CHIP SCALE CARBON NANOTUBE SUPERCAPACITORS WITH IONIC LIQUID ELECTROLYTES

A Dissertation
Presented to
The Academic Faculty

by

Tyler Colling

In Partial Fulfillment
of the Requirements for the Degree
Master of Science in the
School of Materials Science and Engineering

Georgia Institute of Technology
August 2017

CHIP SCALE CARBON NANOTUBE SUPERCAPACITORS WITH IONIC LIQUID ELECTROLYTES

Approved by:

Dr. W. Jud Ready, Advisor
School of Materials Science and Engineering
Georgia Institute of Technology

Dr. Valerie Scott
Microdevices Laboratory
Jet Propulsion Laboratory
National Aeronautics and Space Administration

Dr. Eric Vogel
School of Materials Science and Engineering
Georgia Institute of Technology

Date Approved: July 21, 2017

ACKNOWLEDGEMENTS

I would like to express my sincerest gratitude towards my thesis advisor Dr. W. Jud Ready for his encouragement and guidance throughout this work. I would also like to thank Dr. Valerie Scott for her guidance and assistance in the lab. Additionally, I would like to thank Dr. Eric Vogel for his time and commitment to the present work.

Furthermore, I would like to acknowledge the NASA project NNN12AA01C FY16 JPL SURP as well as the Georgia Tech Vertically Integrated Projects program for funding this work.

A great appreciation is extended to Stephan Turano for his ever present guidance, knowledge, insight, lab management, and general assistance. In particular, a special thank you for your time in training and helping me with all the necessary equipment to complete this project. Additionally, your assistance and expertise using a scanning electron microscope to characterize samples is greatly appreciated.

I also wish to thank Dr. Philip Campbell for his help conducting X-ray photoelectron spectroscopy experiments and his fruitful discussions on experimental design. Additionally, I thank Andrew Marshall for his assistance in conducting impedance spectroscopy experiments.

Finally, I would also like to recognize my family for their never ending support, encouragement, and patience throughout my life. Furthermore, I would like to extend my sincerest gratitude to Ms. Gloria Bowen for being continually by my side providing encouragement, support, and jokes that made every day more enjoyable.

TABLE OF CONTENTS

ACKNOWLEDGEMENTS iii

LIST OF TABLES vi

LIST OF FIGURES vii

LIST OF SYMBOLS AND ABBREVIATIONS xvii

SUMMARY xix

CHAPTER 1 Introduction 1

CHAPTER 2 Background 4
2.1. Overview of Energy Storage Devices 4
2.2. Helmholtz Double Layer 6
2.3. Pseudocapacitance 7
2.4. Electrodes 8
2.4.1. Carbon Electrodes 10
2.4.2. Functionalization 12
2.5. Electrolytes 20
2.5.1. Aqueous and Organic Electrolytes 20
2.5.2. IL Electrolytes 21
2.6. Electrical Testing 23
2.6.1. Cyclic Voltammetry 24
2.6.2. Galvanostatic testing 24
2.6.3. Electrochemical Impedance Spectroscopy 26
2.7. Applications for Supercapacitors 27
2.8. Chapter Summary 28

CHAPTER 3 Design and Procedure 29
3.1. Design Ideology 29
3.2. Sample Details 30
3.3. Current Collector Fabrication 30
3.4. Electrode Fabrication 34
3.5. Chemical Vapor Deposition synthesis of Carbon Nanotube Electrodes 36
3.6. Functionalization of Carbon Nanotube Electrodes 38
3.6.1. Carbon Modified Carbons 38
3.6.2. Atomic Layer Deposition 39
3.7. Supercapacitor Assembly 42
3.8. Analysis of Electrodes and Assembled Devices 43
3.8.1. Scanning Electron Microscopy 43
3.8.2. Electrical Characterization 44
3.9. Chapter Summary 45

CHAPTER 4 Results and Discussion 46
4.1. Analysis of Current Collectors 46
4.1.1. Life Cycle Tests 48
4.2. Scanning Electron Microscopy 49
4.3. X-ray Photoelectron Spectroscopy 52
4.4. Cyclic Voltammetry 59
4.4.1. Achievable Capacitance 59
4.4.2. Effects of Scan Rate 60
4.5. Constant Scan Rate 68
4.5.1. No Functionalities at Constant Scan Rate 68
4.5.2. Titanium Oxide at Constant Scan Rate 71
4.5.3. Titanium Nitride at Constant Scan Rate 74
4.5.4. Zirconium Oxide at Constant Scan Rate 78
4.5.5. Zirconium Nitride at Constant Scan Rate 81
4.6. Resistance measurements 84
4.6.1. Galvanostatic Method 84
4.6.2. Effects of Viscosity 89
4.6.3. Impedance Spectroscopy 93
4.7. Chapter Summary 99

CHAPTER 5 Conclusion 102

CHAPTER 6 Future Work 105

APPENDIX A Further Figures 107
A.1. Scanning Electron Microscopy 107
A.2. Impedance Data and Fitting 111
A.2.1. No Functionalities 111
A.2.2. Titanium Oxide 114
A.2.3. Titanium Nitride 117
A.2.4. Zirconium Oxide 119
A.2.5. Zirconium Nitride 122

REFERENCES 123

LIST OF TABLES

Table	Caption	Page #
Table 1	List of ILs and their abbreviations used in this work.	22
Table 2	List of ILs and their properties relevant to this work.	23
Table 3	Qualities of supercapacitors.	27
Table 4	Process gases used for atomic layer deposition of pseudocapacitive coatings	39

LIST OF FIGURES

Figure	Caption	Page #
Figure 1	Ragone plot showing batteries and capacitors are essentially opposite energy storage devices, batteries have high energy density and capacitors have high power density [1].	4
Figure 2	Helmholtz double layer formed at the negative electrode. Solvated and adsorbed ions at the electrode create pseudocapacitance.	7
Figure 3	Plot of electrode pore size versus normalized capacitance for carbide derived carbon electrodes showing a dramatic increase in capacitance when the pore size is roughly the size of the largest dimension of the ion [17].	9
Figure 4	Base growth CVD method (a) Carbonaceous gas flows over a strongly bound catalyst (b) Carbon diffusion through base and initial crystallization (c) subsequent carbon deposition at the base of the CNT [23]	12
Figure 5	Carbon nanotubes with varying levels of graphenation [25].	14
Figure 6	Four step atomic layer deposition process [39]. From bottom to top: Substrate is exposed to precursor 1 until adsorption is self-limited. Excess gas is purged from the chamber and the second precursor is flowed over the substrate. The precursors react to form the desired layer and excess gas is purged. This cycle is repeated until the desired thickness is achieved.	18
Figure 7	CNTs functionalized with (top to bottom) increasing number of ALD cycles of TiO_2 [31]. As expected, the CNTs become thicker with increasing number of cycles.	19
Figure 8	Ideal galvanostatic charge/discharge curves – (top) measured voltage vesus time plot used to determine dV/dt to calculate capacitance, (bottom) Constant alternating current for galvanostatic charge/discharge tests.	26

Figure 9	Sample voltage drop for highly resistive capacitor. Using Ohm's law, resistance can be calculated by dividing the measured ΔV by the applied constant current I.	25
Figure 10	Diagram of (a) CNTs (b) carbon modified CNTs (c) pseudocapacitive coated CNTs (d) carbon modified and pseudocapacitive coated CNTs.	30
Figure 11	Full fabrication process design beginning with a (1) highly doped silicon wafer. The wafer is then (2) coated with SiO_2 and patterned with standard lithography techniques (3-4). The SiO_2 and silicon are then etched (5-6) and Ti/Al/Fe are deposited (7). CNTs grow in the bottom of the pits (8) and can be functionalized (9) and ultimately, a pair of chips are assembled with a separator membrane between (10).	32
Figure 12	2μm of SiO_2 is used to prevent a short circuit between electrodes.	33
Figure 13	View of cross section of an electrode showing the desired negative sidewall profile and resulting in no CNT growth on the sidewall.	34
Figure 14	(left) Full view of Black Magic PECVD tool. (right) Schematic of PECVD growth chamber.	36
Figure 15	(Top) Pressure, solid black line, and temperature, dotted black line, profiles for CNT growth. (Bottom) Gas flows for two nitrogen flows, black solid and dashed lines, acetylene flow, dash dot red line, and hydrogen flow, dash double dot red line, to achieve high growth CNT electrodes. The red/dotted lines are scaled to the secondary axes on the right.	37
Figure 16	Carbon modified CNTs displaying carbon foliates.	38
Figure 17	TiO_x coated CNTs.	40
Figure 18	TiN_x coated CNTs.	40
Figure 19	ZrO_x coated CNTs.	41
Figure 20	ZrN_x coated CNTs.	41

Figure 21	(left) Single carbon nanotube electrode with fill ports (right) assembled device showing fill ports prior to filling with electrolyte. (Photo courtesy of Gloria Bowen)	43
Figure 22	Microfabricated supercapacitors utilizing battery coin cell holders as connections for electrical tests.	45
Figure 23	(black) Ideal cyclic voltammetry curve and (red) resistive capacitor where the area is proportional to capacitance.	46
Figure 24	Silicon current collector without CNTs operating with IL A.	47
Figure 25	Capacitance measurements of silicon current collectors without carbon nanotubes.	47
Figure 26	CNTs and IL C 200k life cycle test.	48
Figure 27	CNT heights measured using Quartz PCI software. Uniformity is observed across the entire sample.	50
Figure 28	SEM images taken on a variable pressure SEM. (Left) Fully assembled and filled supercapacitor (cleaved and therefore cavity is not entirely filled). (Right) CNT forest becomes entirely coated with IL when filled.	50
Figure 29	(left) Craters formed from plasma instability striking CNT forest during PECVD growth of carbon foliates. (right) Carbon foliates formed from carbon radicals after damaging the CNTs with plasma.	5151
Figure 30	Limited carbon foliate formation on the tips of CNTs in areas that were not struck by high energy plasma instabilities.	52
Figure 31	All data shifted to strongest carbon peak. Peaks from 285-290 eV are expected to be carbonates and other loosely bonded carbons from leftover resist or ALD process gases.	53
Figure 32	Oxygen spectra showing strong oxygen peaks for oxide samples and the presence of oxygen in nitride samples.	54
Figure 33	Strong nitrogen peaks were observed for the nitride samples. A peak was also observed in TiO_x but is expected to be from carbonaceous amino groups.	55

Figure 34	No silicon peaks were observed which suggests the layer thickness is greater than ~10nm.	56
Figure 35	Ti spectra for the Ti based samples. Broad peaks in TiN_x suggest the presence of oxynitrides.	57
Figure 36	Zirconium peaks were observed in both Zr based samples. However, ZrN_x is much broader which suggests the presence of oxynitrides.	58
Figure 37	Capacitance versus scan rate without pseudocapacitive coating. Capacitances did not exceed 10mF. A typical degradation of capacitance over scan rate is observed.	61
Figure 38	IL B showed the highest capacitance for TiO_x electrodes. IL A under performed and showed no significant reactions with the TiO_x electrodes. Similar degredation of capacitance is shown compared to non-functionalized electrodes.	63
Figure 39	TiN_x capacitance versus scan rate. IL D showed a capacitance over 20mF and the highest stability to 200mV/s. IL E produced the most stable curve over the entire scan rate range, but generally achieved lower capacitance.	63
Figure 40	ZrO_x capacitance versus scan rate. IL D demonstrated the highest capacitance at nearly 14mF but was not stable over the scan rate range. IL B exhibited relatively high capacitance at low scan rates and stability over the entire range.	64
Figure 41	ZrN_x capacitance versus scan rate. IL C produced the highest capacitance over the entire scan rate range. However, the other IL produced much lower capacitances but were much more stable. IL B underperformed and had relatively low capacitance and stability.	64
Figure 42	Electrodes without functionalities – Energy density versus scan rate.	65
Figure 43	TiO_x energy density versus scan rate. IL E exhibits highest energy density, even though it had the lowest capacitance due to its large electrochemical window. However, IL is more favorable at higher scan rates, possibly due to its lower viscosity compared to IL E.	65

Figure 44	TiN_x energy density versus scan rate. IL D showed similar performance had the highest capacitance due to its large electrochemical window and high capacitance. IL D is less favorable at high scan rates where IL E then dominates.	66
Figure 45	ZrO_x energy density versus scan rate. IL D demonstrated the highest energy density as expected since it had the highest capacitance and a 5.5V operating voltage window.	67
Figure 46	ZrN_x energy density versus scan rate. IL C produced the highest energy density as expected because it had the highest capacitance and a voltage window of 5.5 V – the second highest in this study.	67
Figure 47	(left) CV and (right) capacitance versus cycle number plots for non-functionalized electrodes and IL A.	69
Figure 48	(left) CV and (right) capacitance versus cycle number plots for non-functionalized electrodes and IL B.	69
Figure 49	(left) CV and (right) capacitance versus cycle number plots for non-functionalized electrodes and IL C.	70
Figure 50	(left) CV and (right) capacitance versus cycle number plots for non-functionalized electrodes and IL D.	70
Figure 51	(left) CV and (right) capacitance versus cycle number plots for non-functionalized electrodes and IL E.	71
Figure 52	(left) CV and (right) capacitance versus cycle number plots for TiO_x functionalized electrodes and IL A.	72
Figure 53	(left) CV and (right) capacitance versus cycle number plots for TiO_x functionalized electrodes and IL B.	72
Figure 54	(left) CV and (right) capacitance versus cycle number plots for TiO_x functionalized electrodes and IL C.	73
Figure 55	(left) CV and (right) capacitance versus cycle number plots for TiO_x functionalized electrodes and IL D.	73
Figure 56	(left) CV and (right) capacitance versus cycle number plots for TiO_x functionalized electrodes and IL E.	74
Figure 57	(left) CV and (right) capacitance versus cycle number plots for TiN_x functionalized electrodes and IL A.	75

Figure 58	(left) CV and (right) capacitance versus cycle number plots for TiN_x functionalized electrodes and IL B.	76
Figure 59	(left) CV and (right) capacitance versus cycle number plots for TiN_x functionalized electrodes and IL C.	76
Figure 60	(left) CV and (right) capacitance versus cycle number plots for TiN_x functionalized electrodes and IL D.	77
Figure 61	(left) CV and (right) capacitance versus cycle number plots for TiN_x functionalized electrodes and IL D.	77
Figure 62	(left) CV and (right) capacitance versus cycle number plots for TiN_x functionalized electrodes and IL E.	78
Figure 63	(left) CV and (right) capacitance versus cycle number plots for ZrO_x functionalized electrodes and IL A.	79
Figure 64	(left) CV and (right) capacitance versus cycle number plots for ZrO_x functionalized electrodes and IL B.	79
Figure 65	(left) CV and (right) capacitance versus cycle number plots for ZrO_x functionalized electrodes and IL C.	80
Figure 66	(left) CV and (right) capacitance versus cycle number plots for ZrO_x functionalized electrodes and IL D.	8080
Figure 67	(left) CV and (right) capacitance versus cycle number plots for ZrO_x functionalized electrodes and IL E.	81
Figure 68	(left) CV and (right) capacitance versus cycle number plots for ZrN_x functionalized electrodes and IL A.	82
Figure 69	(left) CV and (right) capacitance versus cycle number plots for ZrN_x functionalized electrodes and IL B.	82
Figure 70	(left) CV and (right) capacitance versus cycle number plots for ZrN_x functionalized electrodes and IL C.	83
Figure 71	(left) CV and (right) capacitance versus cycle number plots for ZrN_x functionalized electrodes and IL D.	83
Figure 72	(left) CV and (right) capacitance versus cycle number plots for ZrN_x functionalized electrodes and IL E.	84

Figure 73	(left) Galvanostatic test of non-functionalized CNT capacitor demonstrating an easily discernable voltage drop. (right) Galvanostatic measurement of TiN_x demonstrating significant non-linearity upon discharge and therefore difficulty in establishing a clear voltage drop.	85
Figure 74	Sample data for galvanostatic calculations of total ESR.	86
Figure 75	Resistance measurements compared to IL.	87
Figure 76	Resistance measurements made for samples comprised of TiO_x pseudocapacitive coating and IL A. The large changes in resistance demonstrate a possible heating mechanism from insufficient amounts of electrolyte.	89
Figure 77	Viscosity effects in CNT electrodes. No strong correlation is observed.	91
Figure 78	Viscosity effects in TiO_x coated CNT electrodes. A strong correlation is observed with increasing resistance occurring with higher viscosities.	91
Figure 79	Viscosity effects in TiN_x coated CNT electrodes. No strong correlation is observed.	92
Figure 80	Viscosity effects in ZrO_x coated CNT electrodes. No strong correlation is observed.	92
Figure 81	Viscosity effects in ZrN_x coated CNT electrodes. No strong correlation is observed.	93
Figure 82	Equivalent circuit model for electrochemical reaction. Modified Randles circuit model with extra constant phase element.	94
Figure 83	Resistance of plain CNT samples measured by impedance spectroscopy. Most samples exhibited high resistances for supercapacitor applications, however, these results confirm the calculations from galvanostatic methods. IL B and IL demonstrated the lowest resistances.	95
Figure 84	Resistance of TiO_x samples measured by impedance spectroscopy. Each of the IL A samples exhibited extremely high resistances. It is unclear whether this is due to chemical interactions or manufacturing error due to the high viscosity of the IL. IL B and IL C produced the lowest resistances.	96

Figure 85	Resistance of TiN_x samples measured by impedance spectroscopy. IL A produced high resistances whereas IL D and E produced the lowest resistances with TiN_x.	97
Figure 86	Resistance of ZrO_x samples measured by impedance spectroscopy. IL A and D had high resistances whereas IL B had low resistance. N/A for IL D2 shows that the value had no effect on the fitting of the impedance data.	98
Figure 87	Resistance of ZrN_x samples measured by impedance spectroscopy. N/A signifies the resistance value had no impact for fitting to the measured data. IL A and IL B had the highest resistances with most other samples having resistances comparable to the best samples of other architectures in this work.	99
Figure 88	Ragone plot showing the presented supercapacitor performance with respect to other energy storage devices. A data point is shown for the maximum energy density of each pseudocapacitive coating.	100
A. 1	TiO_x coated CNTs. Thicker coatings are observed at the top which suggests the coating is not conformal. (Photo courtesy of Stephan Turano)	107
A. 2	TiNx coated CNTs. Only the first few µm were actually coated by the ALD process. Further Process development is required to ensure conformal coating of the CNTs.	108
A. 3	Conformal coating of CNTs with ZrO_x but only for the first few µm as seen by the gradient from the top of the figure to the bottom.	108
A. 4	Conformal coating of CNTs with ZrN_x but only for the first few µm as seen by the light area at the tip of the CNTs.	109
A. 5	Carbon functionalized CNTs. Only the tips of the CNTs were able to grow carbon foliates well unless a large spark hit the CNTs in which case the surrounding CNTs were conformally covered. (photo courtesy of Stephan Turano)	109
A. 6	Carbon functionalized CNT. (photo courtesy of Stephan Turano)	110
A. 7	Silicon grass formed from DRIE. The formation of the peaks in the pit must be avoided to ensure adhesion of the catalyst layer and to allow sufficient gas flow to grow CNTs.	110

A. 8	Impedance spectroscopy measurements and fitting for electrodes without functionalities paired with IL A.	111
A. 9	Impedance spectroscopy measurements and fitting for electrodes without functionalities paired with IL B.	112
A. 10	Impedance spectroscopy measurements and fitting for electrodes without functionalities paired with IL C.	112
A. 11	Impedance spectroscopy measurements and fitting for electrodes without functionalities paired with IL D.	113
A. 12	Impedance spectroscopy measurements and fitting for electrodes without functionalities paired with IL E.	113
A. 13	Impedance spectroscopy measurements and fitting for electrodes with TiO_x functionalities paired with IL A.	114
A. 14	Impedance spectroscopy measurements and fitting for electrodes with TiO_x functionalities paired with IL B.	115
A. 15	Impedance spectroscopy measurements and fitting for electrodes with TiO_x functionalities paired with IL C.	115
A. 16	Impedance spectroscopy measurements and fitting for electrodes with TiO_x functionalities paired with IL D.	116
A. 17	Impedance spectroscopy measurements and fitting for electrodes with TiO_x functionalities paired with IL E.	116
A. 18	Impedance spectroscopy measurements and fitting for electrodes with TiN_x functionalities paired with IL A.	117
A. 19	Impedance spectroscopy measurements and fitting for electrodes with TiN_x functionalities paired with IL B.	117
A. 20	Impedance spectroscopy measurements and fitting for electrodes with TiN_x functionalities paired with IL C.	118
A. 21	Impedance spectroscopy measurements and fitting for electrodes with TiN_x functionalities paired with IL D.	118
A. 22	Impedance spectroscopy measurements and fitting for electrodes with TiN_x functionalities paired with IL E.	119
A. 23	Impedance spectroscopy measurements and fitting for electrodes with ZrO_x functionalities paired with IL A.	119

A. 24	Impedance spectroscopy measurements and fitting for electrodes with ZrO_x functionalities paired with IL B.	120
A. 25	Impedance spectroscopy measurements and fitting for electrodes with ZrO_x functionalities paired with IL C.	120
A. 26	Impedance spectroscopy measurements and fitting for electrodes with ZrO_x functionalities paired with IL D.	121
A. 27	Impedance spectroscopy measurements and fitting for electrodes with ZrO_x functionalities paired with IL E.	121
A. 28	Impedance spectroscopy measurements and fitting for electrodes with ZrN_x functionalities paired with IL A.	122
A. 29	Impedance spectroscopy measurements and fitting for electrodes with ZrN_x functionalities paired with IL B.	122
A. 30	Impedance spectroscopy measurements and fitting for electrodes with ZrN_x functionalities paired with IL C.	123
A. 31	Impedance spectroscopy measurements and fitting for electrodes with ZrN_x functionalities paired with IL D.	123
A. 32	Impedance spectroscopy measurements and fitting for electrodes with ZrN_x functionalities paired with IL E.	124

LIST OF SYMBOLS AND ABBREVIATIONS

Abbreviation	Name
Al	Aluminum
ALD	Atomic Layer Deposition
BET	Brunauer-Emmett-Teller
CD	Galvanostatic Charge/Discharge
CNT	Carbon Nanotube
CPE	Constant Phase Element
CV	Cyclic Voltammetry
CVD	Chemical Vapor Deposition
EDLC/ECDL	Electrochemical Double Layer Capacitor
EIS	Electrochemical Impedance spectroscopy
ESR	Equivalent Series Resistance
Fe	Iron
g-CNT	Graphenated Carbon Nanotube
IL	IL
IL A	1-Butyl-3-methylimidazolium tetrafluoroborate
IL B	1-Ethyl-3-methylimidazolium bis(trifluoromethylsulfonyl)imide
IL C	1-Butyl-1-methylpyrrolidinium bis(trifluoromethylsulfonyl)imide
IL D	Triethylsulfonium bis(trifluoromethylsulfonyl)imide
IL E	Diethylmethyl(2-methoxyethyl)ammonium bis(trifluoromethylsulfonyl)imide
IoT	Internet of Things
IUPAC	International Union of Pure and Applied Chemistry

mF	millifarad
MWCNT	Multi-Walled Carbon Nanotube
nm	nanometer
PECVD	Plasma Enhanced Chemical Vapor Deposition
Redox	Reduction and Oxidation
RTIL	Room-Temperature IL
SEM	Scanning Electron Microscopy
SWCNT	Single-Walled Carbon Nanotube
TEM	Transmission Electron Microscopty
Ti	Titanium
XPS	X-Ray Photoelectron Spectroscopy
Ω	Ohm
µm	Micrometer

SUMMARY

Supercapacitors are a unique technology with capabilities to fill the gap in energy storage devices to provide both high energy and power density. This work focuses on developing novel high performance supercapacitors by utilizing silicon processing and growing embedded functionalized carbon nanotube electrodes.

A wide array of carbon materials have been studied as electrodes for supercapacitors. This work focuses on vertically aligned carbon nanotubes with titanium and zirconium oxide and nitride functionalities in order to improve the energy density.

Various ILs were surveyed as electrolytes. ILs are more favorable than traditional aqueous or organic electrolytes for their low volatility, low vapor pressure, and high electrochemical window. In this work, five ILs were selected based on a few parameters – high electrochemical windows, varied viscosities, and high temperature stability.

Cyclic voltammetry, galvanostatic methods, and impedance spectroscopy were employed to evaluate capacitance and resistance of the developed supercapacitor architectures. These tests demonstrated high energy storage in most titanium nitride coated CNT electrodes. Some zirconium nitride samples exhibited similar capacitance as titanium nitride. Titanium oxide samples demonstrated high capacitance as well, but lower than the nitride counter parts. Zirconium oxide performed poorly and maintained similar capacitance to non-functionalized CNT electrodes. The ALD coatings added some resistance to the samples, however the results are not easily quantifiable due to manufacturing error resulting from the high viscosity of the ILs.

On the basis of this research, it is suggested to pursue nitride coatings in further research. The traditional oxide coatings performed well but generally had lower capacitance and higher resistance. The highest capacitance values were obtained with the nitride coatings paired with IL C and D. Lower viscosity ILs generally performed better which supports the need for further development to ensure full electrolyte filling.

CHAPTER 1

INTRODUCTION

The energy storage industry consists predominately of batteries and capacitors. Batteries have high energy storage capabilities but may consist of harmful chemicals, lack high/pulse power capabilities, and tend to possess short cycle lifetimes. Traditional capacitors benefit from high power density and a long cycle lifetime but lack significant energy storage during use. These devices leave a gap in the energy storage spectrum for devices with high power and high energy. Supercapacitor research attempts to bridge the gap and produce a device that maintains the benefits of both batteries and capacitors. Specifically, this work is inspired by the versatility and unique properties of carbon nanostructures for supercapacitor electrodes. Particularly, carbon nanotubes (CNTs) have potential to be extremely useful electrode materials due to their inert nature, porous structure, and high conductivity.

Supercapacitor performance is fundamentally controlled through electrode and electrolyte properties and interactions, especially the surface area of the electrode and the dielectric constant of the electrolyte. However, careful consideration of other parameters such as porosity, pore size, ion size, viscosity, operational temperature range, and electrochemical window can be used to optimize the performance. Additionally, expected operating conditions such as current, voltage, and temperature can drastically change the performance.

Carbon based supercapacitors have long been in development, however, few chip scale, silicon based, vertically aligned carbon nanotube based supercapacitors have been developed. This work focuses on the development of a novel hybrid supercapacitor architecture utilizing functionalized vertically aligned carbon nanotube (CNT) electrodes among a survey of ionic liquid (IL) based electrolytes.

CNTs have been widely studied for a variety of applications, however, their use in supercapacitors is particularly unique. By growing forests of vertically aligned CNTs embedded in silicon, a highly porous and robust electrode can be realized that is easily scalable within the silicon industry. The high porosity of CNTs is essential for two reasons – (1) High porosity correlates with high surface area and high capacitance, and (2) high porosity provides many surfaces that can be further functionalized to increase capacitance through pseudocapacitance.

Pseudocapacitance can be induced through interactions between electrode and electrolyte. However, reactive materials need to be deposited on the relatively unreactive CNTs. Atomic layer deposition (ALD) is particularly useful for this application as it is a self-limited, conformal, and highly controllable deposition technique. A variety of materials can be deposited through ALD, but particular attention is paid to titanium and zirconium oxides and nitrides in this work.

The electrolyte has a significant impact on the performance of a supercapacitor, particularly as it pertains to pseudocapacitance. The chemistry between the electrode materials and the electrolyte need to be such that charge transfer can occur either through electron or ion transfer to the surface or ionic intercalation into the electrode. These

reactions must remain highly reversible over many cycles since applications for supercapacitors demand long cycle lives. Other properties of the electrolyte are important as well such as the electrochemical window, which will affect both energy and power density, the dielectric constant, and the viscosity.

Evaluating a variety of pseudocapacitive coatings and electrolytes is imperative to improving supercapacitor performance. This work focuses on evaluating four coatings and five IL (IL) electrolytes and characterizing the resulting capacitance, resistance, energy density, and power density.

CHAPTER 2

BACKGROUND

2.1. Overview of Energy Storage Devices

The two most widely known devices for energy storage are batteries and capacitors. Batteries have high energy density but low power density, and capacitors have low energy density but high power density. Batteries have relatively short cycle lifetimes, on the order of thousands, whereas capacitors have cycle lifetimes on the order of hundreds of thousands [1]. However, these devices fail to account for the whole energy storage spectrum. There is a fundamental gap between capacitors and batteries, as shown in Figure 1, which is filled by electrochemical double layer capacitors (EDLC), (ECDL), also known as 'supercapacitors' or 'ultracapacitors' [1-3].

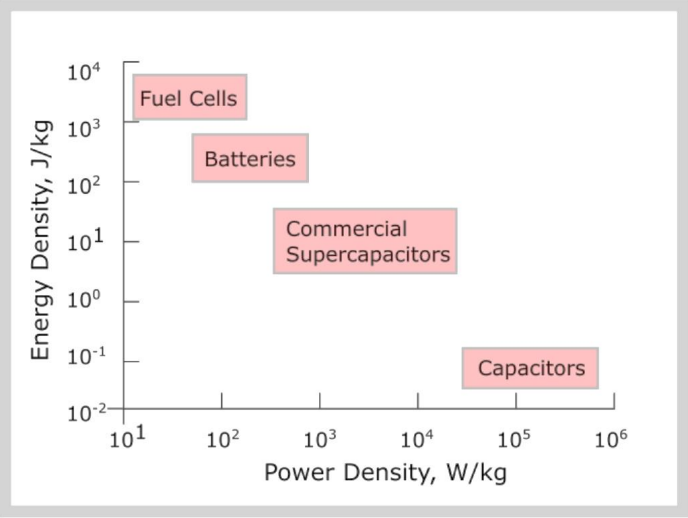

Figure 1: Ragone plot showing batteries and capacitors are essentially opposite energy storage devices, batteries have high energy density and capacitors have high power density [1].

Supercapacitors are characterized through their energy density, power density, volume, and mass. Energy density, E, and power density, P, are defined by Equations 1 and 2, where C is the capacitance, ΔV is the operational voltage window, and ESR is the equivalent series resistance. Both of these equations are frequently normalized by the active electrode volume or mass.

$$E = \frac{1}{2} C \Delta V^2 \tag{1}$$

$$P = \frac{1}{2} \frac{\Delta V^2}{ESR} \tag{2}$$

Supercapacitors have moderately high energy and power density each of which can span a few orders of magnitude depending on the architecture. Furthermore, supercapacitors maintain some of the best attributes of both batteries and capacitors, such as the extremely high cycle life and sustainable architecture. The wide range of energy and power densities, along with long cycle life makes supercapacitors a highly competitive energy storage device.

Two broad categories of supercapacitors are prevalent today, the Helmholtz double layer capacitor, and the pseudocapacitor. Helmholtz double layer capacitors operate on the Helmholtz double layer phenomena, whereas pseudocapacitors operate through reduction-oxidation (redox) reactions.

2.2. Helmholtz Double Layer

The double layer capacitance was first described by Hermann von Helmholtz, a German physicist, in 1853 [4]. This phenomena is non-faradaic, and is analogous to a traditional capacitor in which an applied voltage causes charge separation at the electrode interfaces and is governed by Equation 3. Where C is the capacitance, ε_0 is the permittivity of free space, ε is the dielectric constant of the dielectric material, A is the electrode area and d is the distance between electrodes.

$$C = \frac{\varepsilon_0 \varepsilon A}{d} \tag{3}$$

In electrochemical capacitors, the electrolyte forms a double layer at the electrode as shown in Figure 2. The distance in Equation 1 is reduced to <1nm, defined by the size of the solvent molecules, which results in a dramatic increase in capacitance. However, a functional capacitor, by definition, must have two current collecting electrodes [1], therefore two opposing Helmholtz double layers are formed, between each electrode and the electrolyte, in series.

The Helmholtz double layer phenomena is largely an electrostatic, very high power phenomena [5]. However, it still lacks energy storage. In order to achieve high energy densities, other phenomena, such as pseudocapacitance must be deliberately introduced into the system.

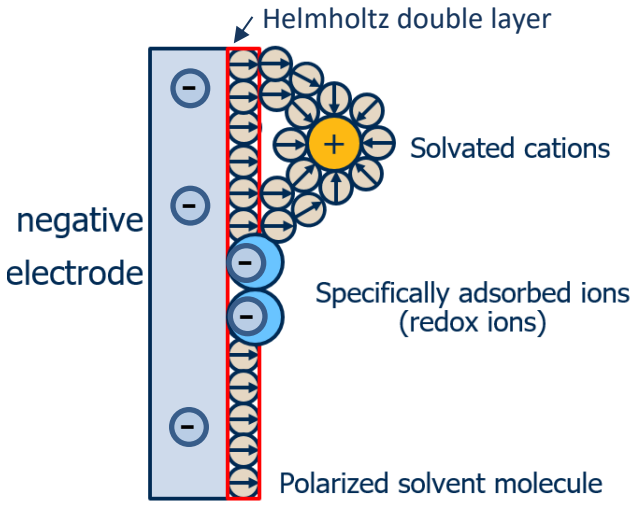

Figure 2: Helmholtz double layer formed at the negative electrode. Solvated and adsorbed ions at the electrode create pseudocapacitance.

2.3. Pseudocapacitance

First developed, in 1991, by Conway et al. [6], pseudocapacitance is a reversible faradaic charge transfer process that occurs through reversible redox reactions at the electrode/electrolyte interface [1, 5, 7, 8]. Pseudocapacitance is analogous to the charge storage in a battery, except in a pseudocapacitor, the ions are loosely intercalated with the electrode surface whereas a battery exhibits deep ionic intercalation [9]. A Helmholtz double layer does not involve any ionic intercalation and is non-faradaic. Intercalated ions are able to be detected by precision mass measurements. This phenomena has first been observed in pseudocapacitance by Snook et al. [8] and can be used to separate the effects of pseudocapacitance from Helmholtz double layer effects.

The redox reactions in pseudocapacitors are highly reversible and therefore will have an extended lifetime compared to batteries. In general, to induce pseudocapacitance, the electrode and electrolyte materials must be deliberately chosen for that purpose. It is possible to observe small amounts of pseudocapacitance in solely carbon electrodes with

proper electrolyte selection however the effects are insignificant [1]. This work will intentionally coat carbon based electrodes to induce significant pseudocapacitive effects.

2.4. Electrodes

Formation of the Helmholtz double layer and pseudocapacitance are both surface effects and are directly related to the electrode material [3]. Therefore, electrode selection is important in optimizing any energy storage device. The electrode must interact appropriately with the electrolyte for maximum power, energy storage, and longevity. In general, an electrode is required to have high specific surface area, controlled porosity, high conductivity, electroactive sites, and low cost [9].

High surface area electrodes are important to achieve high capacitance, as shown in Equation 3, and can be produced using porous electrodes. However, a high degree of porosity is not the only requirement for high surface area. The surface area needs to be accessible by the electrolyte through percolated network of accessible pores. The most well-known technique to determine active surface area is Brunauer-Emmett-Teller (BET) testing. BET is a non-destructive test that measures gas adsorption on the surface of a material, often N_2 at 77 K [10, 11]. Many authors have examined polymeric, carbon, and transition metal oxide electrodes [12] each of which have high accessible surface area on the order of 1720, 2500, and 300 m^2/g, respectively [12-14].

A percolated network of accessible pores is essential for high surface area electrodes, however, the size of the pore will be particularly important for electrode materials [15]. According to IUPAC standards, pore sizes should be classified into three standards as follows – macropores have widths greater than 50 nm, mesopores have widths

between 2 – 50 nm, and micropores have widths less than 50 nm [11]. It has been shown that pore size must correspond with ion size in the electrolyte [15-17]. Largeot et al. demonstrated that there is an optimal pore size based on the size of the anions and cations in the electrolyte [17]. They found that a pore size that is slightly smaller than the largest dimension of the ions maximizes the achievable capacitance. This minimizes any free space on the electrode while still allowing ions to diffuse into the pore. However, it is suggested that if the pore size is significantly smaller than the largest dimension of the ion the ions are no longer able to utilize the exposed surface area, and the accessible surface area is reduced. Generally, it was considered that the number of micropores in a supercapacitor electrode should be minimized [18], however recent work has shown that utilizing micropores can realize significant improvements in capacitance when an appropriately sized electrolyte is used, as shown in Figure 3 [16, 17].

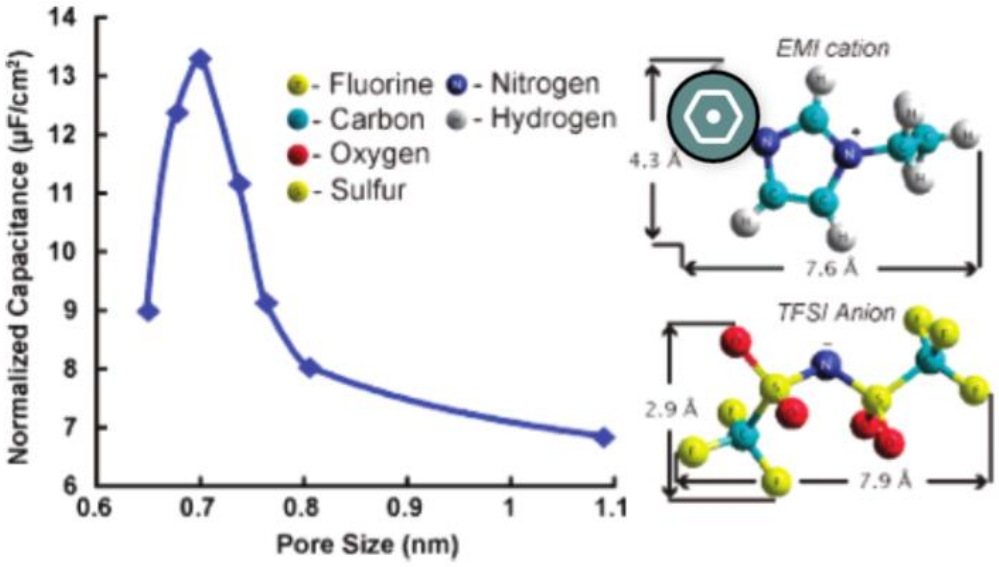

Figure 3: Plot of electrode pore size versus normalized capacitance for carbide derived carbon electrodes showing a dramatic increase in capacitance when the pore size is roughly the size of the largest dimension of the ion [17].

2.4.1. Carbon Electrodes

Carbon materials tend to make excellent electrodes due to their low cost, high conductivity, high surface area, high temperature stability, and high corrosion resistance [2, 12, 19]. The low cost of carbon structures is largely due to the availability of carbon and the pre-existing carbon processing techniques [12]. These techniques have resulted in a variety of useful carbon structures for potential use as electrodes such as CNTs, graphene, aerogels, onions, and carbon black. Carbon materials are also considered environmentally friendly, which makes them an ideal candidate for use in the energy storage industry that has been plagued by harmful chemicals [19].

Carbon materials can be manufactured with controlled porosity to tune an electrode to the electrolyte. In any energy storage device, the pore length and diameter will determine the accessible surface area as well as determine the ESR [1, 3, 17]. Therefore, by controlling the pore size, it is possible to control the energy and power density through the capacitance and ESR.

Due to their unreactive nature, carbon based supercapacitors are limited to charge storage through the Helmholtz double layer. Although the Helmholtz double layer increases the capacitance dramatically, the energy density produced is still limited in its use and needs to be increased [20]. Clever electrode functionalization techniques must be used, such as graphenation and ALD discussed in section 2.4.3, to create a carbon based supercapacitor for widespread use. Carbon aerogels, carbon black, graphene, and CNTs are common carbon based electrode architectures. This work focuses on CNTs and graphene.

2.4.1.1 Graphene

Graphene based electrodes are suggested to have ultra-high accessible surface area because, as a two dimensional sheet, both sides are accessible by the electrolyte. However, graphene sheets will require extensive processing development as the sheets are likely to form graphite [21]. Carbon nanotubes do not possess this characteristic, and therefore may be more suitable for carbon based electrodes.

2.4.1.2 Carbon Nanotubes

CNTs are composed of one or more graphene sheets rolled into a cylindrical shape, forming single walled carbon nanotubes (SWCNT) or multi-walled carbon nanotubes (MWCNT), respectively. Similar to graphene, CNTs are composed entirely of surface atoms. However, only the outside of the CNTs are actually used in surface reactions. The diameter of the CNTs is therefore extremely important in determining surface area and will be drastically different for SWNTs and MWNTs.

CNTs are generally grown by three methods including high pressure arcs, laser ablation and chemical vapor deposition (CVD) [22]. CVD is the most widely used technique for CNT growth due to its simplicity, low cost, structure control, scalability, and versatility. In the simplest form, CNT growth by CVD involves flowing a carbonaceous gas, such as acetylene, methane, or carbon monoxide, over catalyst, such as Fe, Ni, or Co, at elevated temperatures ranging from 600 – 900 °C. A variety of carbon structures and formations can be synthesized by varying the gas flow, temperature, catalyst, or substrate [23]. Two widely accepted growth mechanisms for CNTs are tip-growth, and base growth. This work will focus on the latter as shown in Figure 4.

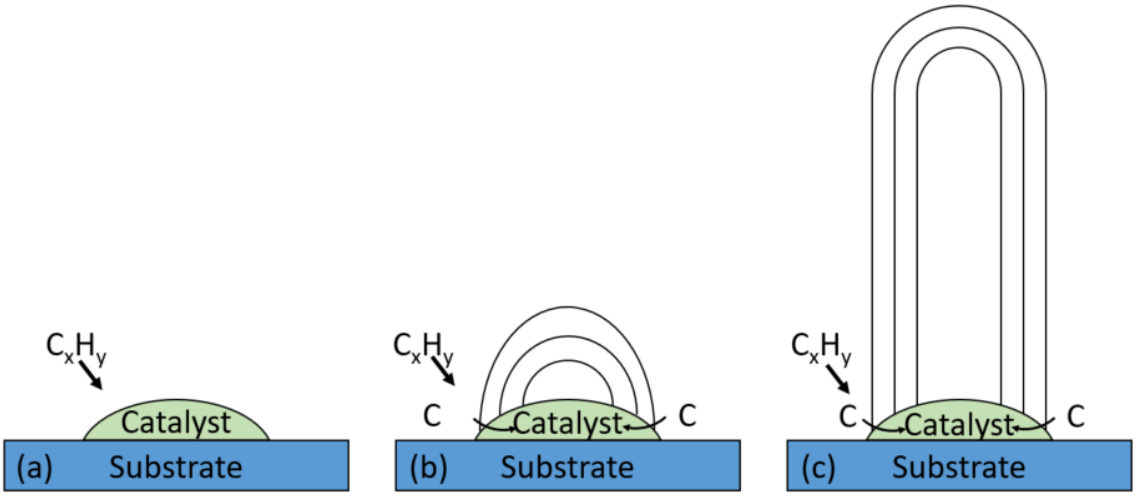

Figure 4: Base growth CVD method (a) Carbonaceous gas flows over a strongly bound catalyst (b) Carbon diffusion through base and initial crystallization (c) subsequent carbon deposition at the base of the CNT [23]

CVD is a well-known, scalable technology that can be easily incorporated into current silicon technology. Growing CNTs on a silicon wafer by CVD could be a promising method to mass produce CNTs. For this reason, this work focuses on the use of highly doped silicon wafers and CVD grown CNT supercapacitor electrodes.

However, CNT electrodes have been plagued by their microtexture, defects, low micropore volume, and catalyst contamination which results in relatively low specific capacitance values [24]. To increase the specific capacitance, various forms of functionalization can be used.

2.4.2. Functionalization

Surface functionalities can have tremendous impact on the achievable capacitance by affecting the wettability of the electrode surface, increasing surface area, and inducing pseudocapacitance [2]. Carbon based supercapacitors, without any functionalization,

operate on the basis of the Helmholtz double layer which produces high power density, but relatively low energy density. Two different types of functionalization are discussed in this work. Graphenation, growing graphene on the electrodes, and pseudocapacitance induced by transition metal oxides.

2.4.2.1 Graphenation

Graphene has a fundamental advantage of other carbon source electrodes since it is two dimensional. However, for the same reason, graphene electrodes are difficult to synthesize without creating graphite. To overcome this inherent difficulty, graphene has previously been grown on CNTs [25, 26]. Growing graphene on CNTs increases the active surface area, of the electrode and allows for further porosity control and thus will produce a higher energy density supercapacitor.

Graphenated CNTs (g-CNTs) are produced through plasma enhanced chemical vapor deposition (PECVD). In this process, multi-walled carbon nanotubes (MWCNT) are used as a substrate and no catalyst is needed for graphene growth. The basic process involves flowing a carbonaceous gas over a damaged MWCNT substrate at high temperatures, ~700°C. The damaged sites act as nucleation sites to grow graphene sheets. However, the details of the graphenation process are not well understood. Parker et al. proposed a nucleation and growth mechanism that involves growing CNTs simultaneously as growing the graphene foliates [25]. They propose that the outer walls of the MWCNTs grow faster than the inner walls which causes buckling of the outer walls. Once the stress is high enough, the outer walls break off and form a nucleation site by which the carbon radicals can attach. Alternatively, Yu et al. propose a method in which the MWCNTs are

grown separately from the graphene foliates [26]. In their method, the MWCNTs were grown without purposely induced defects. These MWCNTs were exposed to an Ar plasma which simultaneously breaks the bonds of the precursor gas and also causes surface defects on the outer walls of the MWCNTs. These defects then act as nucleation sites for the graphene foliates. Yu et al. also propose that the foliates are sp^2 bonded which would result in a highly conductive pathway. Although the fundamental mechanism is not well understood, both articles propose that surface defects are needed to grow graphene foliates on the MWCNTs [25, 26]. Results from Parker et al. are shown in Figure 5.

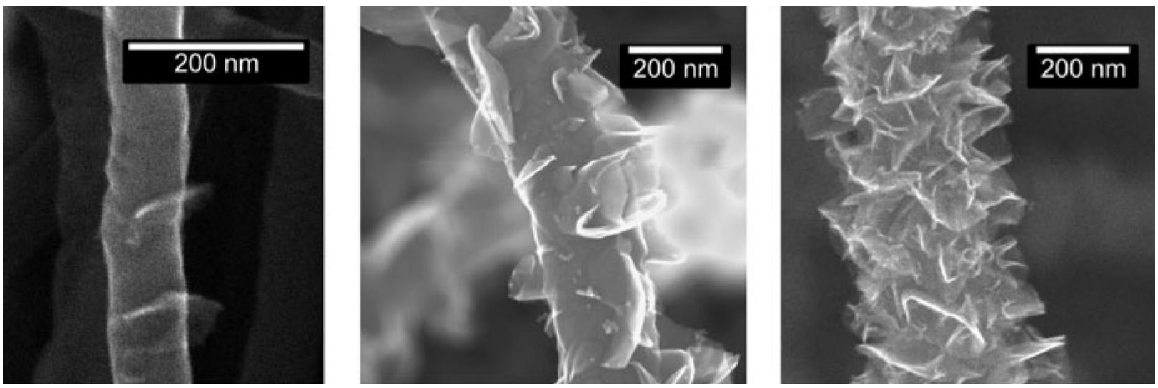

Figure 5: Carbon nanotubes with varying levels of graphenation [25].

2.4.2.2 Transition Metal Oxides

CNT and g-CNT supercapacitor electrodes will operate based on the Helmholtz double layer capacitance. Through further functionalization a faradaic, pseudocapacitive reaction, can be induced. This hybrid device would be able to take advantage of both charge storage mechanisms. In general two materials are used to create pseudocapacitors, conductive polymers and transition metal oxides. Conductive polymers tend to degrade quickly, therefore the alternative is focused on in this work.

Pure metal oxide electrodes, such as RuO_2, MnO_2, NiO, V_2O_5 and SnO_2 exhibit excellent pseudocapacitive properties. However, they lack some of the requirements for electrode materials. The conductivity of these electrodes is very low with the exception of RuO_2. The electrodes tend to crack during electric cycling, and the porosity is difficult to control [9]. Therefore, it is intuitive to attempt to make a hybrid system that involves a carbon based electrode, with controlled porosity and improved conductivity, while also using layers of transition metal oxide particles to induce pseudocapacitance. A brief discussion of pseudocapacitive layers follows, but an extensive overview is reported by Fisher et al. [27].

Ruthenia is regarded as the most promising transition metal oxide based on its high theoretical pseudocapacitance, conductivity, thermal and chemical stabilities, large voltage window, and highly reversible redox reactions [27, 28]. Two forms of RuO_2 are used in electrodes, hydrous and anhydrous, with hydrous exhibiting a higher specific capacitance. This is attributed to mixed proton-electron conductivities of hydrous RuO_2 contributing to faradaic charge transfer process [29]. Although RuO_2 has promising chemical and electrical properties, it has limited industrial applications due to high cost, limited availability, and toxicity [30, 31].

Titania has also been studied for its application in pseudocapacitors. Titania has three different polymorphs – rutile, anatase, and brookite – each with a different crystal structure resulting in different material properties. It has been shown that rutile has higher conductivity and improved pseudocapacitive behavior over anatase and is generally preferred in electronics applications [32]. Titania has shown to be a sufficient alternative pseudocapacitive material to RuO_2. Reddy et al. [24] produced both TiO_2 and RuO_2

nanoparticles on identical electrodes which resulted in similar performances of 160 F/g and 138 F/g respectively. The higher performance of TiO_2 is possibly due to the authors using anhydrous crystalline RuO_2 rather than hydrous RuO_2. Fisher et al. [31] have reported nearly a doubled energy density from TiO_2 coated CNT arrays than their uncoated counterparts. Aside from its comparable performance, TiO_2 is more cost effective and more sustainable than RuO_2 and is therefore of interest as a pseudocapacitve layer [28].

Zirconia is a non-conventional pseudocapacitive material. However, it has many properties that would make it an excellent electrode material such as chemical stability, conductivity, and low cost. Many authors [33-35] have reported significant increases in pseudocapacitance. Zhang et al. created carbon/ZrO_2 aerogel electrodes through a single step sol-gel process. The ZrO_2 nanoparticles were between 2-3nm in size and the electrode retained 77% capacitance after 500 cycles [33]. Mudila et al. used a different approach and created zirconia/graphene oxide nanocomposites which exhibited large redox peaks in the cyclic voltammogram, cycle lifetimes up to 1,000 cycles, and low ESR. Liu et al. [35] deposited ZrO_2 onto graphene nanosheets using atomic layer deposition and reported a 6x increase in capacitance when compared to plain graphene nanosheet supercapacitors under identical conditions.

Although transition metal oxides have traditionally dominated the pseudocapacitive regime, transition metal nitrides are recently of significant interest due to their low cost, corrosion resistance, and high conductivity (relative to transition metal oxides) [36]. Of particular interest are vanadium nitrides because they possess a number of oxidation states and a higher conductivity than its oxide counterpart [30]. TiN is also of significant interest

and have shown a 500% increase in capacitance when deposited on CNT electrodes compared to the bare CNT counterparts [37].

Many methods have been investigated for depositing or growing transition metal oxides on porous electrodes for pseudocapacitors. However, this work will focus on deposition through atomic layer deposition (ALD). ALD is a particularly attractive method for functionalizing CNT arrays due to the inherent porosity control, thickness control, and conformal and homogeneous deposition [38]. ALD is a four step process as shown in Figure 6: (1) exposure of the substrate to the first precursor gas, (2) pump/purge for removal of excess first precursor gas, (3) exposure of the substrate and first precursor gas to the second precursor/reactive gas, (4) pump/purge for removal of second precursor gas. This process has been successful in coating porous and high aspect ratio materials, such as nanotubes and porous carbon structures, with various oxide materials [38, 39]. Fisher et al. were able to successfully coat CNT arrays with TiO_2 as shown in Figure 7.

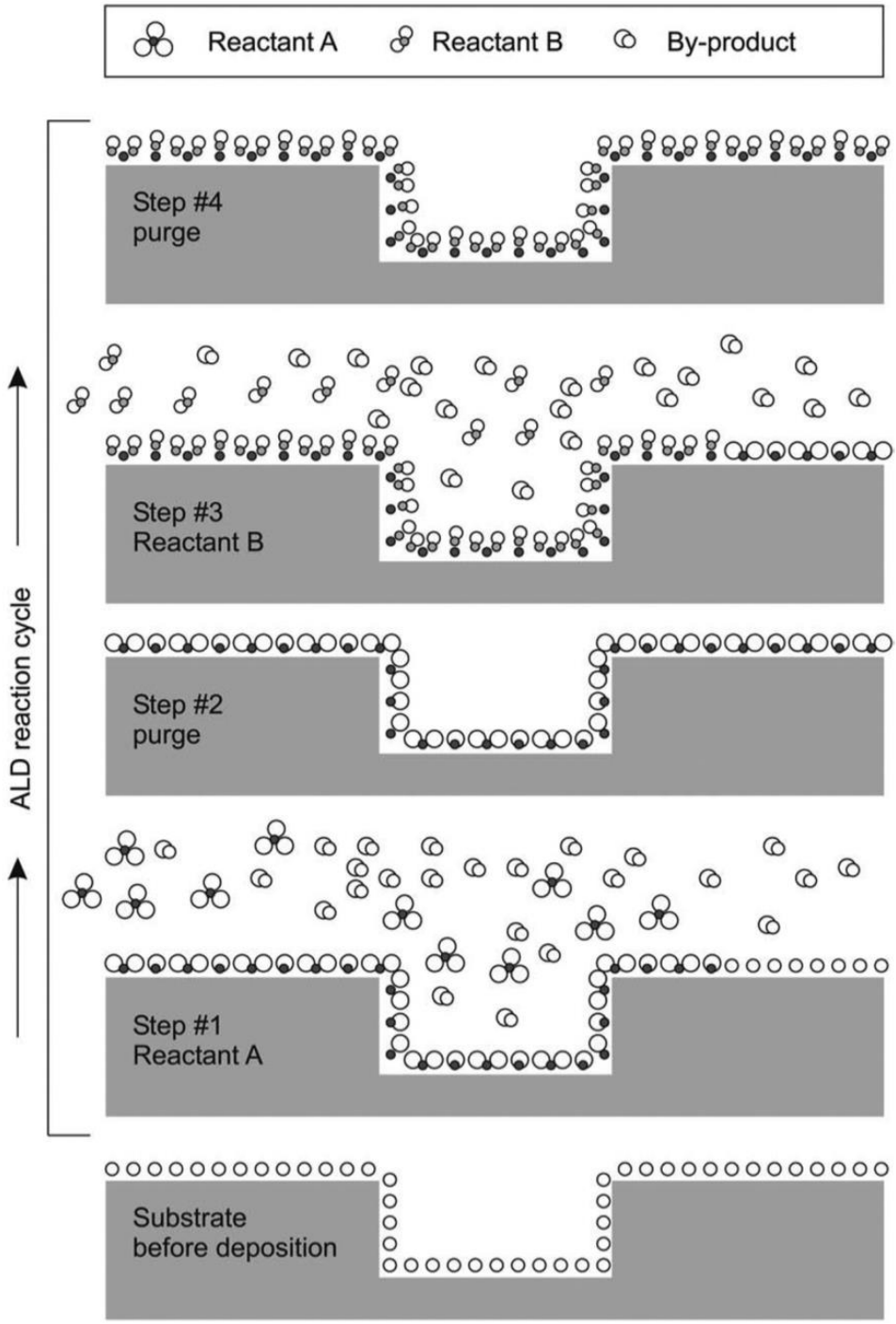

Figure 6: Four step atomic layer deposition process [39]. From bottom to top: Substrate is exposed to precursor 1 until adsorption is self-limited. Excess gas is purged from the chamber and the second precursor is flowed over the substrate. The precursors react to form the desired layer and excess gas is purged. This cycle is repeated until the desired thickness is achieved.

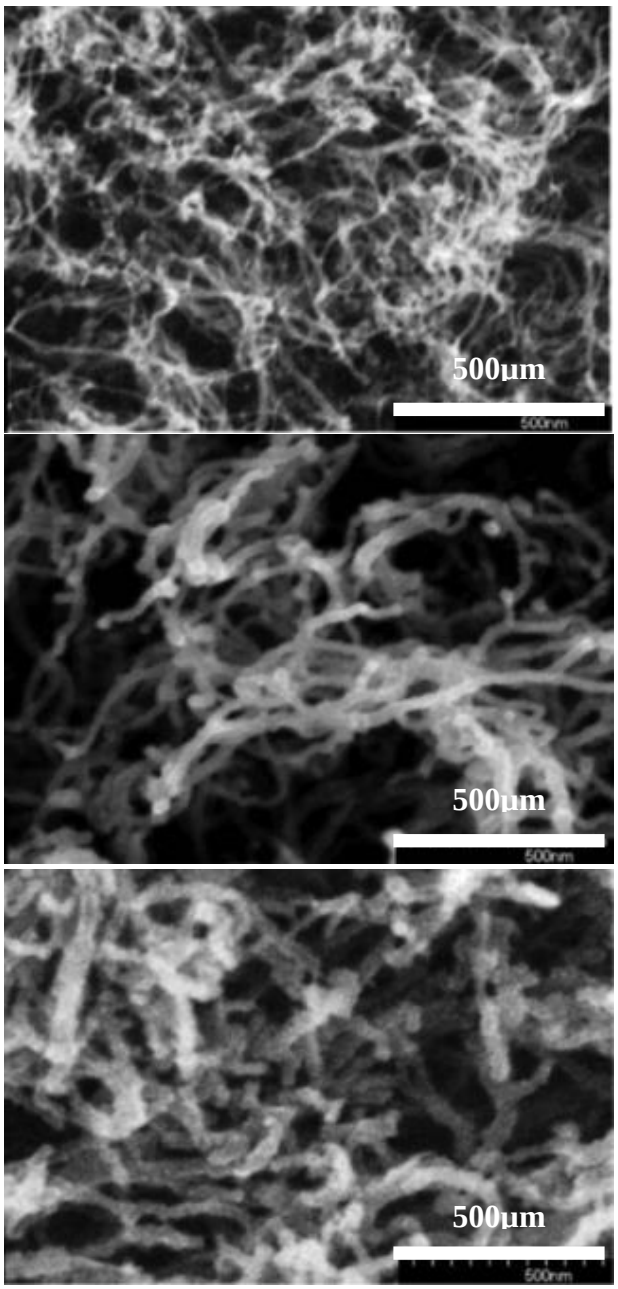

Figure 7: CNTs functionalized with (top to bottom) increasing number of ALD cycles of TiO_2 [31]. As expected, the CNTs become thicker with increasing number of cycles.

2.5. Electrolytes

Equally important as electrode selection, a compatible electrolyte should be chosen in tandem. Electrolyte properties will have a significant impact on the performance of a supercapacitor. Three properties are especially important – (1) Electrolyte resistance will determine the achievable power output [3], (2) ion adsorption on the electrode directly impacts the formation of the double layer, and (3) dielectric properties will determine the double layer capacitance [1].

Maximizing the conductivity and voltage window of an electrolyte is important in order to maximize power capabilities and energy density as seen in Equations 1 and 2. The primary factors affecting conductivity of the electrolyte are the concentration of free charge carriers and their ionic mobility, viscosity and long-range electrostatic anion/cation interactions. The operational voltage window is also particularly important since the energy density is proportional to the square of the operational voltage window [19, 20]. Each of these should be considered when selecting an electrolyte.

2.5.1. Aqueous and Organic Electrolytes

Aqueous and traditional organic electrolytes are composed of a salt and solvent and are the most predominant electrolyte in industrial supercapacitors today. The conductivity of these electrolytes is determined by the solubility of the salt and concentration of free charge carriers. Aqueous electrolytes have an operating voltage range up to ~1.4 V due to the decomposition of water ~1.23 V. Other non-aqueous electrolytes have operating

voltages ranging from 3.0 – 4.0 V but also generally suffer from higher resistivity [5]. The lower voltage range decreases the achievable energy density compared to alternative electrolytes such as room temperature ILs (RTILs). However, aqueous electrolytes are significantly more conductive and therefore have higher power than RTILs.

2.5.2. IL Electrolytes

ILs are composed of large organic cations and anions that are molten salts at low temperatures. Many RTILs degrade when in contact with air and water due to their fluorine based anions and therefore should be stored under dry inert conditions. This also suggests that any system utilizing ILs should be hermetic.

ILs have slightly reduced power compared to other electrolytes, however, their energy density increases tremendously. ILs benefit from a large electrochemical window which corresponds to a large operating voltage. Therefore, ILs are at the forefront of high energy density supercapacitor research. A large electrochemical window has drawn attention to ILs, but they are also unique due to their low vapor pressure, large temperature window, non-volatility, and low environmental impact [40].

High conductivity, and therefore high ionic mobility, is desirable in an electrolyte in order to quickly form a Helmholtz double layer. Viscosity and ion size both contribute to the conductivity of the electrolyte. Sillars et al. showed that increasing viscosity decreased capacitance. Additionally, ion size is particularly important for performance of a supercapacitor as the ion density at the electrode increases with decreasing ion size [41]. Lower ion density would result in less charge storage and lower capacitance. Therefore, a high conductivity, low viscosity, and small ion size is desirable in an electrolyte.

ILs have been known to have relatively similar dielectric constants. Huang et al. studied the relative dielectric permittivity of 42 ILs. Their results show a range of relative permittivity of $10 < \varepsilon_r < 86$. However, the low range, $10 < \varepsilon_r < 16$, was dominated by aprotic ILs with high symmetry, whereas protic ILs were much higher, reaching a maximum of 85.6 [42]. As with most of the physical properties of ILs, the dielectric permittivity can be tuned based on the anion/cation selection. The ILs studied in the present work consist of the symmetric, aprotic, anions, tetrafluoroborate and bis(trifluoromethylsulfonyl)imide, and are therefore expected to have relatively low dielectric constants. However, Sillars et al. suggest that "bulk" dielectric properties in double layer capacitance is not a reasonable assumption. Therefore, as a first calculation approximation, bulk properties may be used, but the results should be accompanied by electrical testing. The ILs studied in this work and their chemical and physical properties are listed in Table 1 and Table 2.

Table 1: List of ILs and their abbreviations used in this work.

IL	Abbreviation
1-Butyl-3-methylimidazolium Tetrafluoroborate	BMIM-BF4
1-Ethyl-3-Methylimidazolium bis(trifluoromethylsulfonyl)imide	EMIM-TFSI
1-Butyl-1-methylpyrrolidinium bis(trifluoromethylsulfonyl)imide	BMP-TFSI
Triethylsulfonium bis(trifluoromethylsulfonyl)imide	TES-TFSI
Diethylmethyl(2-methoxyethyl)ammonium bis(trifluoromethylsulfonyl)imide	DEMMA-TFSI

Table 2: List of ILs and their properties relevant to this work.

	IL	Electrochemical Window (V)	Conductivity (mS/cm)	Viscosity (mPa*s)	Dielectric Constant	Density (g/mL)	Molecular Weight	Anion	Cation
A	BMIM-BF4	4.7[a]	3.2[a] 2.8[b]	141.2[b]	13.9[c]	1.2[d]	226.0	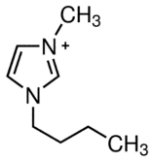	BF_4^-
B	EMIM-TFSI	4.1[d]	8.8[d] 7.8[i]	39.1[b]	12.0[c]	1.5[e]	391.3	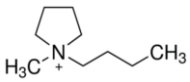	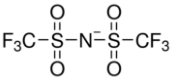
C	BMP-TFSI	5.5[i]	2.2[d] 2.0[i]	76.9[f]	14.7[c]	1.4[f]	422.4	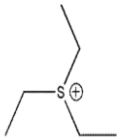	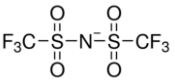
D	TES-TFSI	5.5[i]	5.5[i]	41.1[g]	---	1.5[g]	399.4	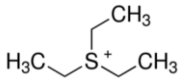	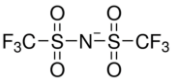
E	DEMMA-TFSI	6.5[i]	2.2[h]	92.7[h]	---	1.4[h]	426.4	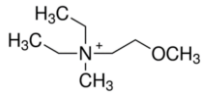	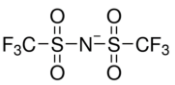

[a] [43] [b] [44] [c] [45] [d] [46] [e] [47] [f] [48] [g] [49] [h] [50]
[i]data obtained from sigma aldrich

2.6. Electrical Testing

Generally, three methods are used to characterize the capacitance of a supercapacitor, cyclic voltammetry (CV), galvanostatic charge/discharge (CD), and electrochemical impedance spectroscopy (EIS) [20].

2.6.1. Cyclic Voltammetry

Capacitance is defined as the ability for a system to store charge. Therefore, determining the capacitance is an essential metric for characterization of supercapacitors and should be maximized in any experiment. CV is one method to determine capacitance. A constant voltage scan rate is applied to a capacitor across a specified voltage range and the current response is measured. From the produced curves, and Equation 4, below, capacitance can be determined.

$$C = \frac{\int_{V_1}^{V_2} i(V)dV}{2(V_2 - V_1)v} \quad (4)$$

C is the capacitance, $i(V)$ is the instantaneous current, V_2 and V_1 are the max and minimum applied voltages, respectively, $\int_{V_1}^{V_2} i(V)dV$, the area of the CV curve, is the total volumetric charge, and v is the voltage scan rate [51]. As shown in Equation 4, capacitance is inversely dependent upon the voltage scan rate. Many researchers have conducted experiments at different scan rates and observed a decrease in capacitance with increasing voltage scan rate, which is expected. However, the scan rate can also be used to 'inflate' results, by scanning at an unrealistically slow rate, and therefore must be reported [21].

2.6.2. Galvanostatic testing

Galvanostatic tests use a constant current to charge and discharge an energy storage device. CD tests are conducted with a constant alternating current as shown in Figure 8 for an ideal curve. This method of analysis allows the use of a common equation for capacitance shown in Equation 5 below,

$$C = i/(\frac{dV}{dt}) \tag{5}$$

where C is the capacitance, i is the constant current, and $\frac{dV}{dt}$ is the slope of the acquired voltage versus time plot [52].

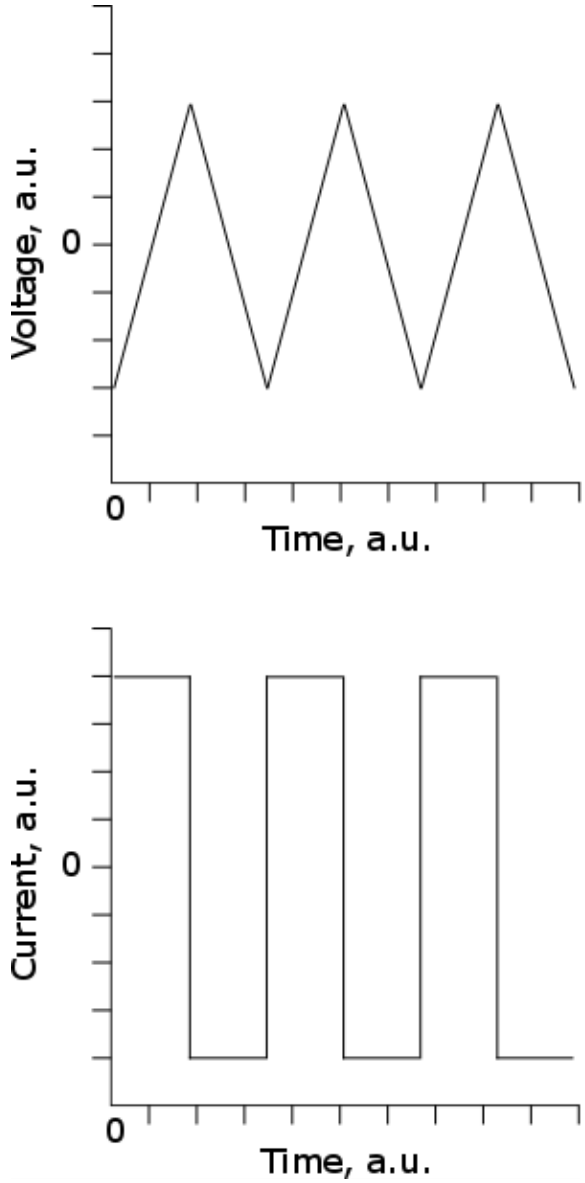

Figure 8: Ideal galvanostatic charge/discharge curves – (top) measured voltage vesus time plot used to determine dV/dt to calculate capacitance, (bottom) Constant alternating current for galvanostatic charge/discharge tests.

The ESR can be obtained easily through CD tests. In the non-ideal case, a voltage drop occurs at the maximum voltage upon discharging as shown in Figure 9. Using ohm's law and the constant applied current, the resistance can be obtained.

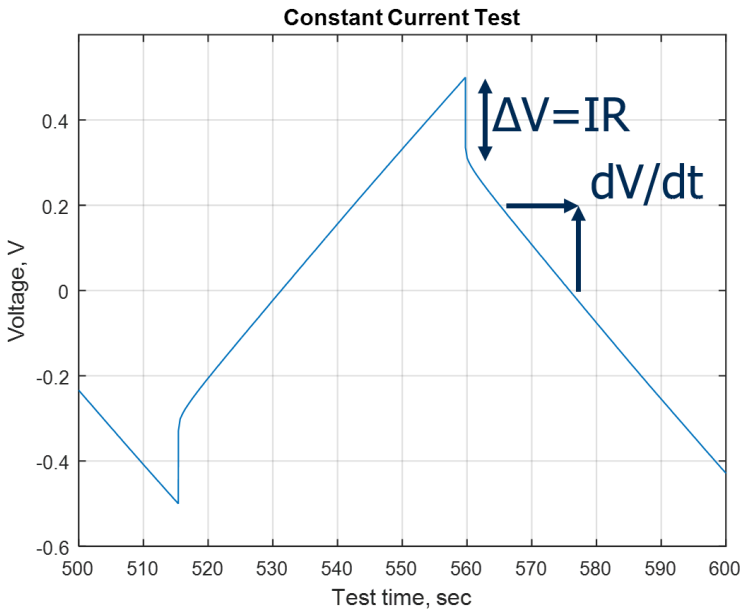

Figure 9: Sample voltage drop for highly resistive capacitor. Using Ohm's law, resistance can be calculated by dividing the measured ΔV by the applied constant current I.

2.6.3. Electrochemical Impedance Spectroscopy

Electrochemical impedance spectroscopy is a thorough electrochemical characterization technique that employs frequency response to analyze a system. Through appropriate selection of an equivalent circuit, to model the electrical response, it is possible to distinguish contributing effects to resistance, capacitance, inductance and porosity [40, 53-56].

2.7. Applications for Supercapacitors

Supercapacitors are ideal candidates for applications where moderate energy densities and high power are required. Such applications include, memory backup, energy harvesting, and pulse power communication devices.

Table 3: Qualities of supercapacitors.

Advantages	Disadvantages
High Power	Low Energy Density (compared to batteries)
Low Resistance	Cost
Long Cycle Lifetime	
Low and High Temperature Operation	

Memory backup is a dramatically growing field with the increase in devices requiring memory storage such as home appliances. Even a brief interruption of power can create memory loss [3]. Therefore a backup power supply must be used in any data storage circuit. A battery would suffice for this application, however, due to the short cycle lifetimes, it would require frequent replacement. Frequent battery replacement is unrealistic since a battery can cost as much as 20% the cost of the final product [57]. The lifetime of the battery can be extended by utilizing a hybrid battery and supercapacitor system.

Energy harvesting devices frequently cycle the energy storage device. The long cycle lifetime of supercapacitors therefore becomes critical in keeping the cost of energy harvesting devices low. Photovoltaic cells currently require battery replacement every three to seven years. Using solely supercapacitors or a hybrid supercapacitor and battery system

would make the lifetime of the energy harvesting and energy storage devices comparable [58].

Currently, batteries are the most popular technology for mobile energy storage devices [59]. However, with the emergence of internet of things (IoT), there are needs for highly cyclable pulse power energy storage devices. Supercapacitors are highly suited for this sort of application. Particularly, supercapacitors are not subject to the levels of wear that a battery is during cycling and therefore would extend the life of the battery by pairing the technologies for IoT applications.

2.8. Chapter Summary

This chapter discussed the fundamental mechanisms of charge storage in supercapacitors as well as various methods to enhance and encourage these mechanisms. Assembly of supercapacitors and supercapacitor electrodes were discussed in detail and the various carbon allotropes that have been investigated with an emphasis on CNT based electrodes. Electrode functionalization mechanisms were addressed, particularly the use of graphenation to increase surface area and porosity control, as well as ALD of pseudocapacitive layers to induce pseudocapacitance. Electrolytes, particularly ILs, were evaluated based on a variety of chemical and physical metrics. The accepted supercapacitor evaluation methods were discussed, as well as applications for supercapacitors.

CHAPTER 3

DESIGN AND PROCEDURE

3.1. Design Ideology

Functionalized carbon nanotube electrodes embedded in highly doped silicon were fabricated using standard silicon processing techniques to create current collectors for CNT electrodes. Silicon processing is well established and scalable and is therefore advantageous for supercapacitor technology. The present research was conducted using 4" silicon wafers, whereas the industry standard is a 12" wafer and therefore, higher throughput would easily be possible in industry. Silicon can withstand the high process temperatures for CNT growth and functionalization and is therefore an ideal substrate. Within the silicon industry, there are also a variety of deposition techniques available that can be used to tailor catalysts, and pseudocapacitive coatings.

This design is chip scale and, in its final form, is intended to be seated directly on a circuit board as a power supply. The small size ensures that the device can be used in a wide range of applications. Since the device can be easily scaled up using silicon processing techniques, it was chosen that a chip scale device would be the most useful to study. Current technologies at Georgia Institute of Technology, within the Institute for Electronics and Nanotechnology cleanroom facilities and Georgia Tech Research Institute, combined with facilities at NASA Jet Propulsion Laboratory within the Microelectronics Laboratory, were used for fabrication and testing of all devices.

3.2. Sample Details

Samples were fabricated from 100µm tall CNT based electrodes (Figure 10 (a)), with carbon and pseudocapacitive functionalizations (Figure 10 (b-d)), and filled with IL electrolytes. A complete list of the ILs used in this work, along with relevant properties can be found in Table 2.

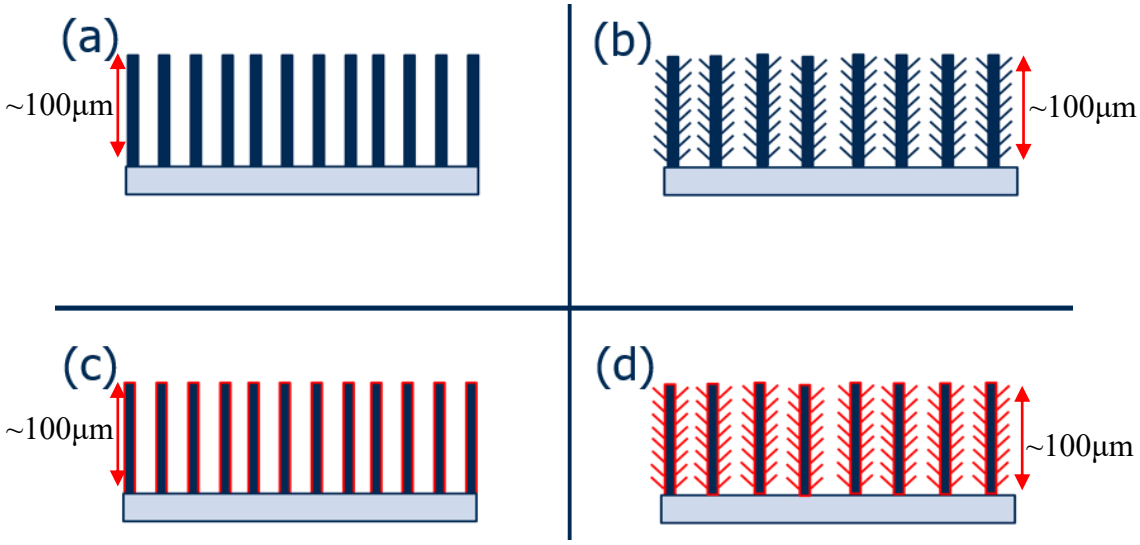

Figure 10: Diagram of (a) CNTs (b) carbon modified CNTs (c) pseudocapacitive coated CNTs (d) carbon modified and pseudocapacitive coated CNTs.

3.3. Current Collector Fabrication

Fabrication of the electrodes takes place over a ten step process, delineated in Figure 11. First, 4", n-type, <111>, single crystal silicon wafers with resistivity of 0.001-0.005 Ω·cm were used as substrates. Two microns of SiO_2 was then deposited over the entire wafer by PECVD using an OXFORD PECVD (*Oxford Instruments, Oxfordshire, UK*) tool Figure 12. The thicknesses were then checked using a Nanospec Reflectometer

(Nan*ometrics Inc., Milpitas, CA USA*). Microposit photoresist primer *(MicroChem Corp., Westborough, MA, USA)* and SPR 220-7 positive photoresist *(MicroChem Corp., Westborough, MA, USA)* were then spincoated onto the wafer at 3000rpm for 60 seconds and at 1500rpm for 45 seconds, respectively. The resulting resist thickness was approximately 10μm thick. The resist was exposed at 550 J/cm^2 in an MA-6 mask aligner *(SUSS Microtech, Garching, Germany)*. The mask produced 7.5mm x 7.5mm squares in the resist. The pattern was then developed in MF-319 *(MicroChem Corp., Westborough, MA, USA)* for 2 minutes and then checked in an Olympus optical microscope *(Olympus Corp., Tokyo, Japan)* for any undeveloped resist. The resist thickness was confirmed using a Dektak profilometer *(Bruker, Billerica, MA, USA)*. The development of the resist exposes the SiO_2 layer within the developed features, which was then etched away using 6:1 buffered oxide etch for 10 minutes (Figure 12), resulting in squares of exposed silicon.

Deep, 250 μm pits are then etched into the exposed silicon on a STS Pegasus ICP (*SPTS Technologies, LTD., Newport, UK)* etch tool using the Bosch process.

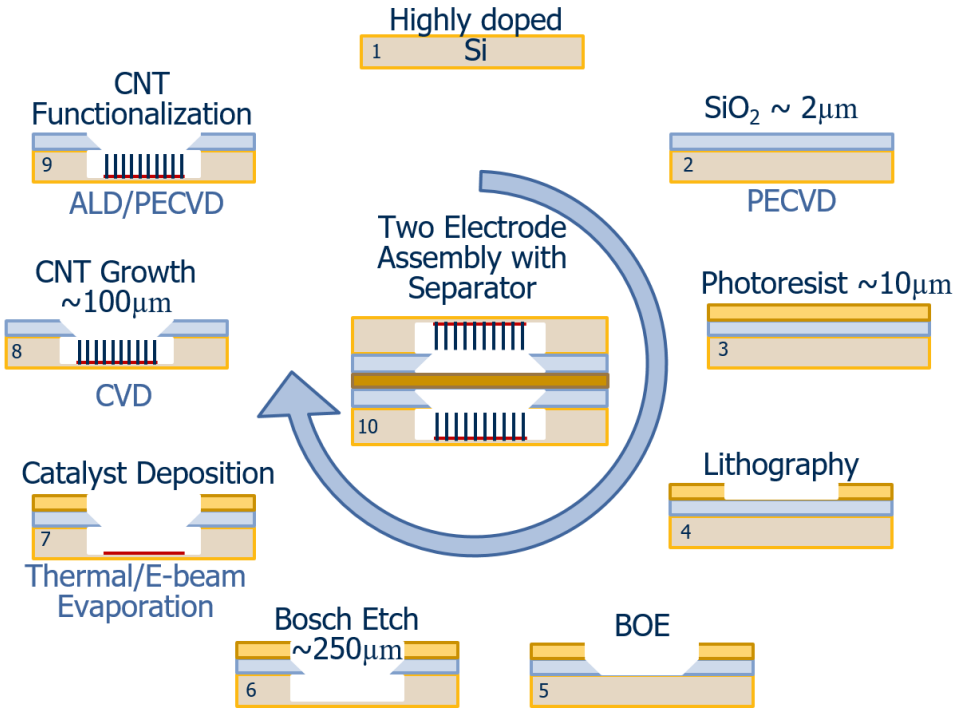

Figure 11: Full fabrication process design beginning with a (1) highly doped silicon wafer. The wafer is then (2) coated with SiO_2 and patterned with standard lithography techniques (3-4). The SiO_2 and silicon are then etched (5-6) and Ti/Al/Fe are deposited (7). CNTs grow in the bottom of the pits (8) and can be functionalized (9) and ultimately, a pair of chips are assembled with a separator membrane between (10).

The Bosch process has a variety of control parameters that allow for profile and texture control inside of the pits. For the studied devices, it is desirable to maintain a negative profile, as shown in Figure 13, while also reducing roughness and silicon grass formation. The negative profile is a hard mask and protects the sidewalls from catalyst during deposition and subsequent nanotube growth which could cause short circuits or shear off CNTs and cause floating charged particles.

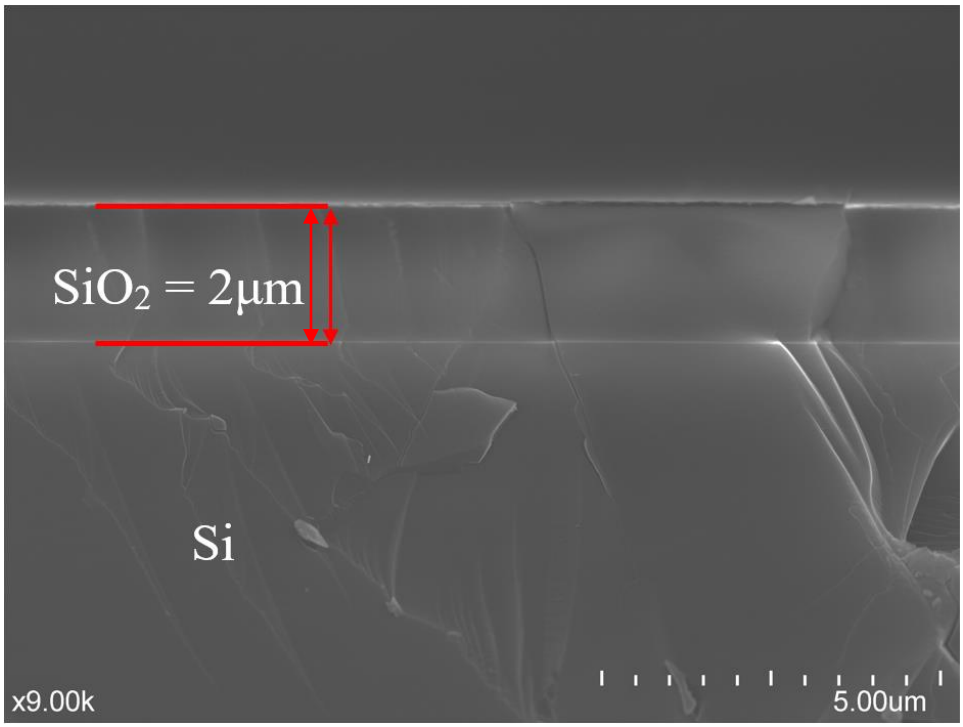

Figure 12: 2µm of SiO_2 is used to prevent a short circuit between electrodes.

Roughness should also be minimized while simultaneously achieving a negative profile. In particular, silicon grass should be eliminated as it was observed to have negative effects on the adhesion of the catalyst layer and also reduced the surface area for CNT growth. Over etching and reducing the passivation time simultaneously improve the negative profile and reduce roughness and silicon grass. Figure 13 shows a cross section of an electrode with a negative sidewall profile and no CNT growth on the sidewall.

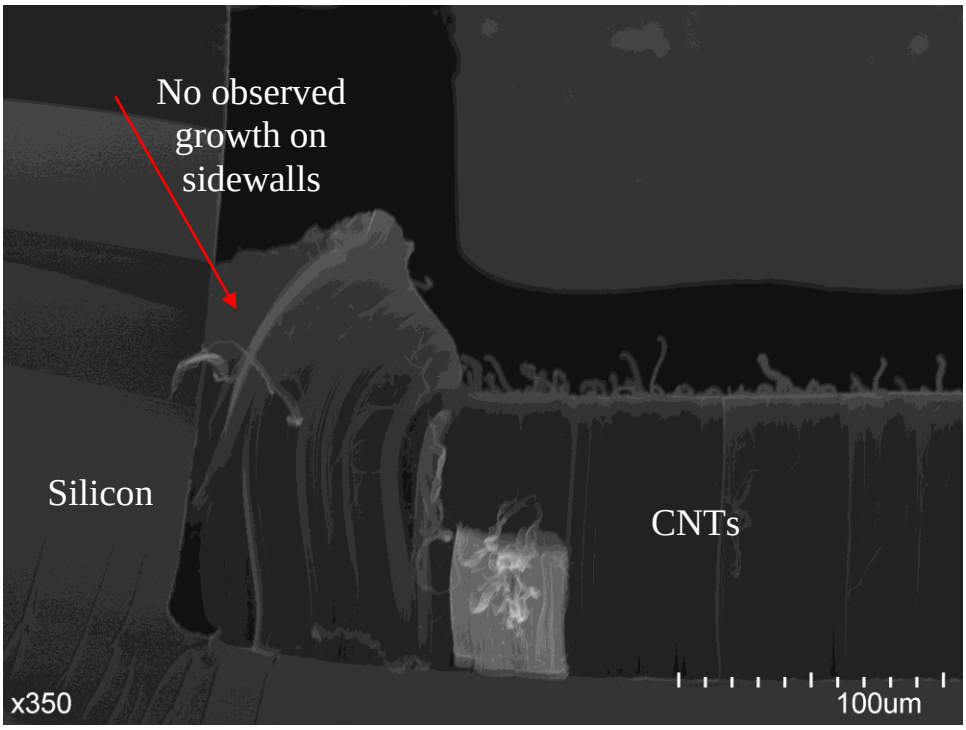

Figure 13: View of cross section of an electrode showing the desired negative sidewall profile and resulting in no CNT growth on the sidewall.

The following recipe is used to achieve the desired profile and roughness – SF_6 is flowed over the patterned silicon at 450 sccm for 2 minutes. Next, C_4F_8 and SF_6 are cycled in the chamber flowing at 250 sccm and 450 sccm for 3 sec and 7 sec, respectively. The gas flows are adjusted slightly over the process time until C_4F_8 and SF_6 are flowing at 220 sccm and 460 sccm for 3.5 sec and 7.25 sec, respectively.

3.4. Electrode Fabrication

CNT growth requires a catalyst and diffusion barrier. Alumina is a traditional and well known diffusion barrier, however the high resistance of alumina is not ideal as an electrode material. For this reason, a metal catalyst stack of titanium, aluminum, and iron (Ti/Al/Fe) was chosen and characterized in this work.

The Ti/Al/Fe catalyst stack used in this work was deposited in an EvoVac deposition system *(Angstrom Engineering, Kitchener, ON, Canada).* Each metal is deposited consecutively in the same vacuum chamber without venting to prevent oxidation. Titanium was deposited first by electron beam evaporation, directly onto the exposed silicon, to a thickness of 20nm. The titanium was then coated with 10 nm of thermally evaporated aluminum. Lastly, 2.8 nm of iron was deposited by electron beam evaporation on top of the aluminum. The entire wafer was then removed from the EvoVac and cleaned with acetone, methanol, isopropyl alcohol, and deionized water and dried by blowing nitrogen. The wafer was then spincoated again using SPR 220-7 photoresist and the aforementioned recipe. This layer of resist is used to protect the catalyst stack from contamination during dicing.

A KnS 900 dicing saw *(Kulicke and Soffe®, Singapore)* is then used to make 275 μm deep dice lines in between each of the catalyst coated pits. These lines are used later to guide a cleave and separate the catalyst coated pits into 10 mm x 10 mm chips with the pits centered in each chip. After forming the dice lines, electrolyte fill ports are cut into the chip. For this, the dicing saw is set to cut 225 μm deep and is used to make consecutive cuts on the inside of the center features. Consecutive cuts are made until a 1 mm wide abscess is formed. The same procedure is used on the opposing side of the pits. The wafer is cleaned and the photoresist removed with acetone, methanol, isopropyl alcohol, and deionized water, and then dried with flowing nitrogen. Lastly, the wafer is subjected to an oxygen plasma descum to ensure any residual resist is removed before CNT growth.

3.5. Chemical Vapor Deposition synthesis of Carbon Nanotube Electrodes

After dicing the wafer and forming the electrolyte fill ports, CNTs can be grown. The CNTs are grown in an Black Magic PECVD furnace *(Aixtron SE, Herzogenrath, Germany)*, shown in Figure 14. There are two heaters, the top heater and the substrate heater. The temperature is measured by three sensors, two thermocouples situated slightly above and below the substrate, and an infrared sensor located near the top heater measuring the temperature at the sample. The thermocouples and infrared sensor are used to control the temperature below and above 550°C, respectively. The process gases, nitrogen, acetylene, and hydrogen, are flown over the top of the sample through a shower head which provides uniform growth over the entire wafer.

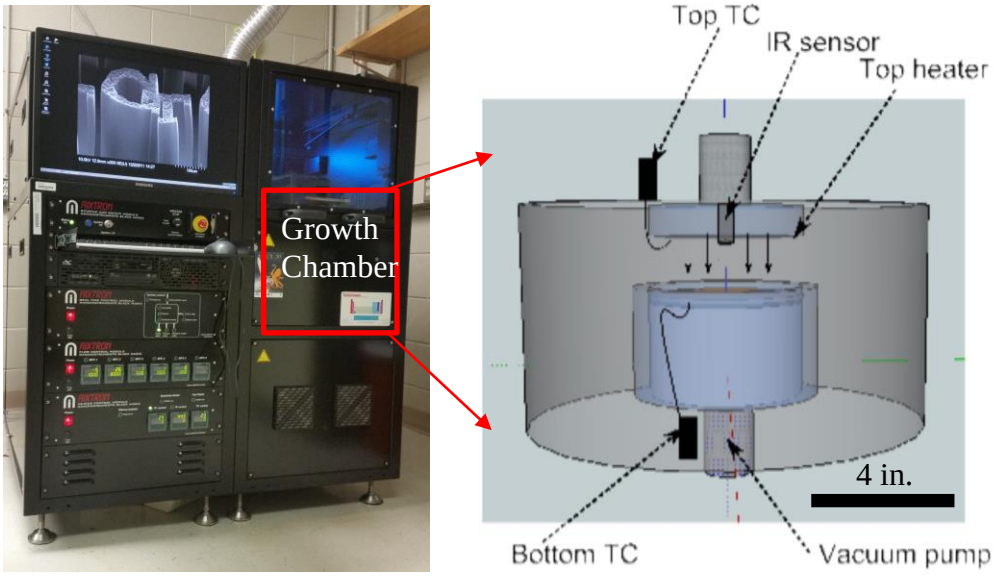

Figure 14: (left) Full view of Black Magic PECVD tool. (right) Schematic of PECVD growth chamber.

The process recipe for CNT growth begins by heating the sample to 510°C in a nitrogen atmosphere. Once the infrared sensor measures 510°C, hydrogen is flowed over

the sample and the sample is annealed for five minutes in an atmosphere of hydrogen and nitrogen. After annealing, the sample is heated to the growth temperature of 800°C. Once the sample reaches 800°C a combination of hydrogen and acetylene is flown across the sample at 320 sccm and 160 sccm, respectively, for the duration of the growth time. In this work, CNTs were grown to heights between 50 – 110 µm. Figure 15 shows an example temperature, pressure, and gas flow profile for this process.

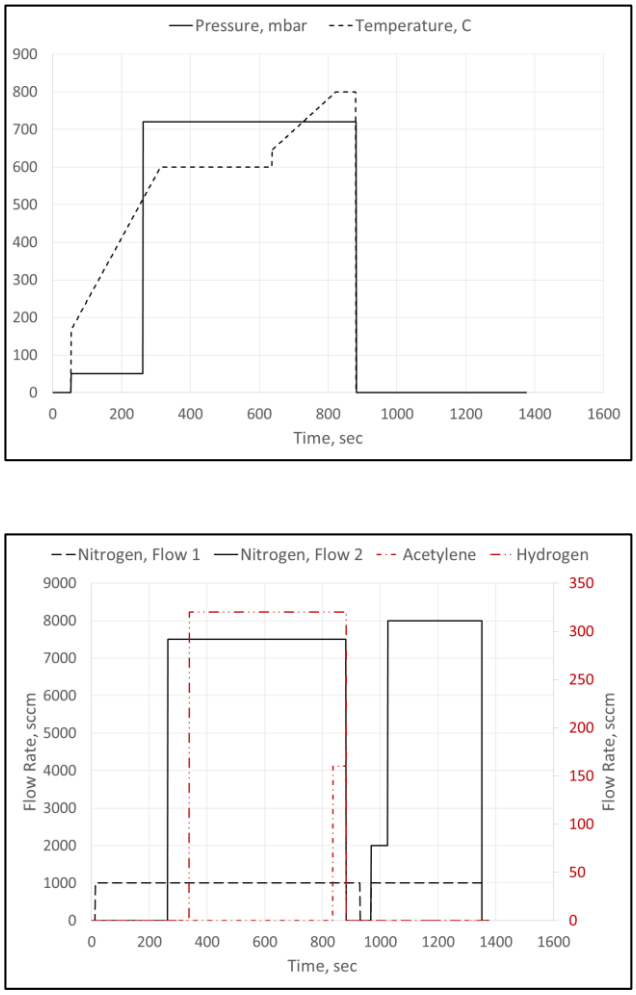

Figure 15: (Top) Pressure, solid black line, and temperature, dotted black line, profiles for CNT growth. (Bottom) Gas flows for two nitrogen flows, black solid and dashed lines, acetylene flow, dash dot red line, and hydrogen flow, dash double dot red line, to achieve high growth CNT electrodes. The red/dotted lines are scaled to the secondary axes on the right.

3.6. Functionalization of Carbon Nanotube Electrodes

3.6.1. Carbon Modified Carbons

Functionalizing CNTs with carbon foliates is possible through damaging the carbon substrates and providing a carbon source, usually a carbon based gas, to produce free carbon radicals that can attach to the CNTs. In this work, the carbon nanotubes are heated to 800°C and exposed to an 80W, 15kHz, argon plasma for 5 minutes. The carbon nanotubes acted as their own carbon source to produce carbon foliates and therefore no carbon based gas was used.

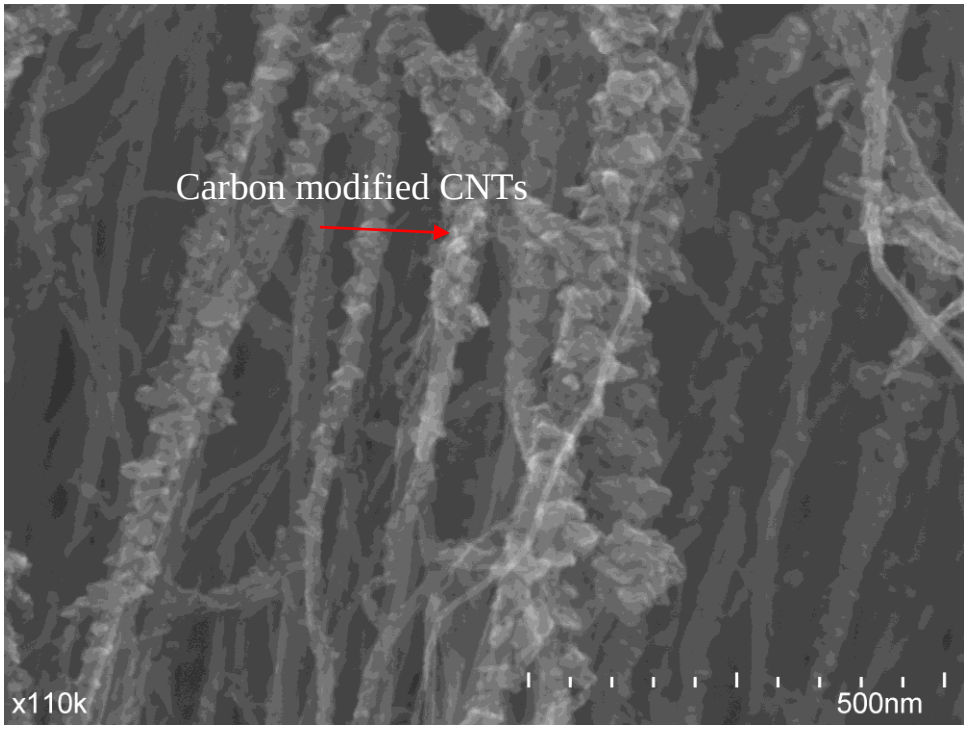

Figure 16: Carbon modified CNTs displaying carbon foliates.

3.6.2. Atomic Layer Deposition

Chapter 2 discussed the fundamental aspects of atomic layer deposition. In this work, four different ALD coatings were used, titanium oxide (TiO_x), titanium nitride (TiN_x), zirconium oxide (ZrO_x), and zirconium nitride (ZrN_x), deposited by a FIJI ALD system *(Vecco-CNT, Waltham, MA, USA)*. Each coating is shown in Figure 17 – Figure 20. The process gases for each are listed in Table 4. Each recipe was run for 140 cycles alternating between the precursor gas and the reactant gas for 0.06 sec and 0.2 sec, respectively, with a 45 sec wait between pulses. X-ray photoelectron spectroscopy (XPS) was used to characterize the resulting thin films which revealed some oxygen and carbonaceous contamination in the samples. The extent of contamination and its effects will be discussed in a later chapter.

Table 4: Process gases used for atomic layer deposition of pseudocapacitive coatings

Pseudocapacitive	Precursor Gas	Reactant
TiO_x	TDMAT (Tetrakis(dimethylamido)Titanium(IV))	Water (H_2O)
ZrO_x	TDMAZr (Tetrakis(dimethylamido)zirconium(IV))	Water (H_2O)
TiN_x	TDMAT (Tetrakis(dimethylamido)Titanium(IV))	Nitrogen (N_2)
ZrN_x	TDMAZr (Tetrakis(dimethylamido)zirconium(IV))	Nitrogen (N_2)

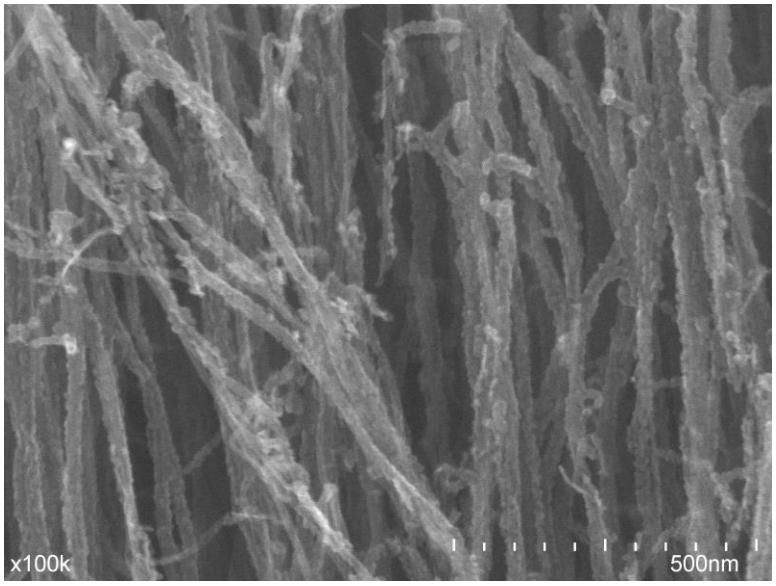

Figure 17: TiO_x coated CNTs.

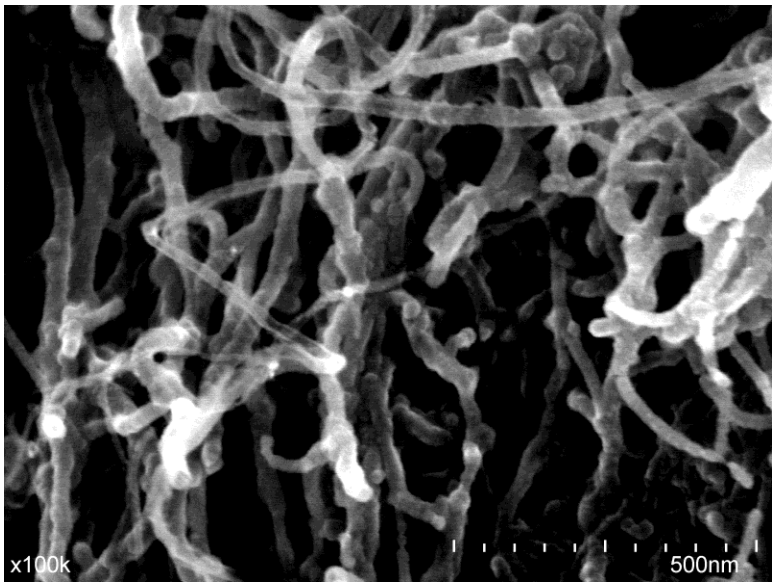

Figure 18: TiN_x coated CNTs.

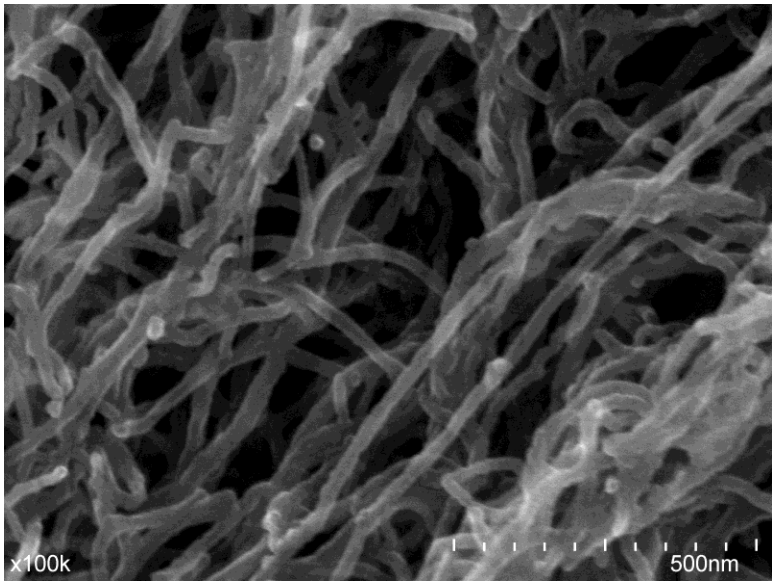

Figure 19: ZrO_x coated CNTs.

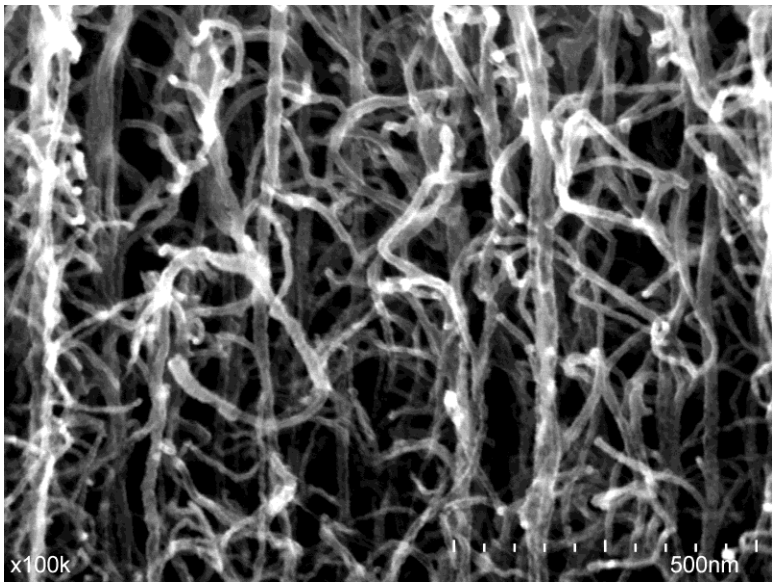

Figure 20: ZrN_x coated CNTs.

3.7. Supercapacitor Assembly

Once the electrodes are fabricated, a pair of electrodes and a porous (pore size: 2µm) glass fiber separator membrane *(Sigma Aldrich, St. Louis, MO, USA, #MIL: AP2002200)* are manually aligned and adhered together using cyanoacrylate adhesive. Once the three components are bonded together, epoxy is applied around three of the four edges to seal the edges and prevent leaks during filling. After applying epoxy, the epoxy is allowed to cure at room temperature for 24 hours. A single CNT electrode and an assembled supercapacitor, prior to filling, are shown in Figure 21.

The assembled devices are then filled, using a syringe, through the diced fill ports, which have not been sealed with epoxy, while in a nitrogen filled glove box, with ~50µL of electrolyte. The separator membrane serves a dual purpose here – (1) The separator membrane is used to prevent short circuits among the opposing CNT electrodes through either stray floating CNTs, unusually long CNTs, or nitride coated electrodes, and (2) as a stop for the syringe to touch before the syringe tip hits any CNTs which may cause them to shear off. Finally, the filled device is then sealed on the fourth side with epoxy and dried for 24 hours.

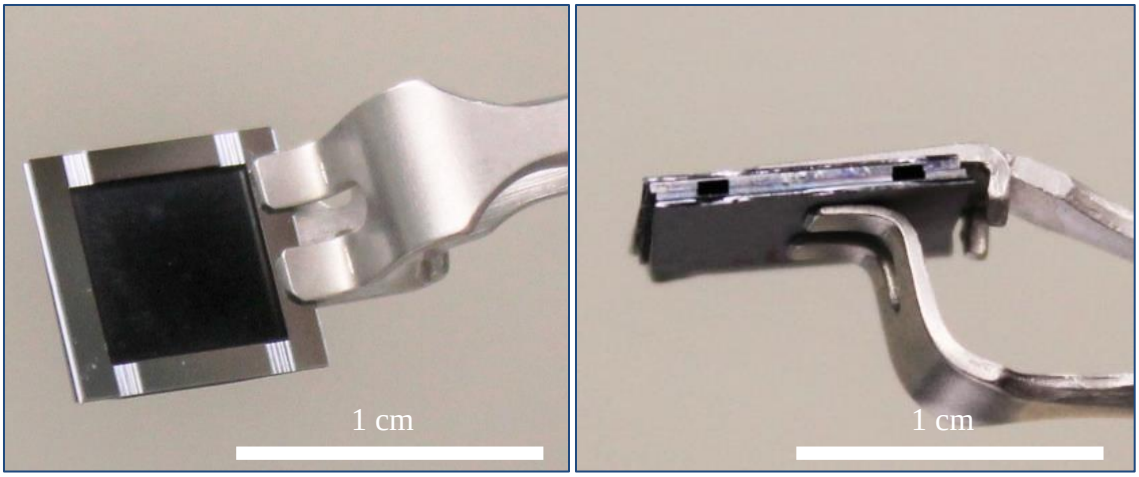

Figure 21: (left) Single carbon nanotube electrode with fill ports (right) assembled device showing fill ports prior to filling with electrolyte. (Photo courtesy of Gloria Bowen)

3.8. Analysis of Electrodes and Assembled Devices

3.8.1. Scanning Electron Microscopy

Scanning electron microscopy (SEM) was conducted on a Hitachi 4800 SEM *(Hitachi, Ltd., Tokyo Japan)* to evaluate the height of the CNT forest and relative diameter of the CNTs and functionalized CNTs. Each sample was imaged at accelerating voltages between 5-15keV, various magnifications, and many locations across the sample. Measurements of some nanotube diameters were taken using Quartz PCI software, particularly to visualize and quantify the difference in diameter between plain CNTs and their functionalized counterparts.

Some samples were imaged after being filled with electrolyte on a Hitachi S-3700N *(Hitachi, Ltd., Tokyo Japan)* variable pressure SEM. These images were used to reveal

information in regards to failure of the devices and the interaction of the IL electrolyte with the CNT electrode. However, cleaving of the silicon current collector and cutting the separator membrane was highly destructive which made imaging these samples difficult. Therefore, only a few SEM images will be presented from full devices.

3.8.2. Electrical Characterization

An Arbin battery cycler *(Arbin Instruments, College Station, TX, USA)* was used to perform both CV and CD tests on the fabricated supercapacitors. The Arbin battery cycler has a voltage range of +/- 5V, a current range of 3µA to 500mA, and utilizes a four point probe method to apply and measure both current and voltage. The current range is distributed amongst three configurations, low current, medium current, and high current, with current ranges of +/- 3-300µA, +/- 300µA-50mA, and +/- 50-500mA respectively. Using a current in the incorrect configuration would have one of two results. If the measured current is too high for the configuration, the current would be limited, i.e. applying 1mA while in the low current range would result in a current of 300µA being applied. If the measured current is too low for the configuration, the device is less sensitive to current changes and would increase any inaccuracies. For these reasons, the corresponding range was used for the desired constant current test.

There were no leads fabricated directly onto the silicon electrodes in the present work. Therefore, a traditional coin cell battery holder was used in order to create contact on both electrodes. Utilizing a coin cell battery holder ensured consistent contact surface area and pressure between all samples. An image of 10 supercapacitors being tested is shown in Figure 22.

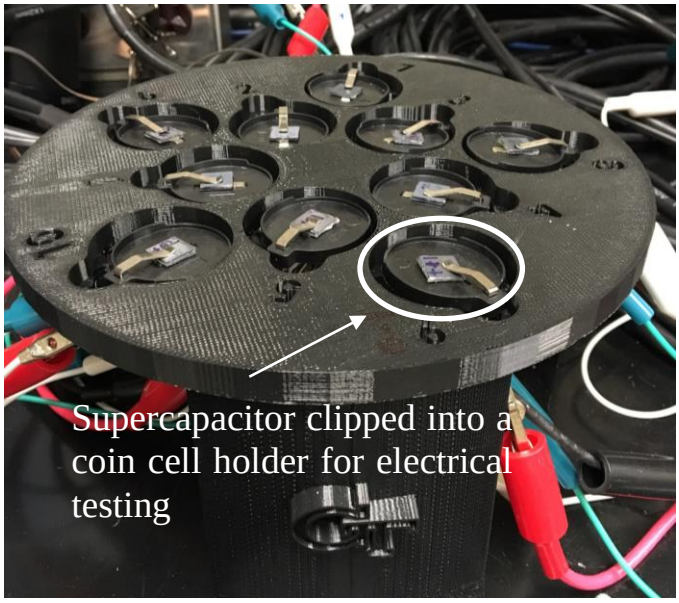

Figure 22: Microfabricated supercapacitors utilizing battery coin cell holders as connections for electrical tests.

3.9. Chapter Summary

This chapter has consisted of a full description of the fabrication process of the presented supercapacitor architecture including materials, lithography, and etch processing. A short discussion of the methods for growing CNTs and the functionalizations are presented. Lastly, the respective characterization techniques and procedures were also discussed.

CHAPTER 4

RESULTS AND DISCUSSION

4.1. Analysis of Current Collectors

The silicon current collectors were analyzed with CV at a scan rate of 4mV/sec from -1 to 1 V. These measurements were taken on the Arbin battery cycler, however, the observed current is difficult to interpret due to the resolution of the tool with an error of 0.3µA. These were also highly resistive samples as can be seen by the slanted CV curve as shown in Figure 23 – Figure 24. The capacitances of all samples without CNTs are displayed in Figure 25. The samples had similar capacitances which is to be expected because each IL had similar dielectric constants.

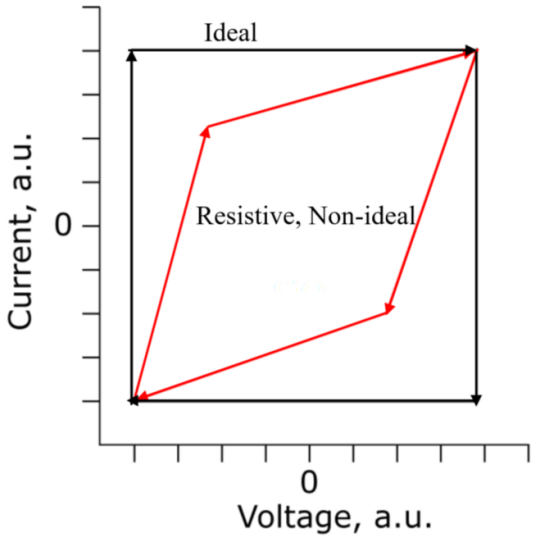

Figure 23: (black) Ideal cyclic voltammetry curve and (red) resistive capacitor where the area is proportional to capacitance.

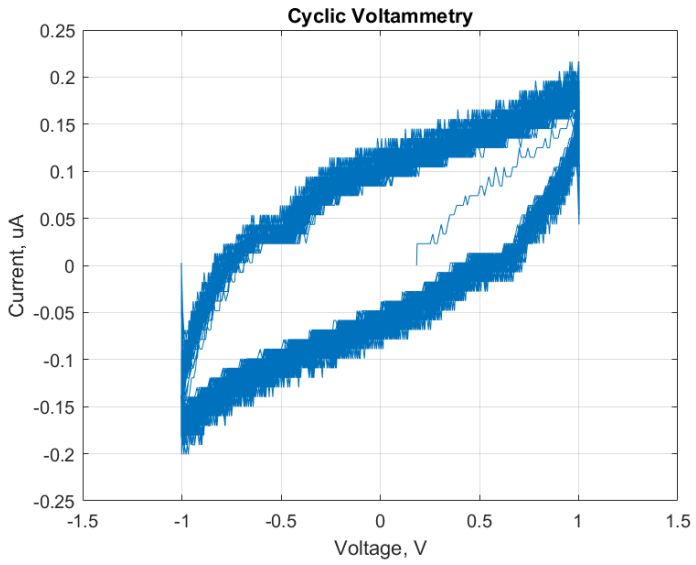

Figure 24: Silicon current collector without CNTs operating with IL A.

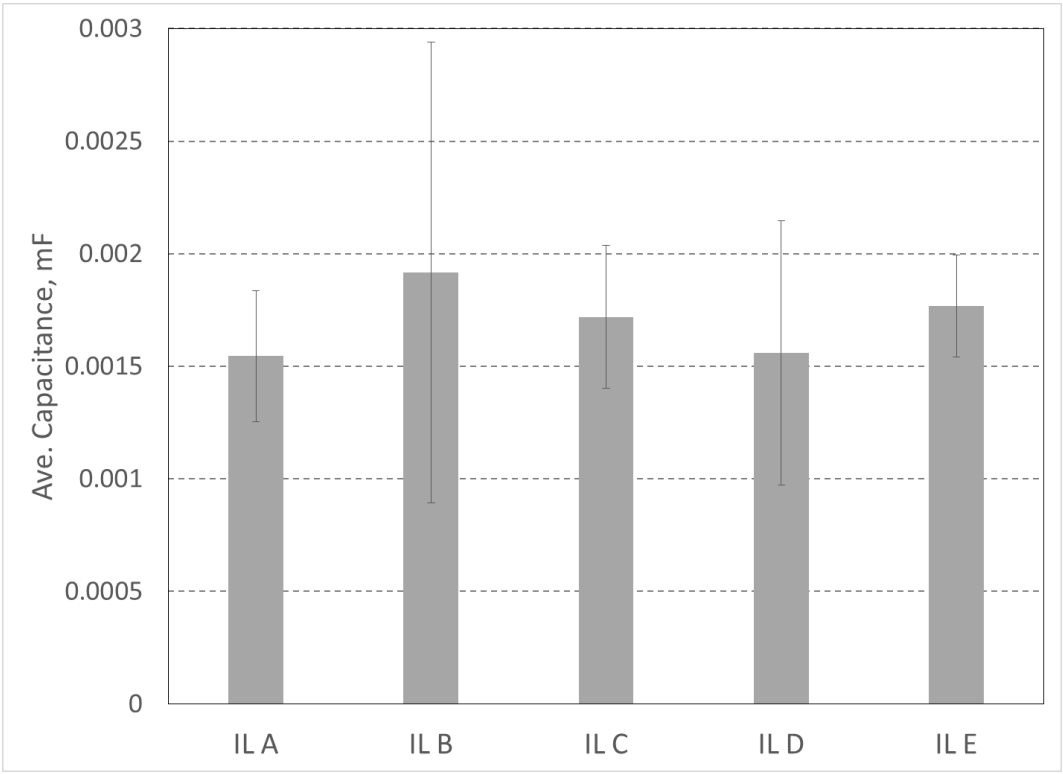

Figure 25: Capacitance measurements of silicon current collectors without carbon nanotubes.

4.1.1. Life Cycle Tests

Typically, batteries operate for a few thousand cycles, and capacitors for several hundred thousand cycles. Supercapacitors usually have lifecycles between both devices depending on the primary mode of charge storage. Life cycle tests were conducted for 200,000 cycles on some capacitors to test the longevity of the CNT based supercapacitors. These CNT electrodes had no functionalities and therefore operate on the Helmholtz double layer energy storage mechanism.

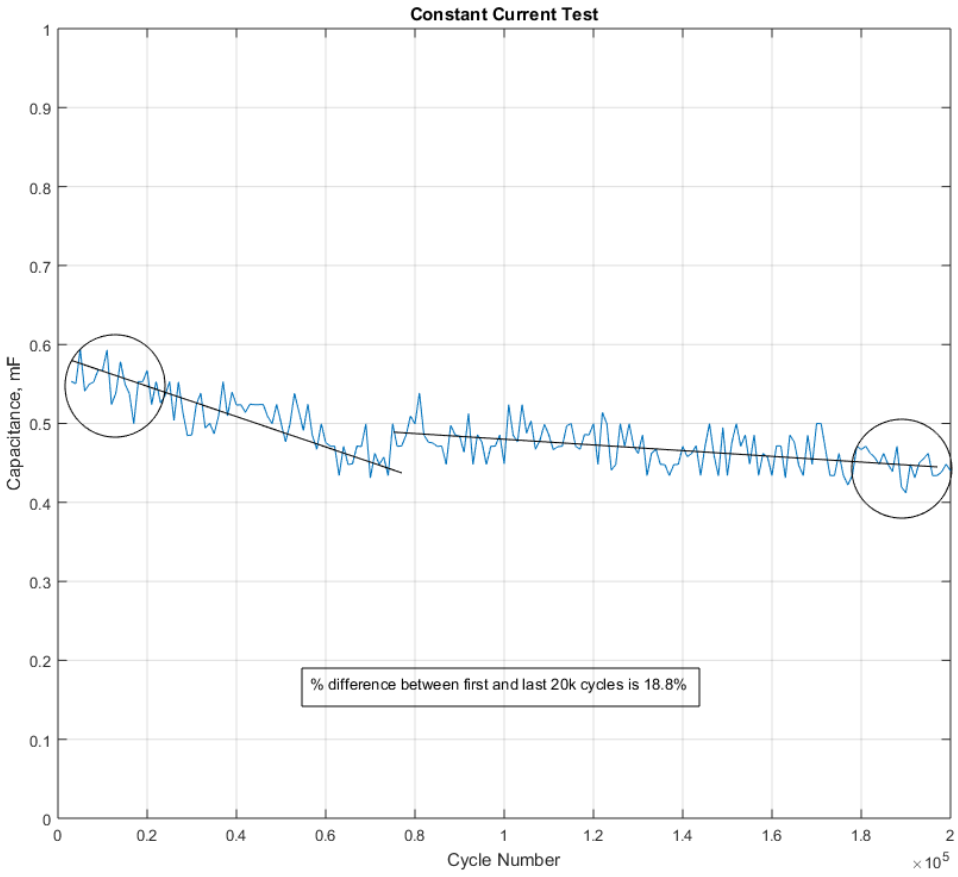

Figure 26: CNTs and IL C 200k life cycle test.

It is viable that supercapacitors should survive at least a 200,000 life cycle test. For these tests, every 1,000th cycle is recorded and a percent difference between the first and last 20,000 cycles is calculated. This is shown in Figure 26. By industry definition, a capacitor is considered past its lifetime after degrading 25% of its capacitance, or gaining 100% ESR [60]. After, 200,000 cycles, the Helmholtz double layer capacitors without pseudocapacitive coatings survived. However, these tests have not yet been carried out on supercapacitors with pseudocapacitive coatings.

4.2. Scanning Electron Microscopy

Scanning electron microscopy was integral in this work for initial characterization of the carbon nanotube forests, the current collector shape, and the pseudocapacitive coatings. Figure 27 shows example measurements taken on the CNT forest as well as the uniformity in growth height. Bent CNTs are artifacts from cleaving the sample for a cross section view of the CNT forest. Figure 28 (left) shows a fully assembled supercapacitor that had been filled. After cleaving, the electrolyte drained out but remained wicked into the CNT forest. Defects that are shown are a result from cleaving the chips and cutting the separater membrane. As observed in Figure 28 (right), the IL electrolyte coats the CNTs completely and wicks to even the bottom of the CNT forest.

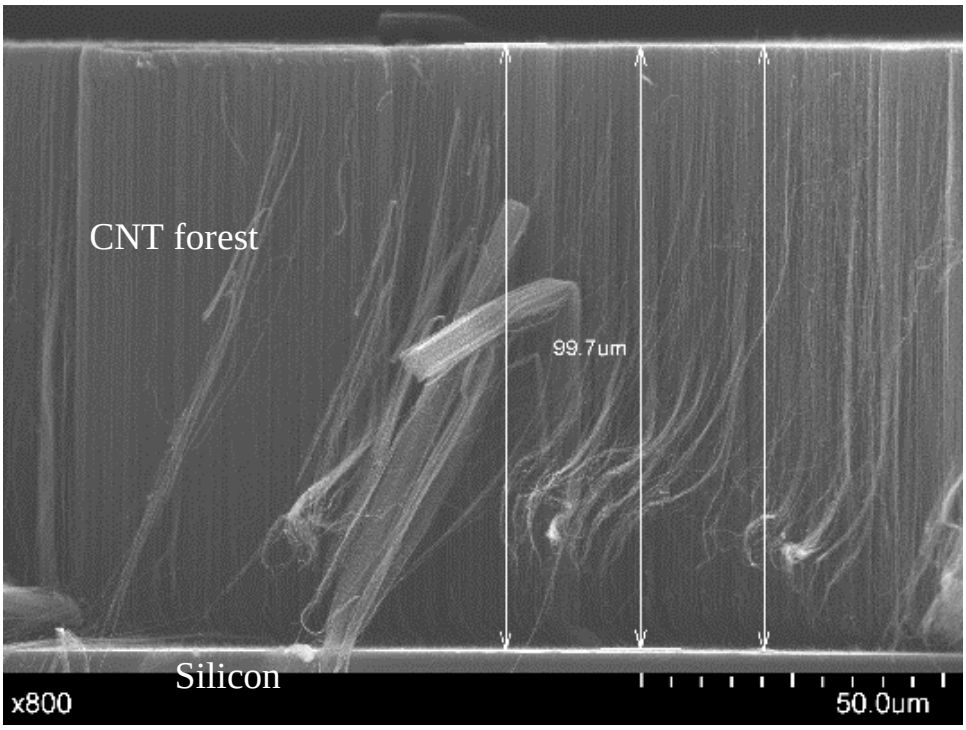

Figure 27: CNT heights measured using Quartz PCI software. Uniformity is observed across the entire sample.

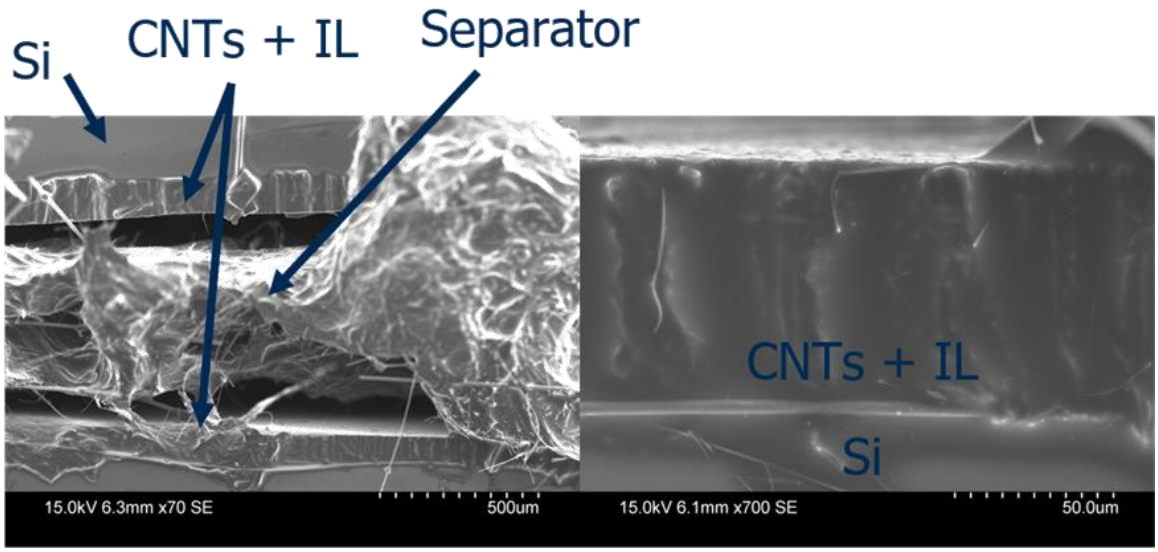

Figure 28: SEM images taken on a variable pressure SEM. (Left) Fully assembled and filled supercapacitor (cleaved and therefore cavity is not entirely filled). (Right) CNT forest becomes entirely coated with IL when filled.

Growth of carbon foliates is a possible method to drastically improve capacitance. This method, increases surface area of the electrode, and defined by equation 3, the capacitance improves proportional to the area. The aforementioned carbon foliate growth recipe had limited success. Successful carbon foliate growth occurred when the plasma would arch to the CNT forest. This created a crater within the forest as shown in Figure 29 (left). The crater created a number of free carbon radicals and damaged the surrounding CNTs. The radical carbons then were able to attach to the CNTs and create carbon foliates as shown in Figure 29 (right). When plasma instabilities did not strike the CNT forest, only limited formation of carbon foliates occurred as shown in Figure 30. These results indicate that a higher temperature, or higher plasma power, like a plasma instability, are needed to fully functionalize the CNTs. Carbon foliates on CNTs were not used in the following capacitance investigations due to inconsistency of the growth process.

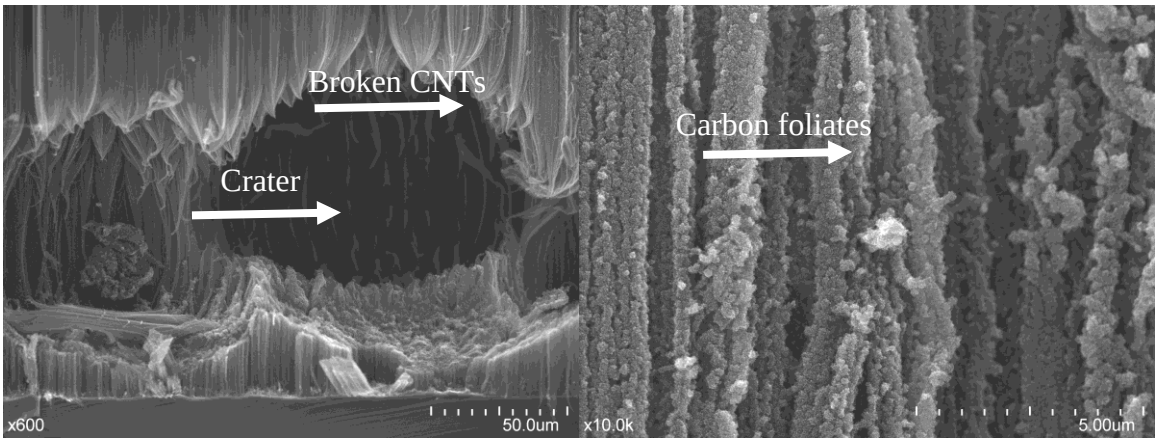

Figure 29: (left) Craters formed from plasma instability striking CNT forest during PECVD growth of carbon foliates. (right) Carbon foliates formed from carbon radicals after damaging the CNTs with plasma.

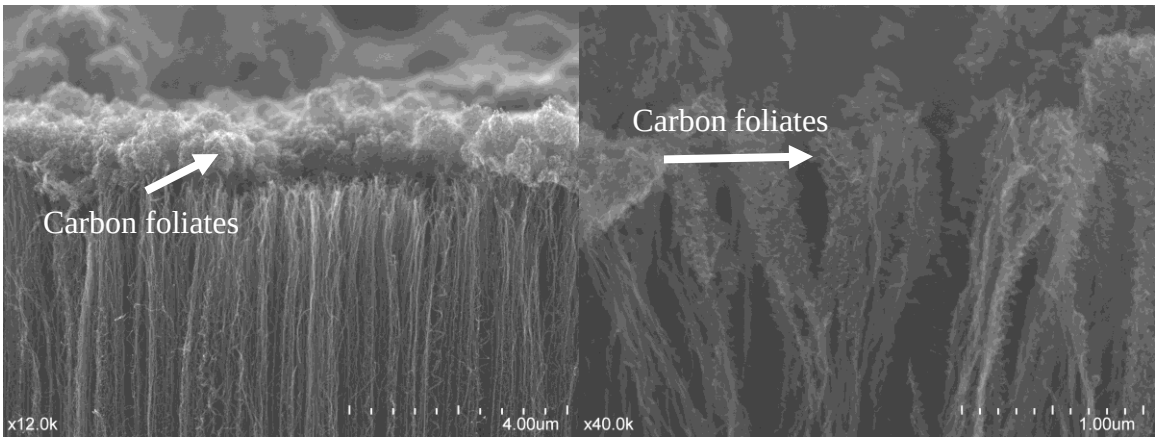

Figure 30: Limited carbon foliate formation on the tips of CNTs in areas that were not struck by high energy plasma instabilities.

4.3. X-ray Photoelectron Spectroscopy

XPS was used to assess the characteristics of the samples. Each of the samples are fabricated in a user facility where it is likely that unintended materials can be deposited on the samples during ALD. The measurements were taken on the outside edge of the supercapacitor electrode, between the CNT forest and the edge of the chip. This testing location was chosen, instead of testing on the CNT forest, in order to mitigate any unusual measurements from the CNT forest. In the measurements, particular attention was on the expected binding energies for Ti-2p, Zr-3d, O-1s, N-1s, C-1s, and Si-2p. Ti and Zr were only analysed for the corresponding oxide and nitride.

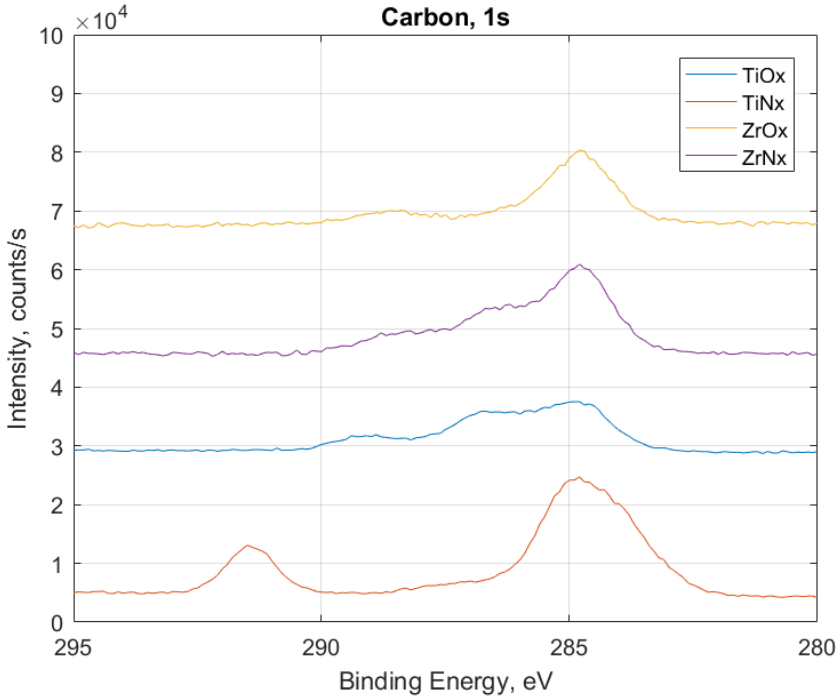

Figure 31: All data shifted to strongest carbon peak. Peaks from 285-290 eV are expected to be carbonates and other loosely bonded carbons from leftover resist or ALD process gases.

The strongest carbon peaks (Figure 31) were shifted to standard single bonded carbon at 284.8eV. Peaks from 285-290eV are expected to be present when there are carbonates and other carbon, oxygen, and hydrogen bonds present on the sample. These were likely introduced to the samples from processing. TiO_x, ZrO_x, and ZrN_x all show broad, weak peaks in the 285-290eV regime. The presence of excess ligands can be confirmed with the secondary oxygen peaks in ZrO_x and ZrN_x. TiO_x also showed a subtle, secondary, peak at 532 eV in the oxygen spectra. Outside of the 285-290 eV range for carbon, TiN_x showed a strong peak at 291.5 eV which correlates with π- π* satellite bonding [61].

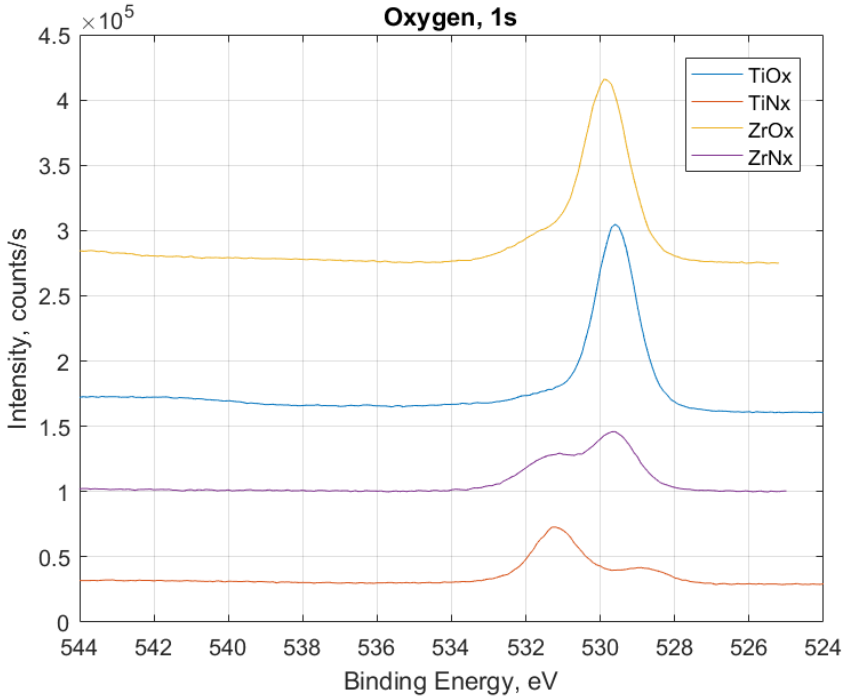

Figure 32: Oxygen spectra showing strong oxygen peaks for oxide samples and the presence of oxygen in nitride samples.

In the O1s regime, strong peaks are expected in the range of 528-530 eV depending on the covalency of the bonding. Due to their covalency, metal oxide bonds typically reside in the 529-530 eV range [61]. ZrO_x and TiO_x show strong peaks near 530 eV as expected, shown in Figure 32. However, ZrN_x also shows a strong peak near 530 eV which suggests oxygen contamination or oxidation of the samples during/after fabrication. The TiN_x, ZrO_x, and ZrN_x samples all have secondary peaks near 531.5 eV which correlates to organic single bond CO [61]. This peak is particularly prominent in the nitride samples. This would suggest that the ALD process was not optimized. The reactions taking place may not have finished before switching gases. In this case, ligands may have been left from the Zr/Ti precursor gases and were unreacted with the nitrogen plasma. Increasing gas flow or plasma power may help mitigate these issues in future experiments.

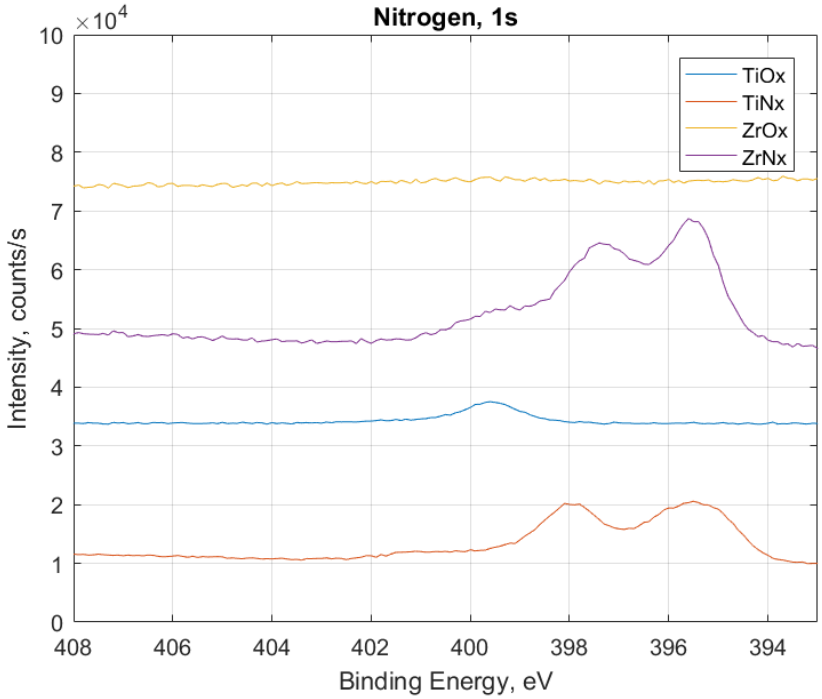

Figure 33: Strong nitrogen peaks were observed for the nitride samples. A peak was also observed in TiO_x but is expected to be from carbonaceous amino groups.

Strong nitrogen peaks were observed in the nitride samples as expected as shown in Figure 33. N1s peaks are expected for TiN and ZrN at 397.3 eV [62] and 397.5-397.7 eV [63], respectively. There is a ZrN_x peak observed at this location, however there is a secondary peak near 395.5eV and a satellite peak near 400 eV. This secondary peak is likely formed from the presence of oxynitrides. It has been previously shown that the presence of oxygen in metal nitrides (and therefore oxynitrides) will shift peaks to higher energies [64]. A peak is observed in TiN_x near its expected region (397.3 eV) but the peak is located nearer 398 eV. The oxygen spectra supports these explanations as both nitride samples had significant amounts of oxygen present. A nitrogen peak was also observed in the TiO_x spectra. This was unexpected, however is likely due to process contamination

resulting in nitrogen in the film. Carbonaceous amino groups (i.e. CNH_2) exhibit nitrogen peaks near ~400eV [61] which aligns well with the observed peak.

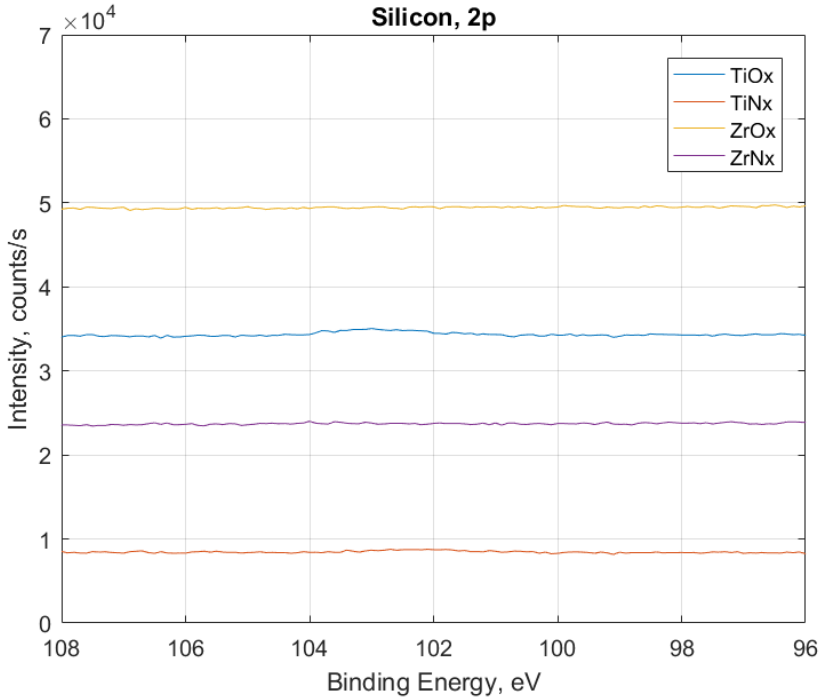

Figure 34: No silicon peaks were observed which suggests the layer thickness is greater than ~10nm.

No peaks were measured in the silicon regime, Figure 34. This confirms that there is no silicon contamination from the user facility, and the thickness of the deposited coating is greater than ~10nm where the underlying silicon is no longer being detected.

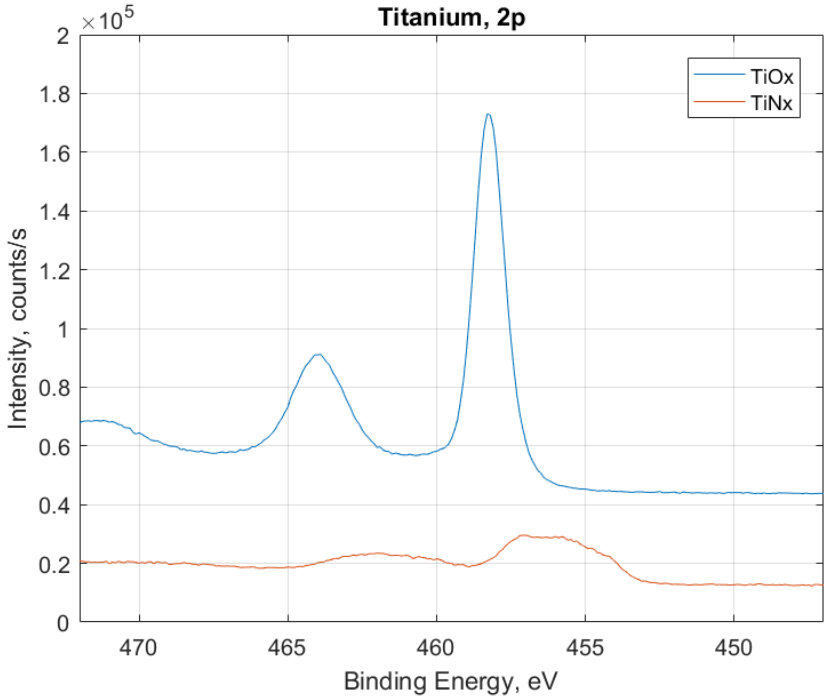

Figure 35: Ti spectra for the Ti based samples. Broad peaks in TiN_x suggest the presence of oxynitrides.

Strong Ti peaks were observed in both Ti samples, however, the peaks in TiN_x were broader as shown in Figure 35. The strongest Ti peak in TiO_x is located where Ti $p_{3/2}$ is expected (458.5 eV [61]). A secondary peak is observed in TiO_x at ~464 eV which corresponds to the TiO_2 $p_{1/2}$ peak. TiO_2 also exhibits a satellite peak at 472 eV which is also observed [61]. TiN $2p_{3/2}$ peaks are expected between 454-455 eV with satellite features between 456-458 eV. These peaks are observed, however, TiO exhibits a $Ti2p_{3/2}$ peak at 457.3 eV [63] which may be distorting the peaks in the 454-458 eV region. A secondary peak in the TiN_x spectra is observed at ~462 eV. The TiN $Ti2p_{1/2}$ peak is expected between 460-461 eV with a satellite feature near 464 eV [61]. Both peaks in TiN_x suggest that deviations from TiN, such as the presence of oxynitrides and left over organic ligands, caused the merging of satellite peaks and the strong $Ti2p_{3/2}$ and $Ti2p_{1/2}$ bonds. However,

the peak locations suggest that the TiO_x sample is comprised of TiO_2 and the TiN_x sample is a mixture of TiN and TiN_xO_y.

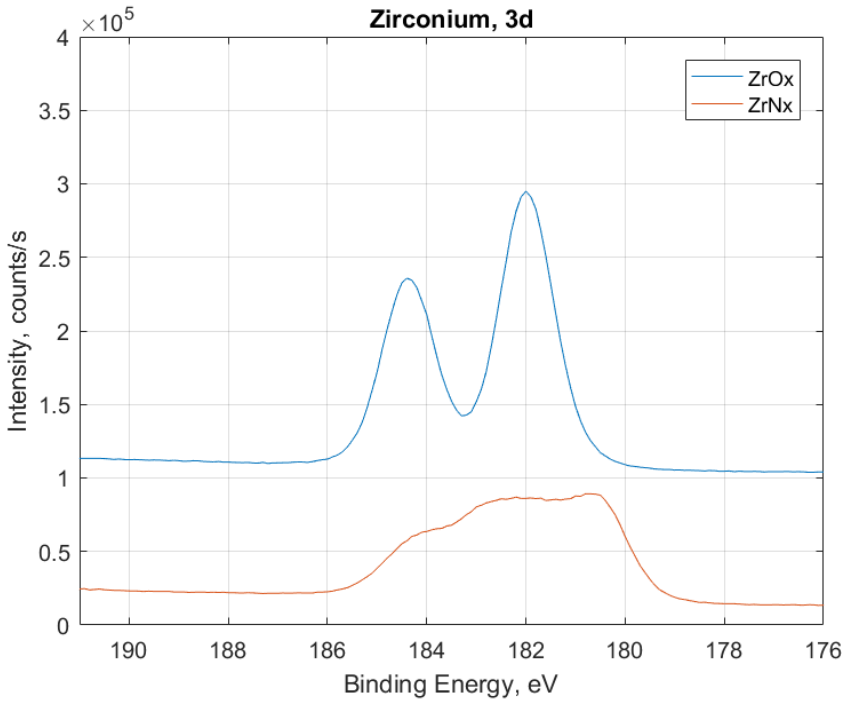

Figure 36: Zirconium peaks were observed in both Zr based samples. However, ZrN_x is much broader which suggests the presence of oxynitrides.

Peaks are observed in both Zr samples as expected as shown in Figure 36. ZrO_x had particularly well defined peaks at 182 and 184.5eV. These measurements correlate well with the Handbook of Monochromatic XPS spectra [62] which suggests that peaks for ZrO_2 should be observed at 182.5 and 184.85 eV. ZrN_x is less well defined, however, in ZrN, a Zr $3d_{5/2}$ peak is expected at 180.9 eV [63] which is observed in the spectra shown. Zirconium oxynitrides exhibit a peak with a binding energy of 182.2+/-0.3 eV. Increasing oxygen content increases the binding energy [64]. Therefore, the secondary peak near 182.5 eV is most likely a form of ZrO_xN_y. The last peak in the ZrN_x spectrum, at 184.5 eV

is the ZrO_2 present in the sample from process contamination or oxidation from atmosphere.

In general, the oxide samples were less contaminated than the nitride samples. In the nitrogen spectra, ZrO_x did not show signs of nitride contamination, however, a secondary peak in the TiO_x sample, as shown in Figure 35, shows possible nitride contamination. The presented figures demonstrate oxide contamination in all nitride samples. The thickness of the coatings was >10nm as demonstrated in Figure 34.

4.4. Cyclic Voltammetry

CV was chosen to evaluate the capacitance of each sample since pseudocapacitance can be easily observed during data analysis. In this work, CV measurements were made at scan rates of 10, 50, 100, 200, and 500mV/s between the operating voltages of -2.5 to 2.5 V. These scan rates correspond to reasonable discharge rates for supercapacitors which can be anywhere from seconds to 10 minutes [1]. At each scan rate, with the exception of 10mV/s, 1,000 cycles were measured. At 10mV/s, the tests were stopped between 100-300 cycles due to the long length of the test. Current versus voltage, and capacitance versus cycle number plots were created for each test.

4.4.1. Achievable Capacitance

The CNT electrodes used in this work have a mass of approximately 0.3 mg. Peigney et al. have formulated a correlation between specific surface area of CNTs and the number of walls in the MWCNT [10]. The specific surface area of CNTs with 10 walls is approximately 150 m^2/g which results in 0.045 m^2 for the purposes here. Using Equation

3 and assuming d and ε are approximately 1 nm and 15, respectively. Solving for C, yields a capacitance of one Helmholtz double layer of 6 mF. Adding the two Helmholtz double layer capacitances in series results in an expected capacitance, for a non-functionalized CNT supercapacitor, of 3 mF.

4.4.2. Effects of Scan Rate

Scan rate has been known to have significant impacts on the achieved capacitance when measured with CV [31]. This is particularly important for determining capacitance for high power applications where faster scan rates would take place. Figure 37 – Figure 46 show the effects of scan rate on capacitance and energy density differentiated by pseudocapacitive coating. Energy density is proportional to V^2 and therefore, a sample with a lower capacitance may still have a higher energy density. Therefore it is important to discuss both phenomena simultaneously. In the plots, each point represents a single sample averaged over 1,000 cycles. Error bars are +/- a single standard deviation for those 1,000 cycles.

Without functionalities the capacitance of the samples was limited to below 10mF. 1-Ethyl-3-methylimidazolium bis(trifluoromethylsulfonyl)imide (IL B) and Diethylmethyl(2-methoxyethyl)ammonium bis(trifluoromethylsulfonyl)imide (IL E) exhibited stable capacitances over a wide range of scan rates whereas the other IL electrolytes performed poorly at high scan rates. Due to the low capacitance values, the voltage window has an exacerbated effect when calculating energy density. Figure 42 shows the energy density of plain CNT electrodes, and as expected, IL E outperformed the other ILs due to its 6.5V voltage window.

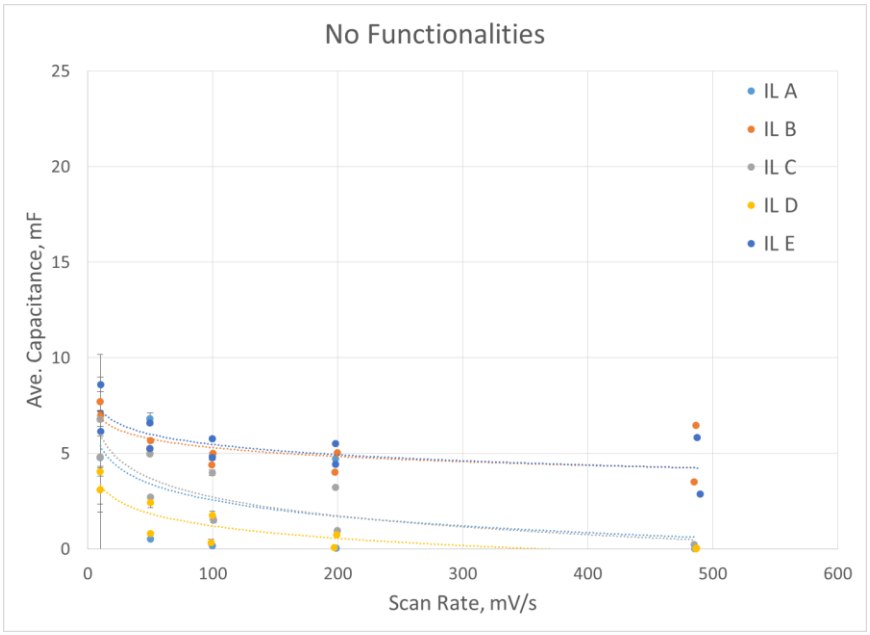

Figure 37: Capacitance versus scan rate without pseudocapacitive coating. Capacitances did not exceed 10mF. A typical degradation of capacitance over scan rate is observed.

The zirconium samples produced a significantly lower capacitance than the titanium based samples. Titanium oxide produced higher capacitance values compared to bare CNT electrodes at 100mV/s. Most TiO_x samples were over 5mF at 100mV/s with IL B and Triethylsulfonium bis(trifluoromethylsulfonyl)imide (IL D) producing the highest capacitance with TiO_x and TiN_x, respectively. IL B and 1-Butyl-1-methylpyrrolidinium bis(trifluoromethylsulfonyl)imide (IL C) produced the highest capacitance with ZrO_x and ZrN_x, respectively. This is particularly interesting since IL B produced the highest capacitance for both oxide samples. This may suggest that the pseudocapacitive reactions occur primarily with the oxygen atoms for IL B in parallel with the traditional Ti^{3+}/Ti^{4+} reaction with oxygen vacancies exhibited by TiO_x [32].

Nitride samples proved to be the most successful in this work. TiN_x paired with IL D is the most promising candidate for functionalized supercapacitors. However, ZrN_x paired with IL C was also effective. Both TiN_x and ZrN_x had high capacitances at 10mV/s at 20.38mF and 16.73mF respectively. At 500mV/s, TiN_x and ZrN_x exhibited capacitances of 1.28mF and 3.42mF, respectively. However, surprisingly, at high scan rates, TiO_x samples, combined with IL B produced the highest capacitance. This could possibly be due to the number of oxygen vacancies available in the TiO_x coating compared to TiN_x.

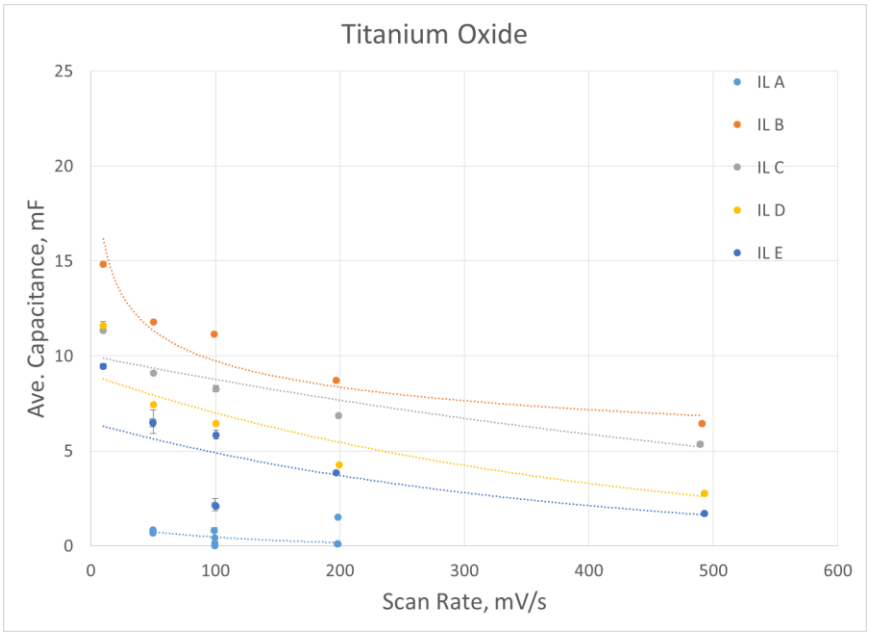

Figure 38: IL B showed the highest capacitance for TiO_x electrodes. IL A under performed and showed no significant reactions with the TiO_x electrodes. Similar degredation of capacitance is shown compared to non-functionalized electrodes.

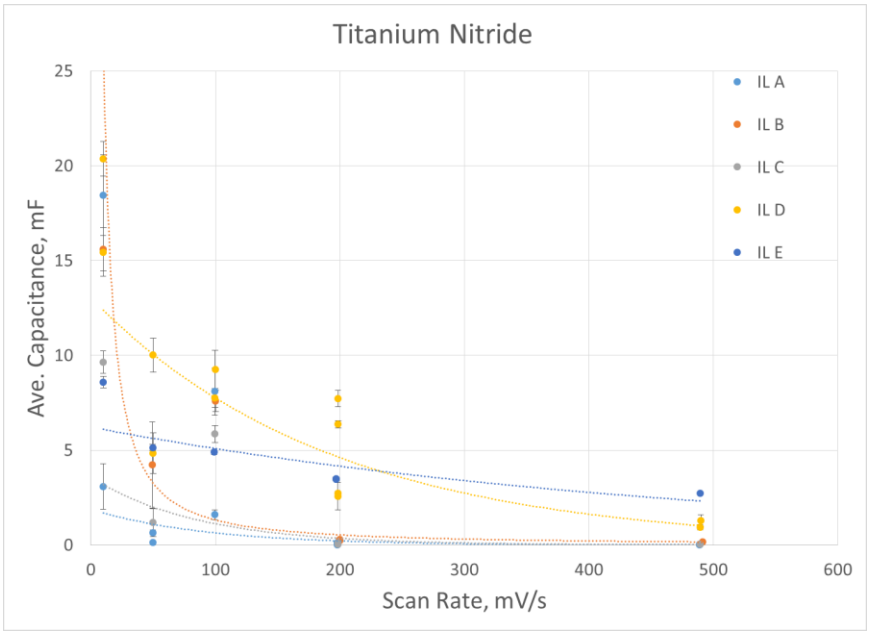

Figure 39: TiN_x capacitance versus scan rate. IL D showed a capacitance over 20mF and the highest stability to 200mV/s. IL E produced the most stable curve over the entire scan rate range, but generally achieved lower capacitance.

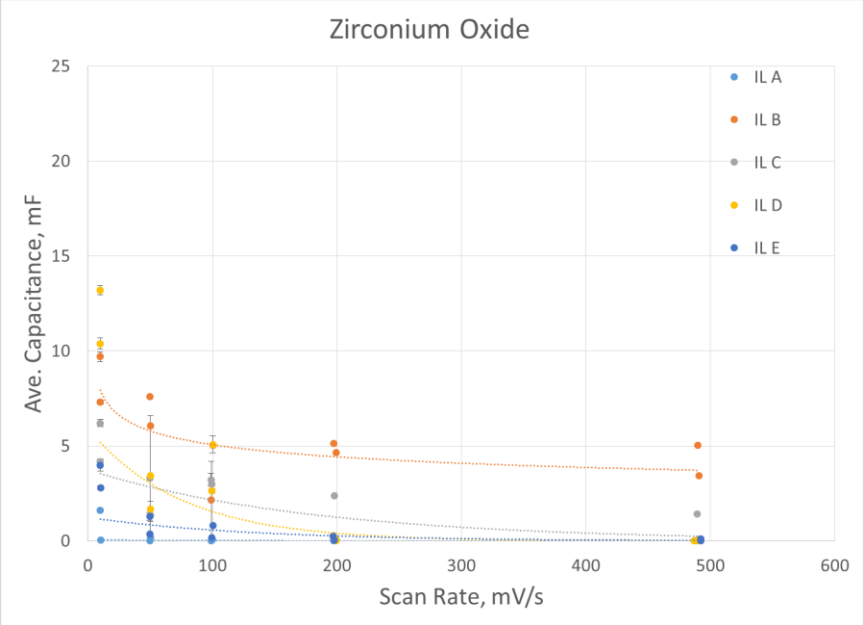

Figure 40: ZrO_x capacitance versus scan rate. IL D demonstrated the highest capacitance at nearly 14mF but was not stable over the scan rate range. IL B exhibited relatively high capacitance at low scan rates and stability over the entire range.

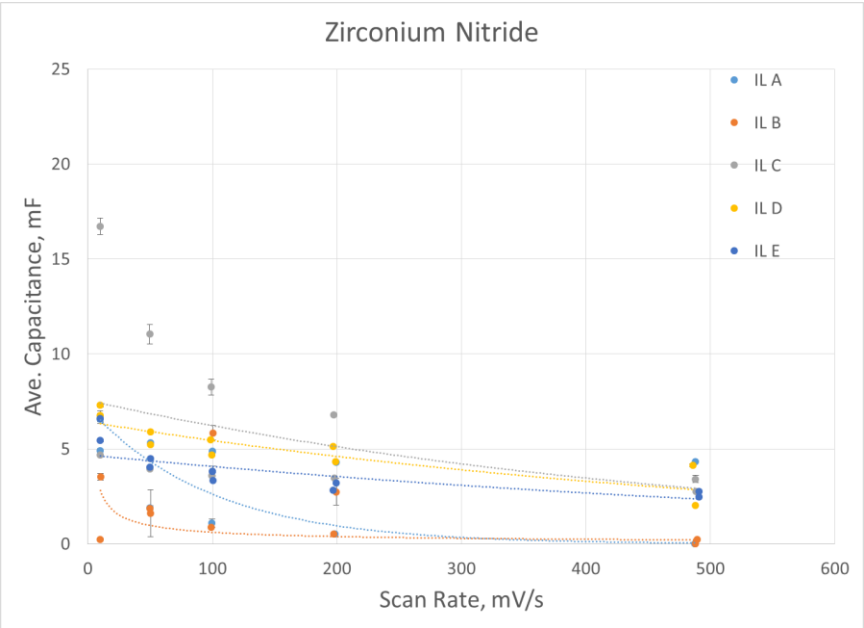

Figure 41: ZrN_x capacitance versus scan rate. IL C produced the highest capacitance over the entire scan rate range. However, the other IL produced much

lower capacitances but were much more stable. IL B underperformed and had relatively low capacitance and stability.

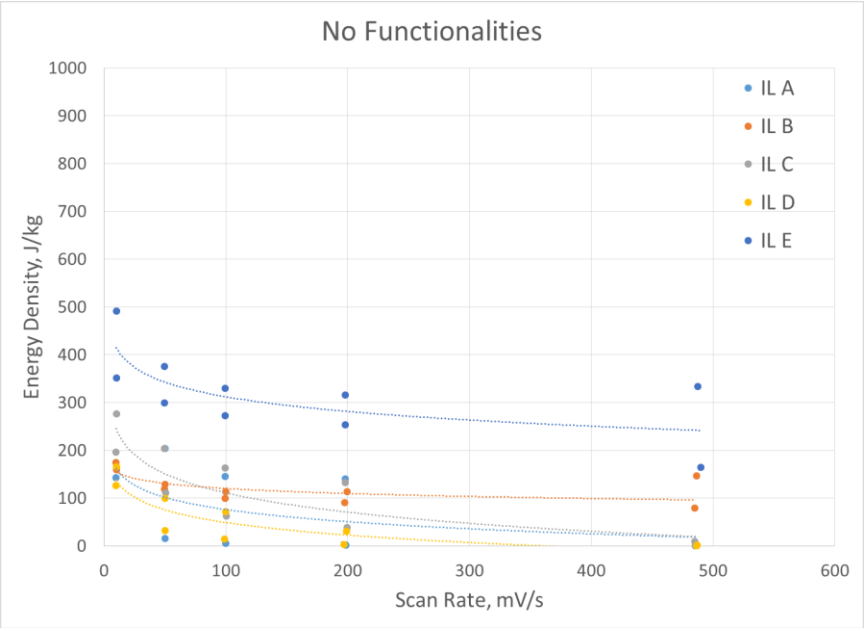

Figure 42: Electrodes without functionalities – Energy density versus scan rate.

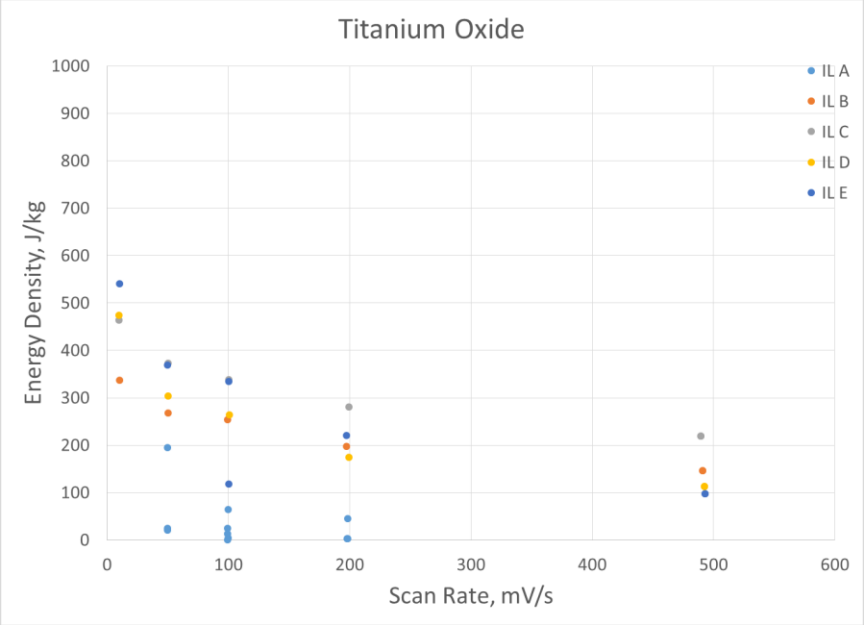

Figure 43: TiO_x energy density versus scan rate. IL E exhibits highest energy density, even though it had the lowest capacitance due to its large electrochemical

window. However, IL is more favorable at higher scan rates, possibly due to its lower viscosity compared to IL E.

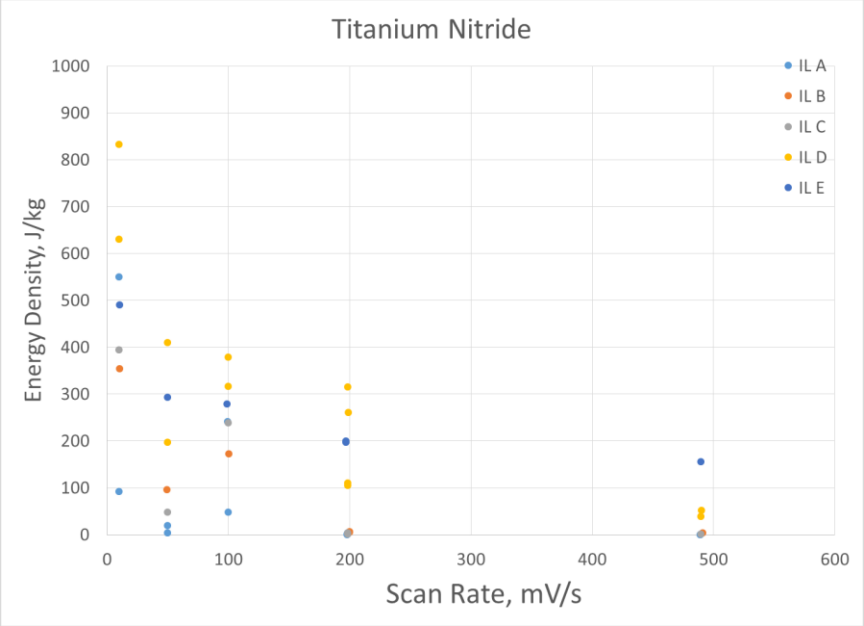

Figure 44: TiN_x energy density versus scan rate. IL D showed similar performance had the highest capacitance due to its large electrochemical window and high capacitance. IL D is less favorable at high scan rates where IL E then dominates.

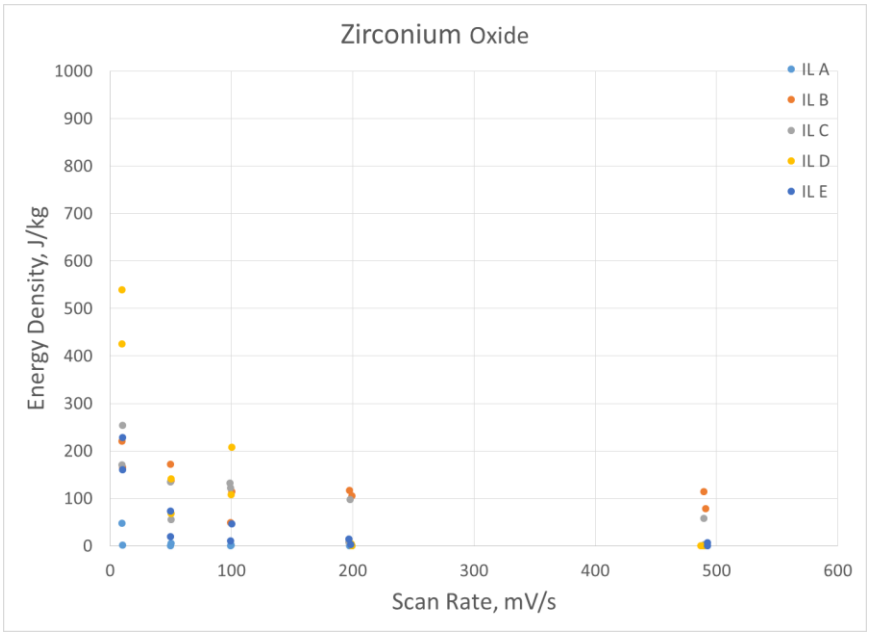

Figure 45: ZrO_x energy density versus scan rate. IL D demonstrated the highest energy density as expected since it had the highest capacitance and a 5.5V operating voltage window.

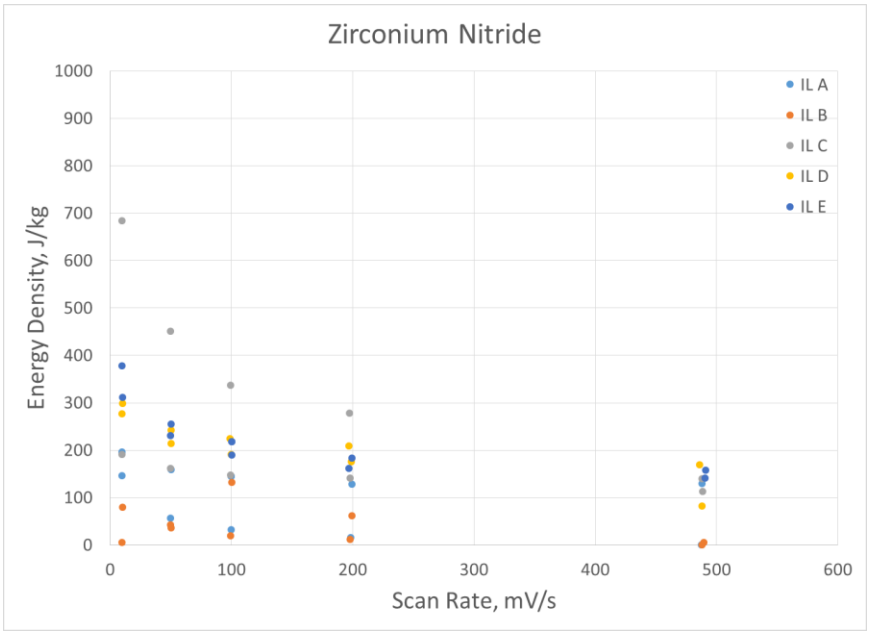

Figure 46: ZrN_x energy density versus scan rate. IL C produced the highest energy density as expected because it had the highest capacitance and a voltage window of 5.5 V – the second highest in this study.

4.5. Constant Scan Rate

Figure 47 – Figure 72 relay important information about each IL and pseudocapacitive coating combination. Through these plots, it is recognizable that plain CNT electrodes have a lower capacitance than the functionalized counterparts except where the resistance is extremely high, such as the pair of 1-Butyl-3-methylimidazolium tetrafluoroborate (IL A) and TiO_x or ZrO_x. The plain CNT electrodes also exhibited much higher stability as can be seen in the capacitance versus cycle number plots. This is to be expected since plain CNT electrodes operate entirely on the Helmholtz double layer effect which is entirely electrostatic.

Qualitatively from CV curves, oxide samples produced samples that were more resistive. This can be seen by the number of samples that produced highly linear CV curves. This suggests that the samples follow Ohm's law and are therefore performing as resistors, not capacitors. As previously discussed, resistance can be qualitatively discerned from CV curves by observing a slanted CV curve. In general, for the coatings tests, the nitride coatings produced more rectangular CV curves, even more so than the plain CNT electrodes. This observation is expected when compared to the oxide samples since nitrides, although still insulators, are much more conductive than the oxide counterparts. This observation will be further discussed in the resistance measurements section.

4.5.1. No Functionalities at Constant Scan Rate

Figure 47 – Figure 51 show the CV curves and plots of capacitance versus cycle number for the non-functionalized samples. These plots do not demonstrate significant contributions from pseudocapacitance as is expected without added functionalities. IL A

and IL E produced the highest capacitance and IL D had the lowest. However, each IL, with the exception of IL D, had a capacitance of near 5mF. The similar values are expected because the ILs all have similar dielectric constants, which is a primary metric for Helmholtz double layer capacitors. IL D, qualitatively, displays a high resistance and therefore, the capacitance is reduced due to the tilting CV curve, shown in Figure 50.

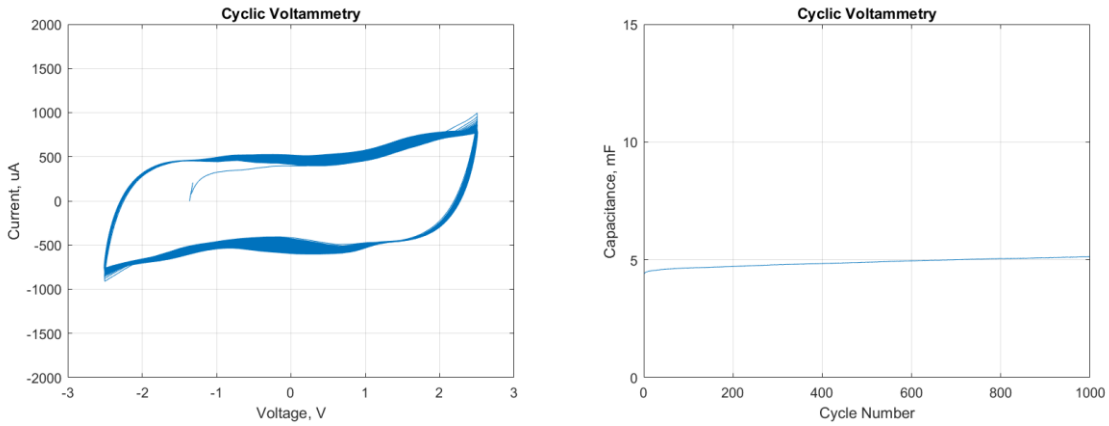

Figure 47: (left) CV and (right) capacitance versus cycle number plots for non-functionalized electrodes and IL A.

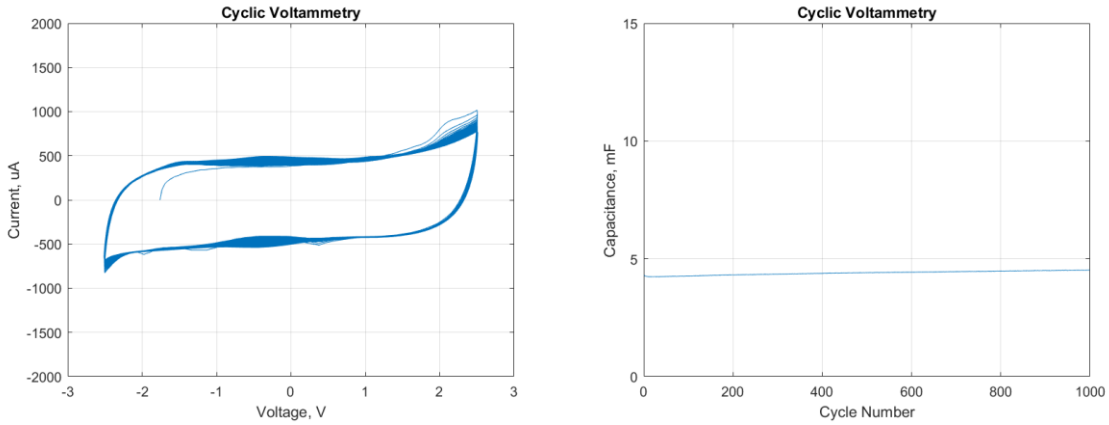

Figure 48: (left) CV and (right) capacitance versus cycle number plots for non-functionalized electrodes and IL B.

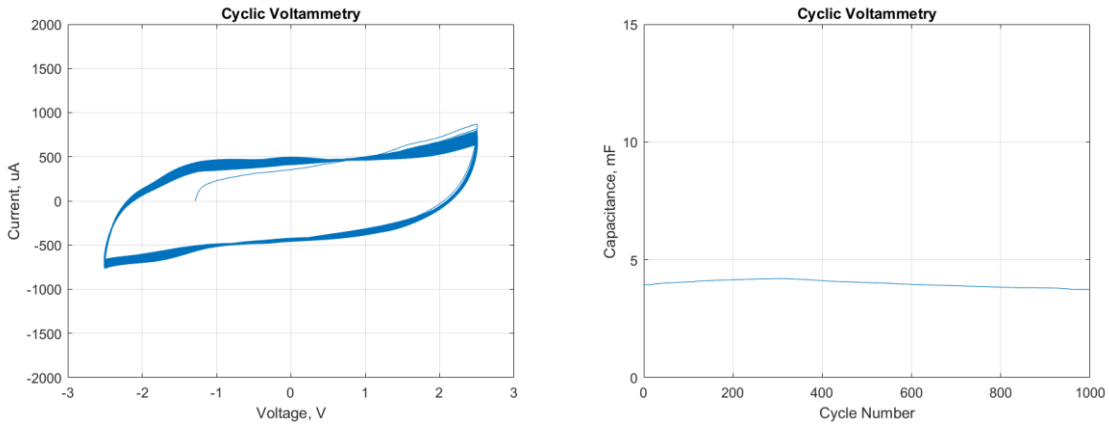

Figure 49: (left) CV and (right) capacitance versus cycle number plots for non-functionalized electrodes and IL C.

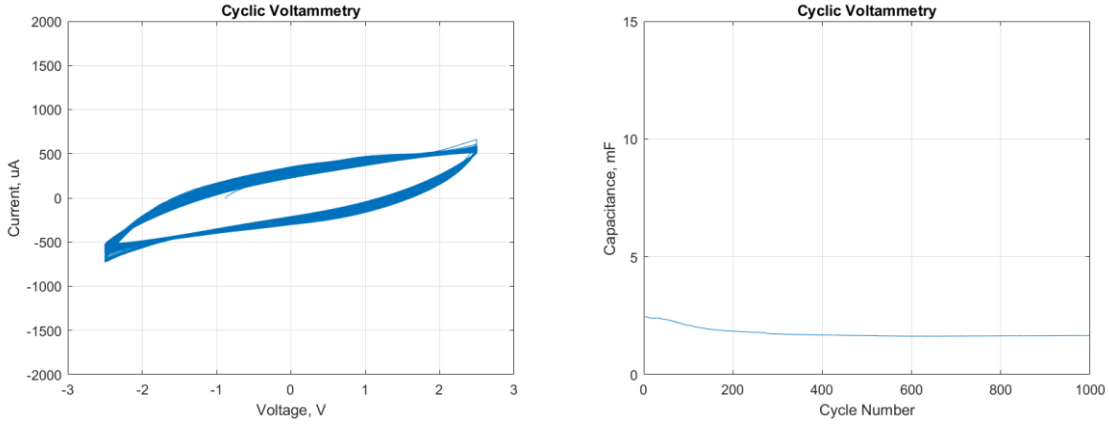

Figure 50: (left) CV and (right) capacitance versus cycle number plots for non-functionalized electrodes and IL D.

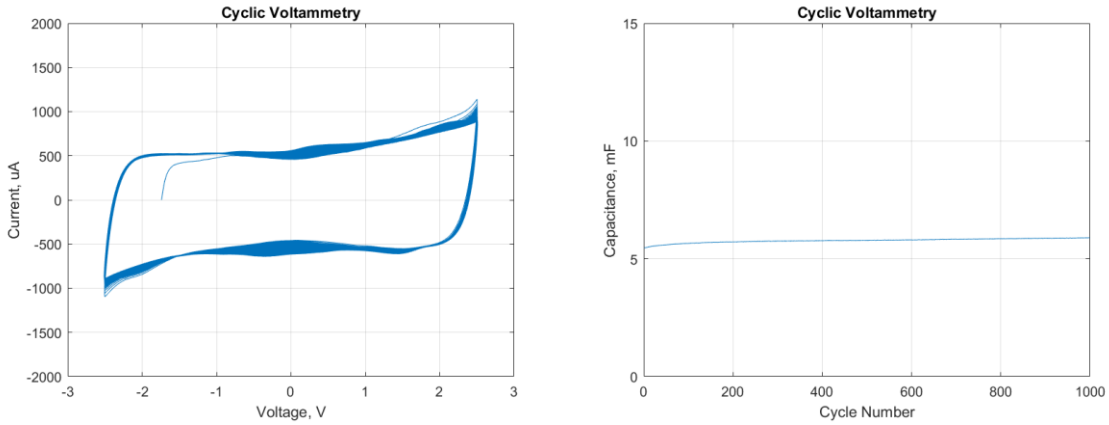

Figure 51: (left) CV and (right) capacitance versus cycle number plots for non-functionalized electrodes and IL E.

4.5.2. Titanium Oxide at Constant Scan Rate

Each TiO_x sample maintained stability over the 1,000 cycles (Figure 52 – Figure 56). IL B and IL C demonstrated pseudocapacitive interactions with the TiO_x electrode surfaces, as shown by the peaks, observed in Figure 53 and Figure 54, around +/- 1 V.

IL A, IL D, and IL E seemed to be unreactive with TiO_x. This was not expected because TiO_x has been shown to be an effective pseudocapacitive coating with a variety of electrolytes. However, IL A and TiO_x was expected to outperform most other pairs. The samples that were tested demonstrated high resistances which will reduce the area covered by the CV curve and therefore reduce the capacitance. This phenomena is discussed in detail in the next section. Although IL D and IL E did not seem to have strong electrochemical interactions, there were slight improvements in capacitance. This, combined with the high operational voltage window, still provides large energy densities comparable to batteries.

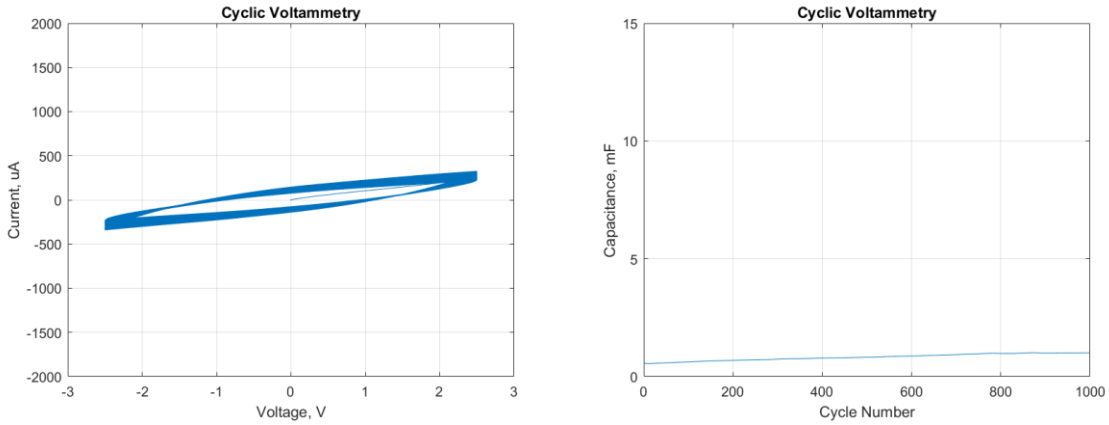

Figure 52: (left) CV and (right) capacitance versus cycle number plots for TiO_x functionalized electrodes and IL A.

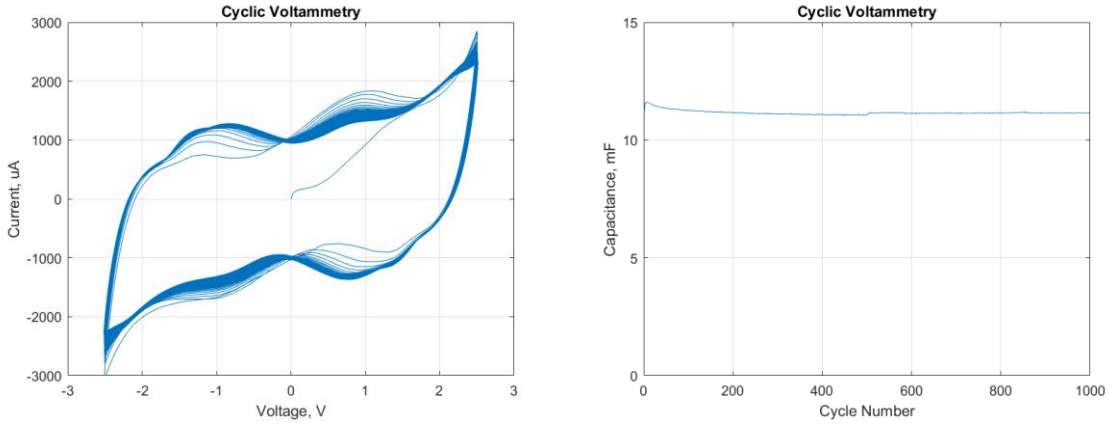

Figure 53: (left) CV and (right) capacitance versus cycle number plots for TiO_x functionalized electrodes and IL B.

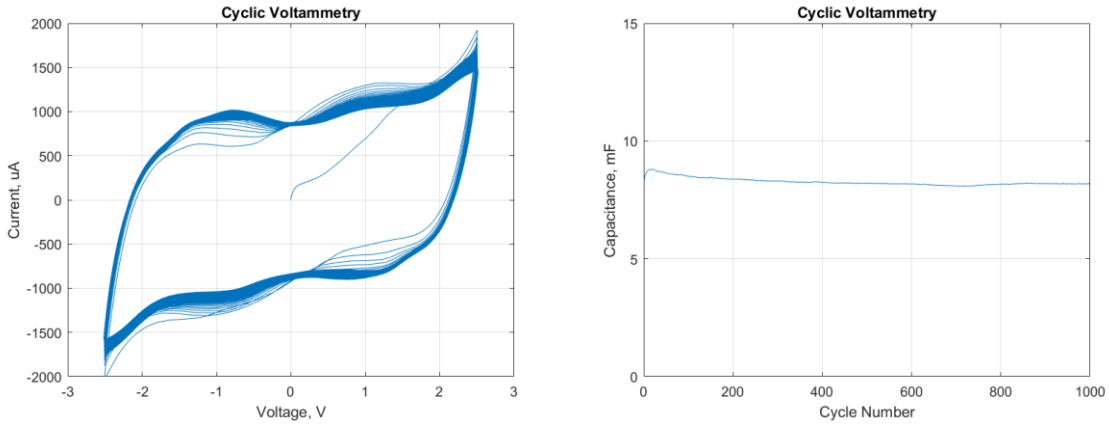

Figure 54: (left) CV and (right) capacitance versus cycle number plots for TiO_x functionalized electrodes and IL C.

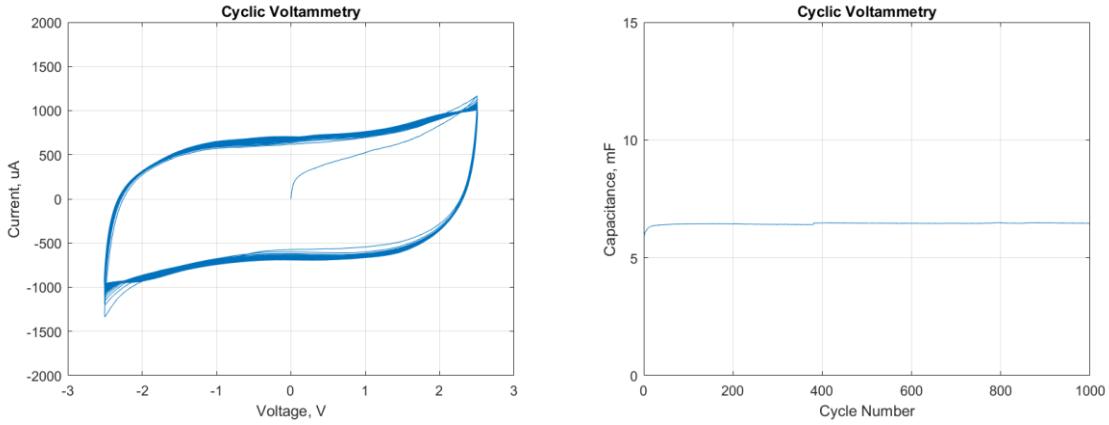

Figure 55: (left) CV and (right) capacitance versus cycle number plots for TiO_x functionalized electrodes and IL D.

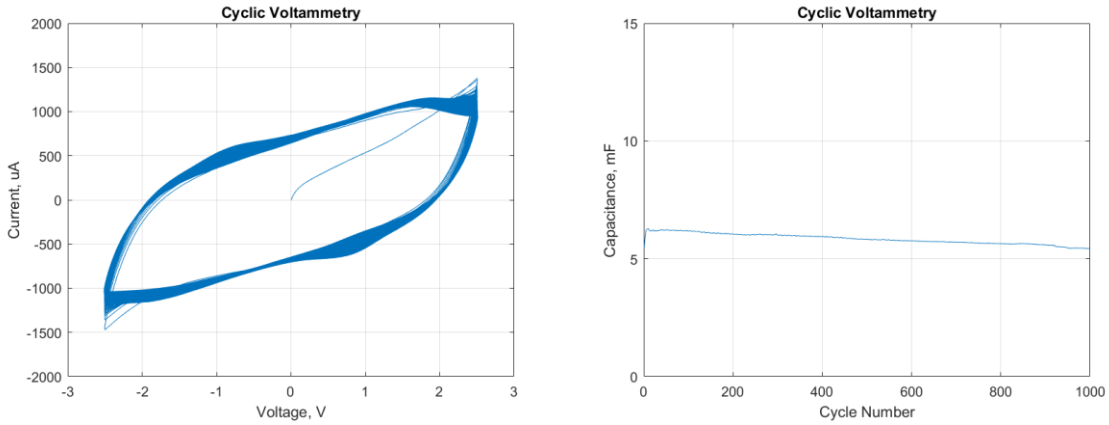

Figure 56: (left) CV and (right) capacitance versus cycle number plots for TiO_x functionalized electrodes and IL E.

4.5.3. Titanium Nitride at Constant Scan Rate

TiN_x showed highly active electrochemical interactions with every IL, however less so with IL E, as observed in Figure 57 – Figure 62. In the most electrochemically active cases, there were dramatic increases in capacitance over the 1,000 cycles. It is uncertain as to whether this is a conditioning effect for the coating or if there is degradation of the electrode/electrolyte during the reactions. However, degradation is unlikely because further testing did not show signs of malfunction.

IL A exhibited three electrochemical peaks in the CV curve (Figure 57). However, these peaks are at unusual locations. IL B, IL C, and IL D (Figure 58 – Figure 60) only demonstrated two peaks with one peak in each case forming near the +/- 1V that was shown in the TiO_x samples. Similar peaks are expected in the TiN_x samples because charge storage from TiN_x occurs via the same mechanism as TiO_x but utilizes and oxides formed on the surface of the TiN_x coating [65].

Interestingly, IL A and IL D had strong interactions with TiN_x but did not shown any significant signs of electrochemical interaction with TiO_x. There are two possible explanations for the difference in electrochemical activity – (1) the difference in bonding of titanium/oxygen and titanium/nitrogen is such that it allows a more favorable pseudocapacitive interaction when using titanium/nitrogen, or (2) the small amounts of TiO_x contamination in the TiN_x samples could be dominating the reaction. The second point suggests that a smaller amount of TiO_x may need to be used to produce significant pseudocapacitance in the TiO_x samples. In the case of IL A, the TiO_x sample suffered from high resistances and therefore may not have been able to respond to the applied voltage appropriately. As previously mentioned, IL A and TiO_x has been previously demonstrated to exhibit pseudocapacitance [31].

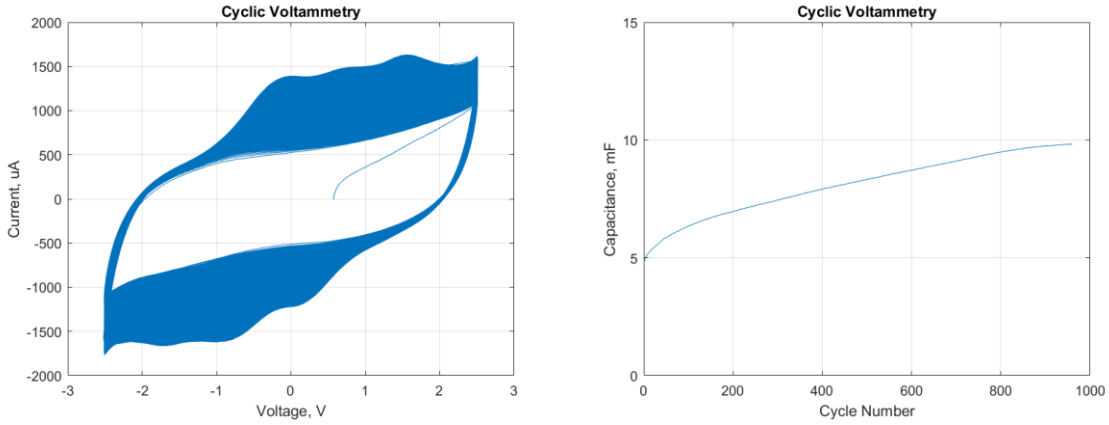

Figure 57: (left) CV and (right) capacitance versus cycle number plots for TiN_x functionalized electrodes and IL A.

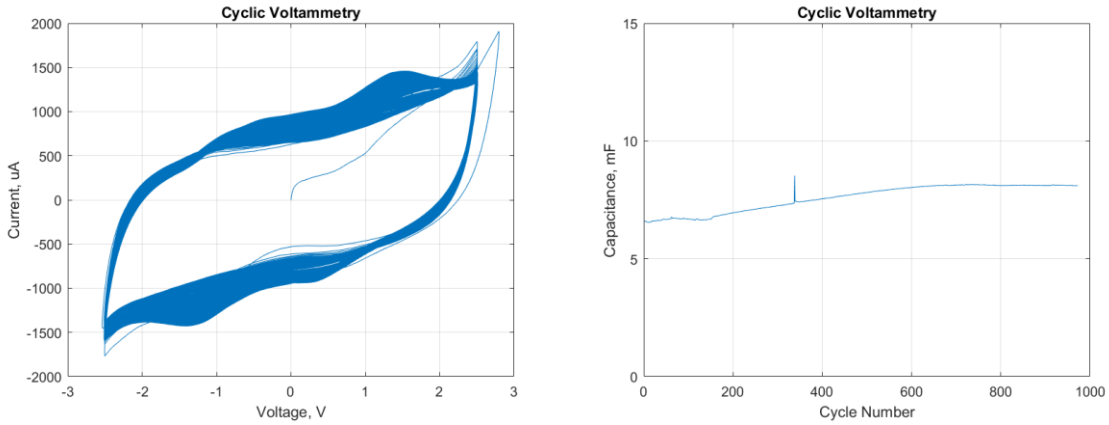

Figure 58: (left) CV and (right) capacitance versus cycle number plots for TiN_x functionalized electrodes and IL B.

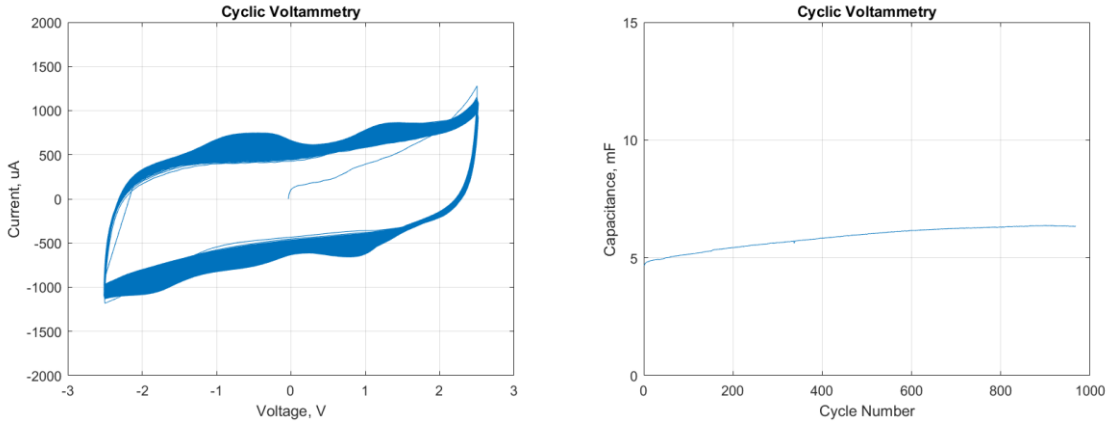

Figure 59: (left) CV and (right) capacitance versus cycle number plots for TiN_x functionalized electrodes and IL C.

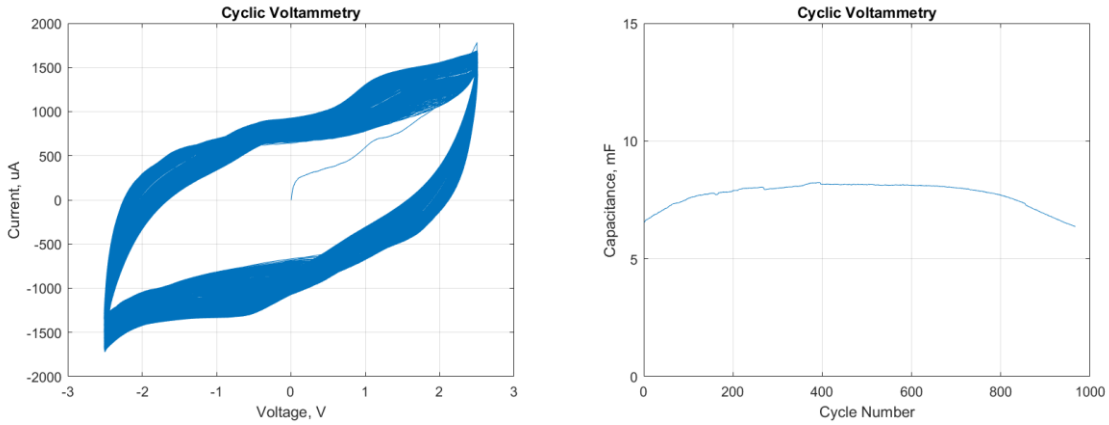

Figure 60: (left) CV and (right) capacitance versus cycle number plots for TiN_x functionalized electrodes and IL D.

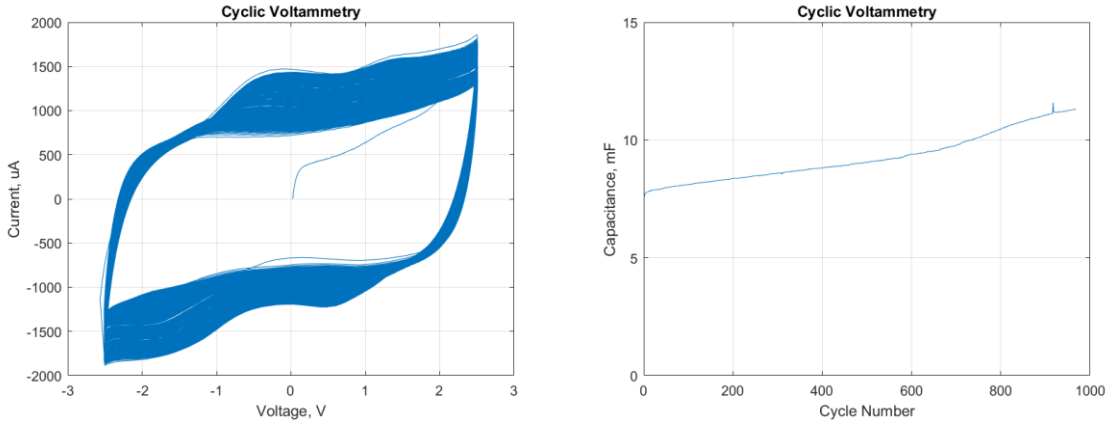

Figure 61: (left) CV and (right) capacitance versus cycle number plots for TiN_x functionalized electrodes and IL D.

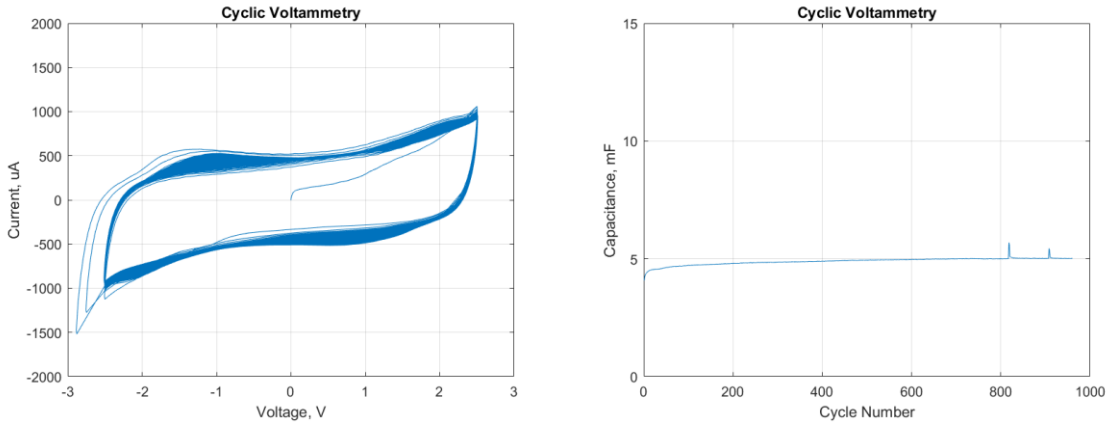

Figure 62: (left) CV and (right) capacitance versus cycle number plots for TiN_x functionalized electrodes and IL E.

4.5.4. Zirconium Oxide at Constant Scan Rate

Zirconium oxide samples were particularly unreactive as shown in Figure 63 – Figure 67. IL A and IL E produced highly resistive samples (Figure 63 and Figure 67). IL C did not show any signs of electrochemical interactions, as seen in Figure 65, and produced CV curves very similar to the plain CNT/IL C sample. IL B (Figure 64) produced small peaks in the CV curve and it is difficult to say if these are electrochemical interactions or effects from overcharging the IL. However, similar, yet less defined, peaks were shown in the plain CNT samples which therefore suggests that no strong pseudocapacitve interaction is occurring. The final sample, IL D, did show strong pseudocapacitive peaks, however these peaks were more prominent on charging compared to discharging (Figure 66). This is unusual since most supercapacitors produce symmetric CV curves unless an anisotropic architecture is used (ie. positive electrode is coated with TiO_x and negative

electrode is coated with ZrN_x). This might suggest that the cathodic and anodic ions from the IL are interacting differently with the electrodes.

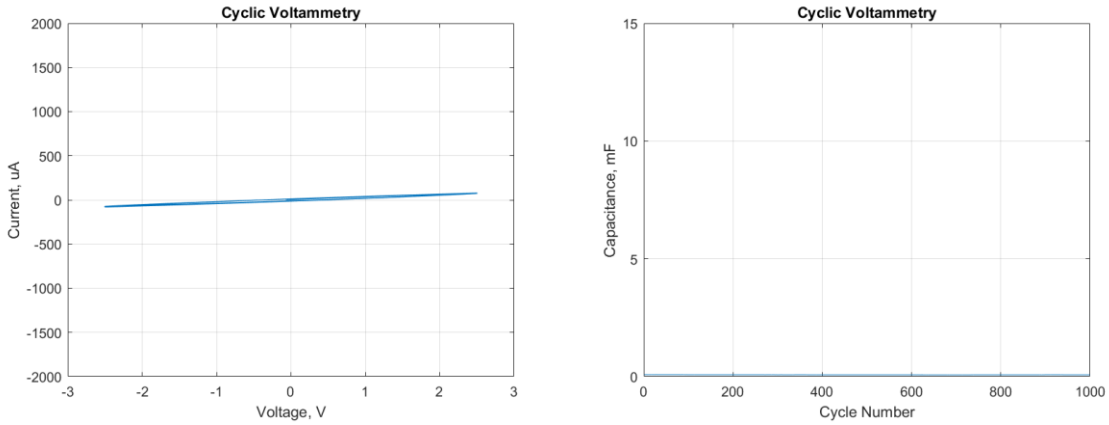

Figure 63: (left) CV and (right) capacitance versus cycle number plots for ZrO_x functionalized electrodes and IL A.

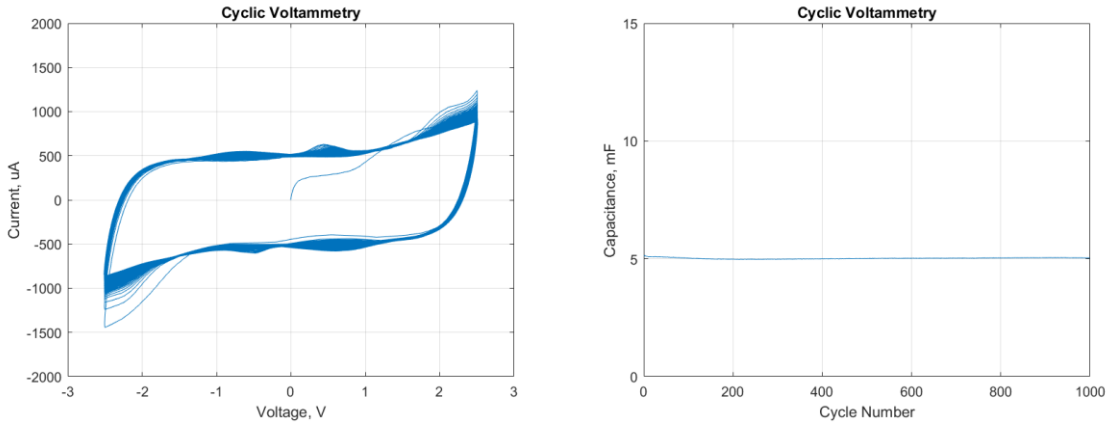

Figure 64: (left) CV and (right) capacitance versus cycle number plots for ZrO_x functionalized electrodes and IL B.

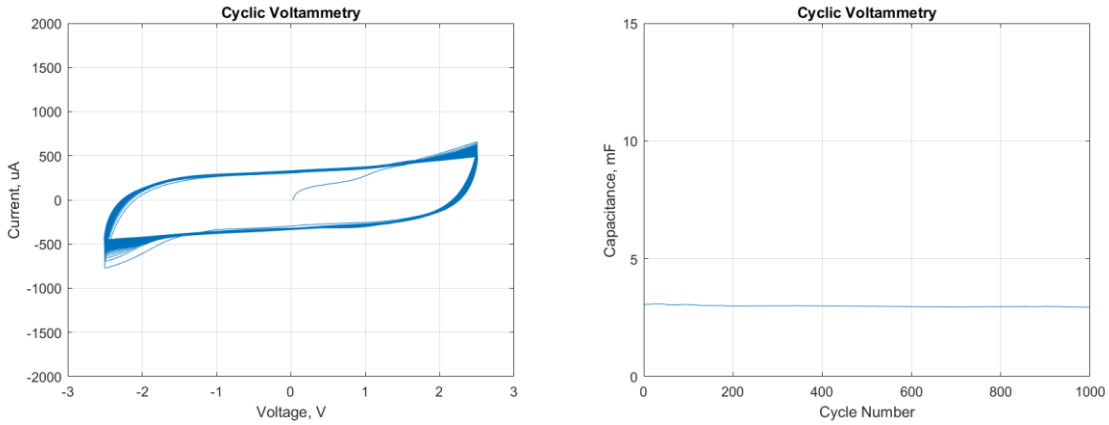

Figure 65: (left) CV and (right) capacitance versus cycle number plots for ZrO_x functionalized electrodes and IL C.

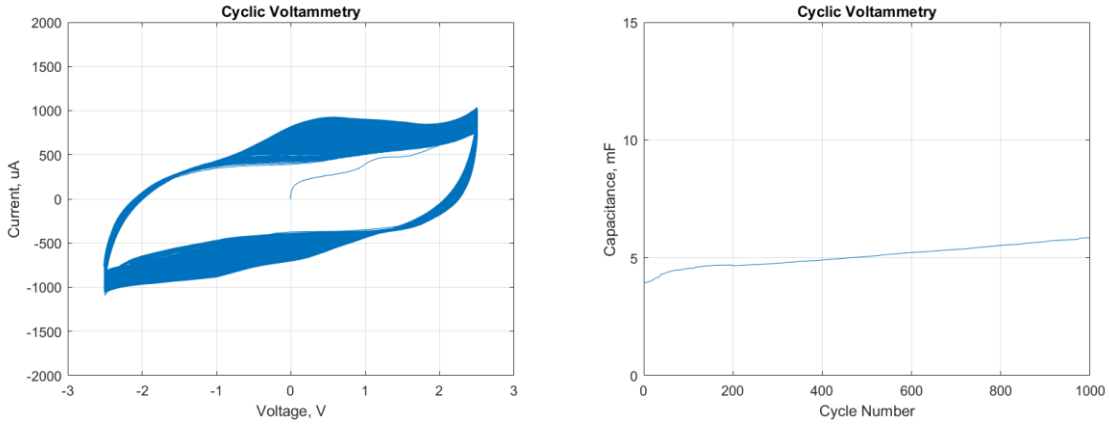

Figure 66: (left) CV and (right) capacitance versus cycle number plots for ZrO_x functionalized electrodes and IL D.

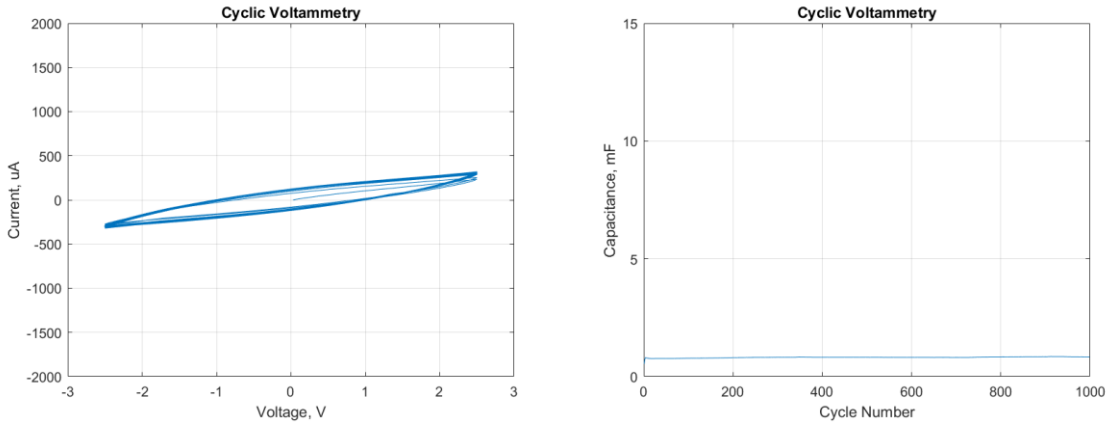

Figure 67: (left) CV and (right) capacitance versus cycle number plots for ZrO_x functionalized electrodes and IL E.

4.5.5. Zirconium Nitride at Constant Scan Rate

Zirconium nitride samples, similar to the ZrO_x samples, were less pseudocapacitively active than the titanium samples. IL B and IL C produced pseudocapacitive reactions but were unstable, as shown in Figure 69 and Figure 70. IL A, IL D, and IL E remained highly stable over the 1,000 cycle test but did not demonstrate any significant pseudocapacitve reaction (Figure 68, Figure 71 and Figure 72). These samples showed similar capacitance values as the non-functionalized electrodes which confirms there lack of pseudocapacitance. Further studies need to be conducted to confirm charge storage mechanisms, particularly with IL C, which exhibited significant pseudocapacitance and therefore high capacitance.

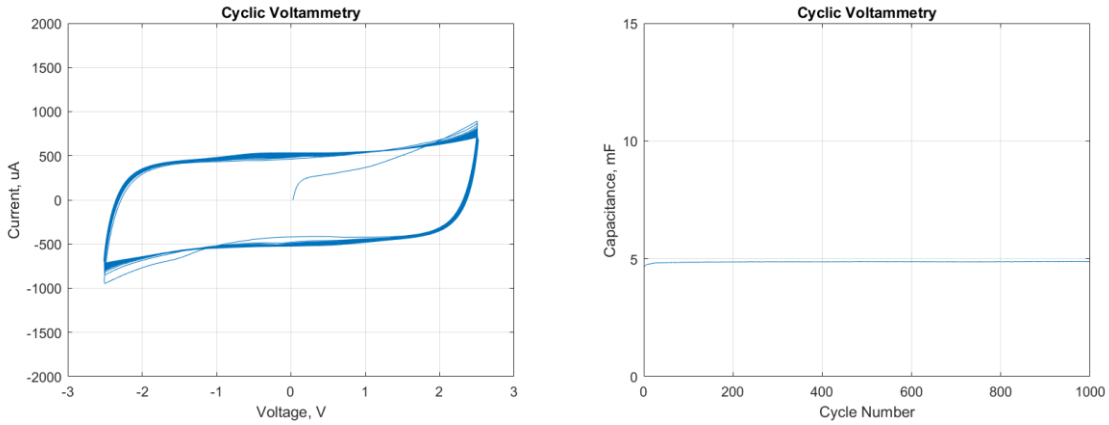

Figure 68: (left) CV and (right) capacitance versus cycle number plots for ZrN_x functionalized electrodes and IL A.

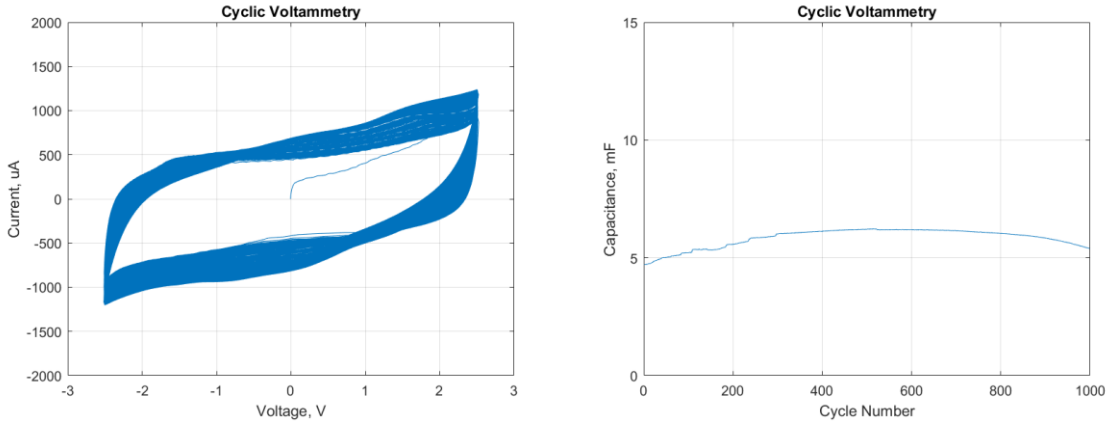

Figure 69: (left) CV and (right) capacitance versus cycle number plots for ZrN_x functionalized electrodes and IL B.

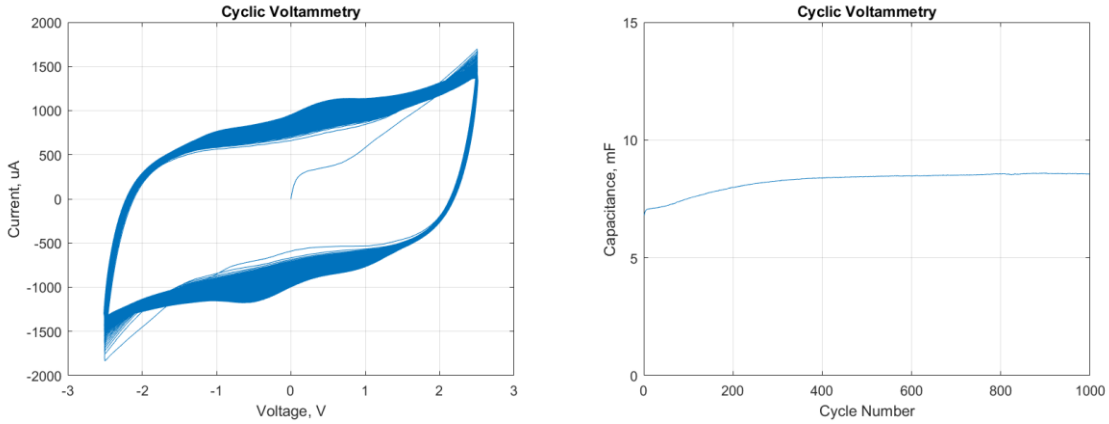

Figure 70: (left) CV and (right) capacitance versus cycle number plots for ZrN_x functionalized electrodes and IL C.

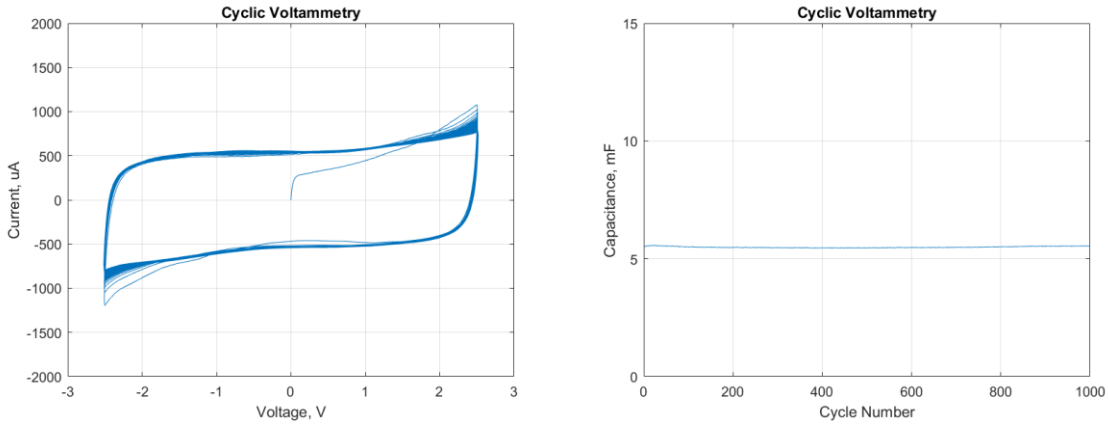

Figure 71: (left) CV and (right) capacitance versus cycle number plots for ZrN_x functionalized electrodes and IL D.

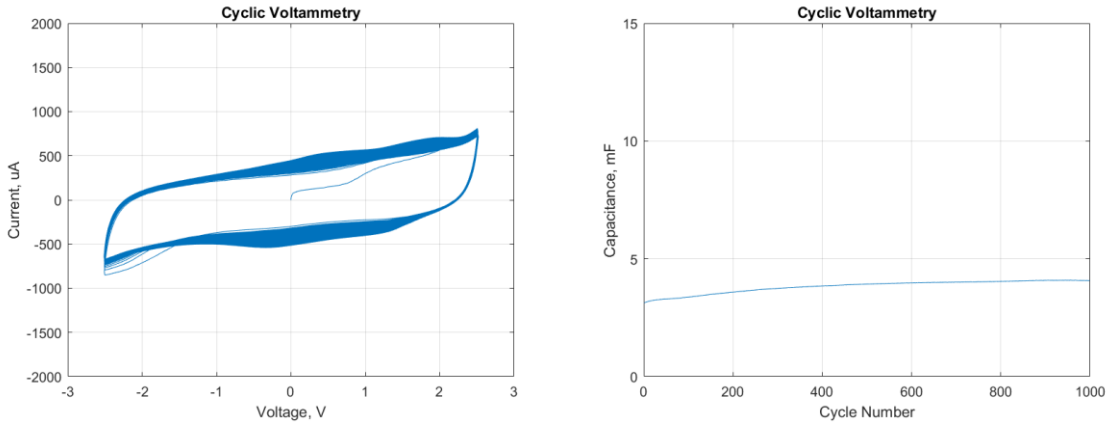

Figure 72: (left) CV and (right) capacitance versus cycle number plots for ZrN_x functionalized electrodes and IL E.

4.6. Resistance measurements

ESR is an important metric in energy storage devices and can be calculated using CD testing and Ohm's law. An alternative method, impedance spectroscopy can also be used. In this work, galvanostatic methods were used initially, but an undefined voltage drop created uncertainty in the data. To ensure the data was accurate, impedance spectroscopy was implemented to verify the results.

4.6.1. Galvanostatic Method

Measurements of equivalent series resistance (ESR) were conducted using galvanostatic methods at currents of 200, 350, 500, 650, and 800 µA in the voltage range of -2.5 to 2.5 V. Each measurement was made on a single cycle. As shown in Figure 73 there is significant non-linearity in the discharge curve due to pseudocapacitance [66].

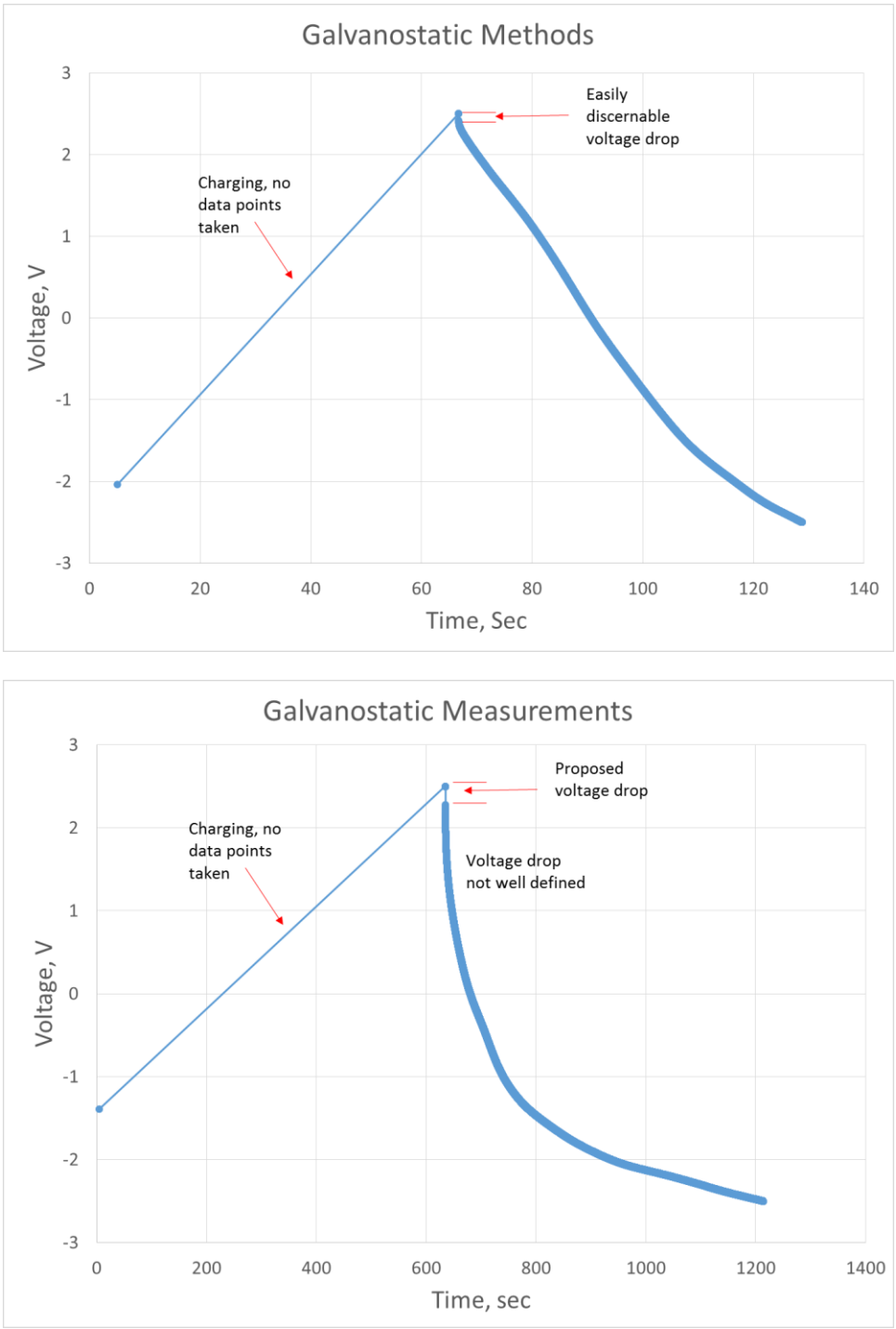

Figure 73: (left) Galvanostatic test of non-functionalized CNT capacitor demonstrating an easily discernable voltage drop. (right) Galvanostatic measurement of TiN_x demonstrating significant non-linearity upon discharge and therefore difficulty in establishing a clear voltage drop.

The non-linearity prevented the formation of a distinguishing voltage drop that is traditionally present in supercapacitors. To overcome these limitations, the voltage drop was defined as the first data point after discharging. A sample calculation of ESR from acquired data is shown Figure 74 below:

Current(A)	Voltage(V)
0	-1.64283919
0.000649945	2.50025773
0.000649945	2.500907421
0.000649945	2.500907421
0.000649945	2.500907421
0.000649945	2.500907421
0.000649945	2.500907421
-8.9472E-05	2.31541276
-0.00014518	2.298682451
-0.00019583	2.282764196
-0.00024107	2.267983198
-0.00028159	2.254176617
-0.00031839	2.241019726
-0.00031839	2.241019726
-0.00035148	2.228675127

$$\Delta V = IR$$

$$From\ data: \Delta V = 2.500907421 - 2.31541276 = 0.18548982\ V$$

$$I = 350 * 10^{-6}\ A$$

$$R = 530.0\ \Omega$$

Figure 74: Sample data for galvanostatic calculations of total ESR.

As can be easily observed from the data, there is a 10 fold difference in slope between the first two points upon discharge (highlighted in Figure 74) and the next pair of data points. Due to this significant difference in slope, the method described above is justified for determining resistance of the supercapacitors. However, impedance spectroscopy was also used to verify these results as discussed in the next section.

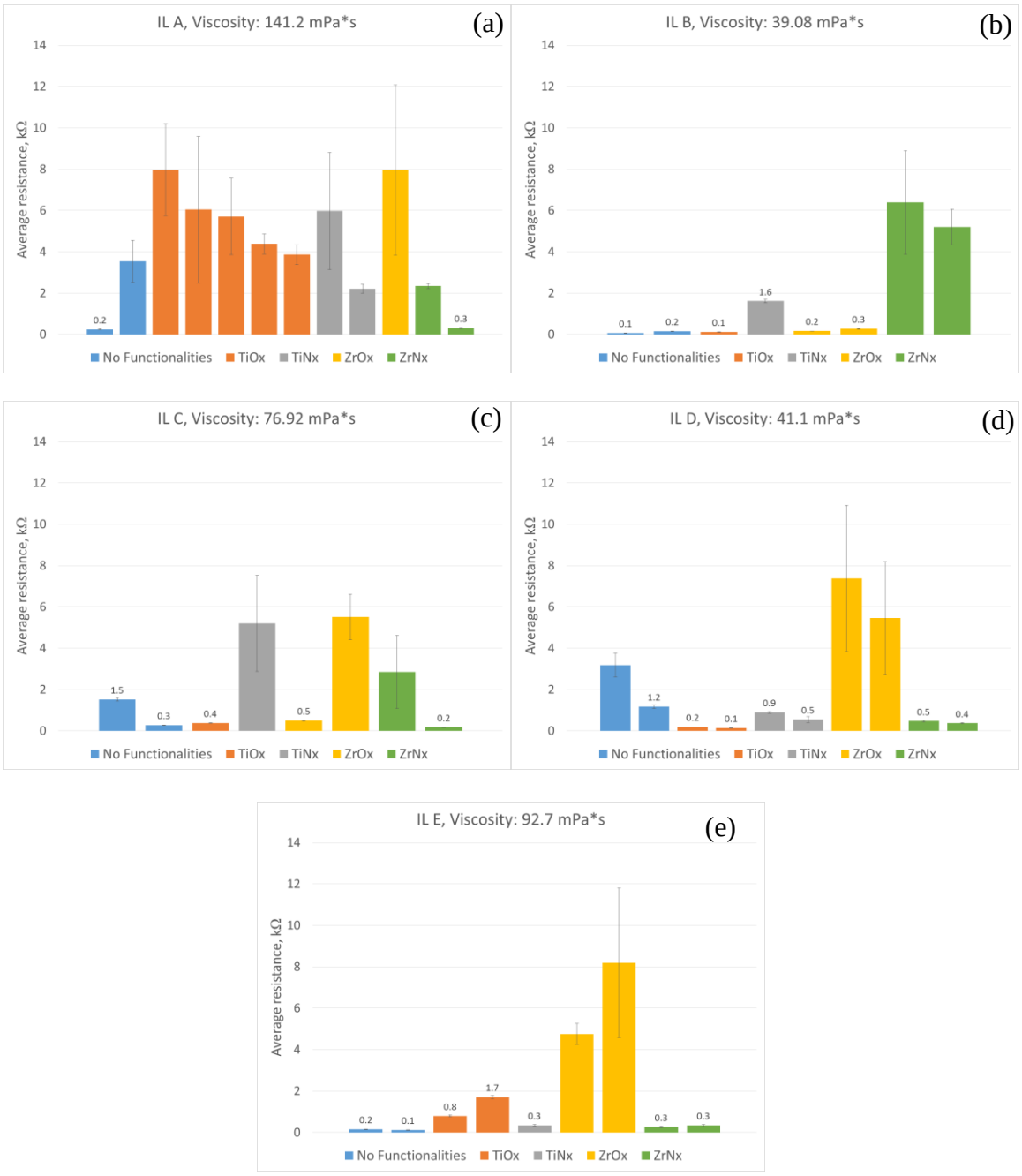

Figure 75: Resistance measurements compared to IL.

Figure 75 shows the resistance, calculated through galvanostatic methods, for each pseudocapacitive coating, grouped by IL. Each bar is an average of the calculated resistances at each tested current. Of particular note from this data set, IL A exhibited

extremely high resistances compared to the other ILs. Fisher et al. reports resistances with IL A, and a similar electrode architecture, on the order of ohms, whereas this data suggests resistances in kilo-ohm ranges [31]. Although this work contradicts Fisher's results, the consistently high resistance suggests IL A may not produce pseudocapacitive reactions with the studied coatings. However, an alternative explanation can be drawn due to the viscosity of IL A.

The resistance was much lower in samples that were filled entirely with some samples below 100Ω. However, these resistances still result in a power density that is much too high for most supercapacitor applications. For example, the sample with the lowest resistance (67.5 Ω) would result in a power density of 442.2 J/kg. As shown in Figure 1, this value puts the as fabricated samples in a similar category as batteries.

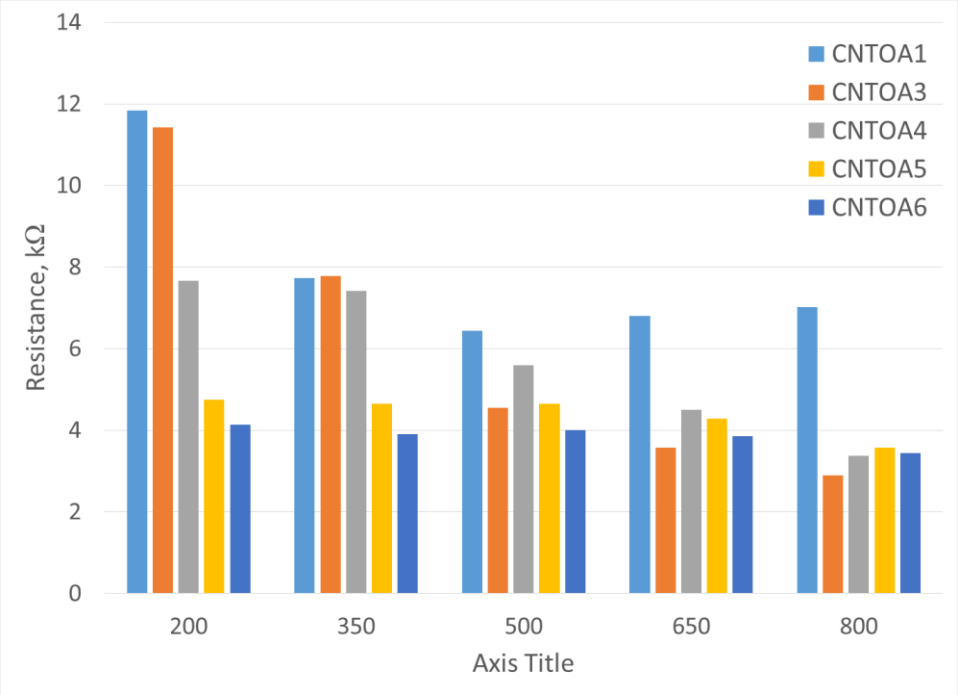

Figure 76: Resistance measurements made for samples comprised of TiO_x pseudocapacitive coating and IL A. The large changes in resistance demonstrate a possible heating mechanism from insufficient amounts of electrolyte.

4.6.2. Effects of Viscosity

Viscosity is considered one of the most important parameters to consider when choosing ILs for practical applications [67]. When designing supercapacitors, the viscosity should be considered because it has a tremendous effect on the ionic mass transport [68].

IL A has a viscosity of 141mPa·s which is 50mPa·s higher than the next highest viscosity IL, IL E. The high viscosity makes the filling method previously described particularly difficult because the viscous liquid does not flow easily through the fill ports. This suggests that the supercapacitors are not being filled to entirety. Without being filled entirely, the electrolyte is expected to form a thin pathway on the walls of the electrodes. This layer allows charge transfer, but due to the size of the pathway, ionic motion is likely

inhibited, which would increase resistance. This is supported through the resistance calculations at different currents as shown in Figure 75. The highest resistance occurs at low currents. However, as the current is increased, heat is generated in the small, resistive pathways. As the IL is heated ionic mobility increases and reduces the resistance. This can also be observed in Figure 75 where the higher resistance samples generally have larger error bars from the resistance changing dramatically at each tested current since each value is an average of all tested currents. Further design development is expected to reduce the resistance.

It is useful to analyse the resistance versus achieved viscosity for the studied ILs. These results are presented in Figure 77 –Figure 81. The resistance presented in these figures is calculated from galvanostatic methods and the error bars are a single standard deviation from the average of each current tested.

No correlation between viscosity and resistance was observed for the plain CNT electrodes, as shown in Figure 77. This was unexpected as there is a dramatic correlation between viscosity and ionic mobility and therefore resistance [68]. The expected trend is shown in the TiO_x samples (Figure 78) where resistance increased with viscosity of the IL. However, no other system exhibited a significant correlation of viscosity and resistance (Figure 79 – Figure 81). There are two conclusions that can be drawn from this data. First, viscosity is less important than previously thought. Second, as previously discussed, the supercapacitors were not being filled to entirety and caused deviations in resistance. Most likely, the supercapacitors in this work were not consistently being filled to entirety.

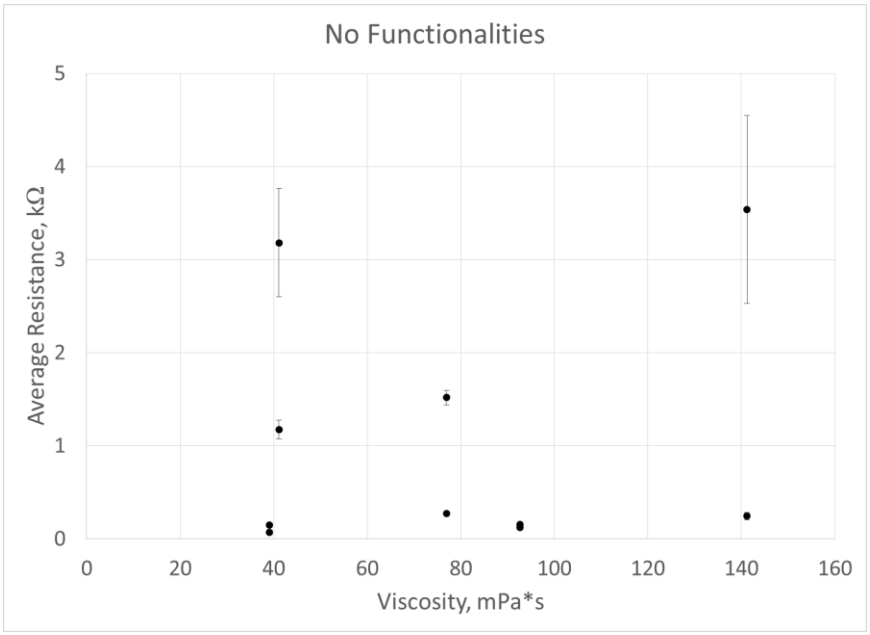

Figure 77: Viscosity effects in CNT electrodes. No strong correlation is observed.

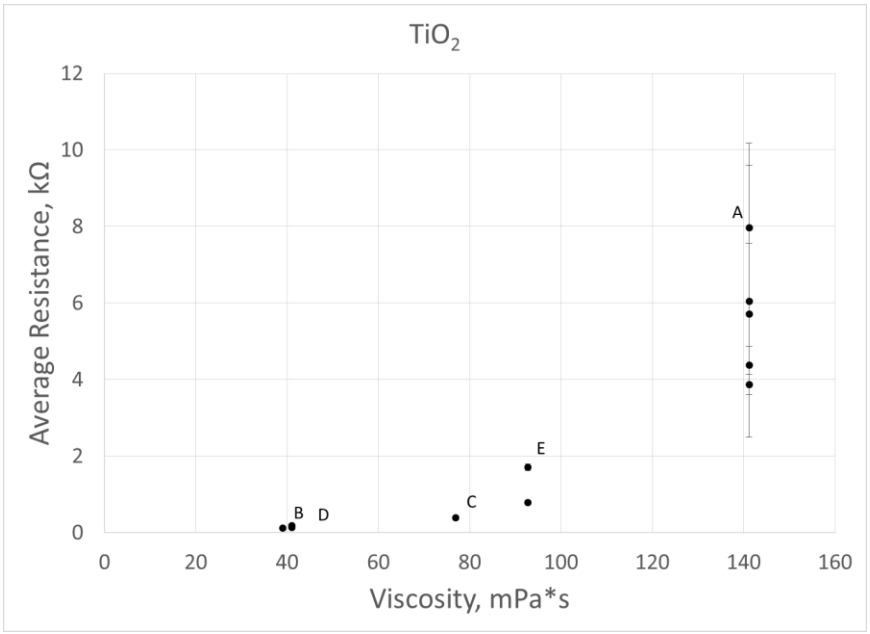

Figure 78: Viscosity effects in TiO_x coated CNT electrodes. A strong correlation is observed with increasing resistance occurring with higher viscosities.

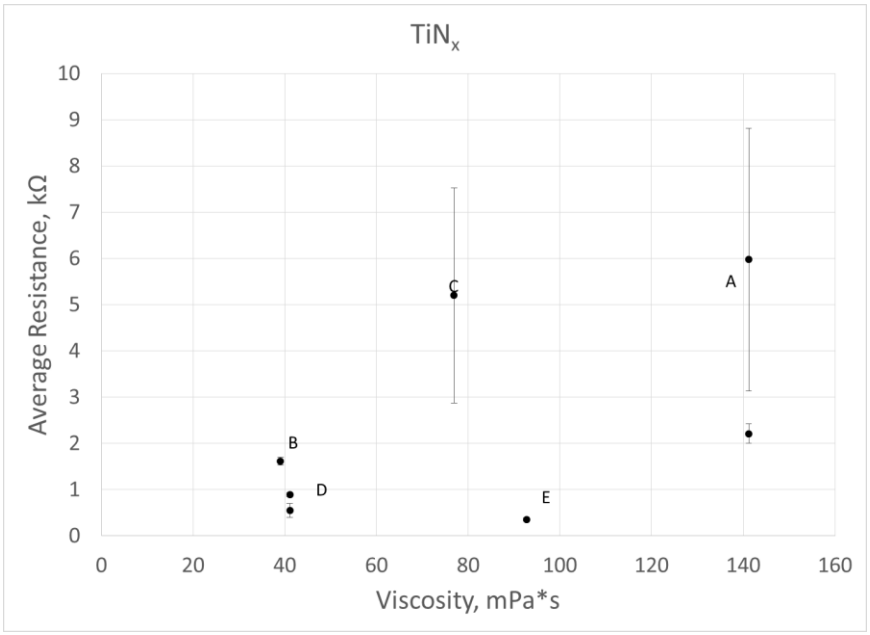

Figure 79: Viscosity effects in TiN_x coated CNT electrodes. No strong correlation is observed.

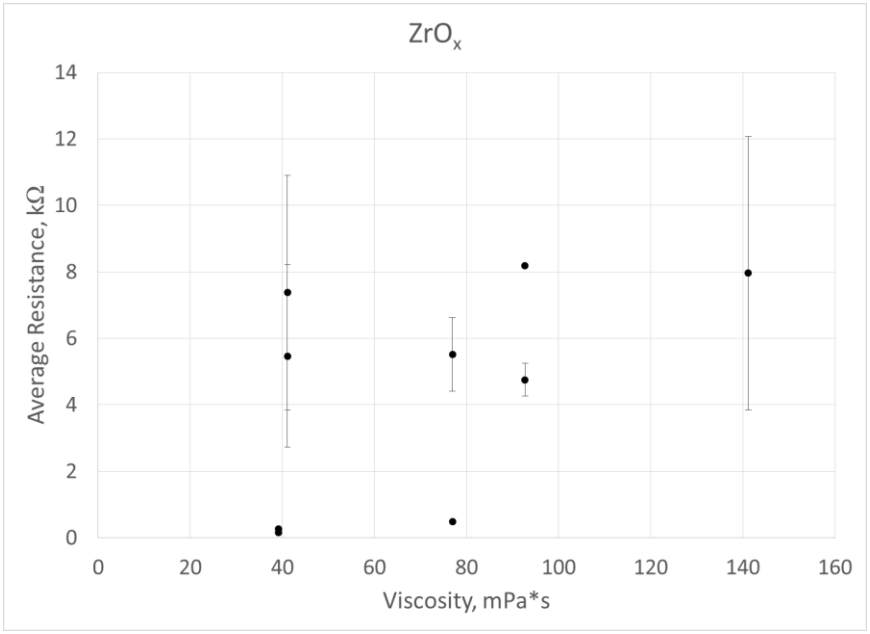

Figure 80: Viscosity effects in ZrO_x coated CNT electrodes. No strong correlation is observed.

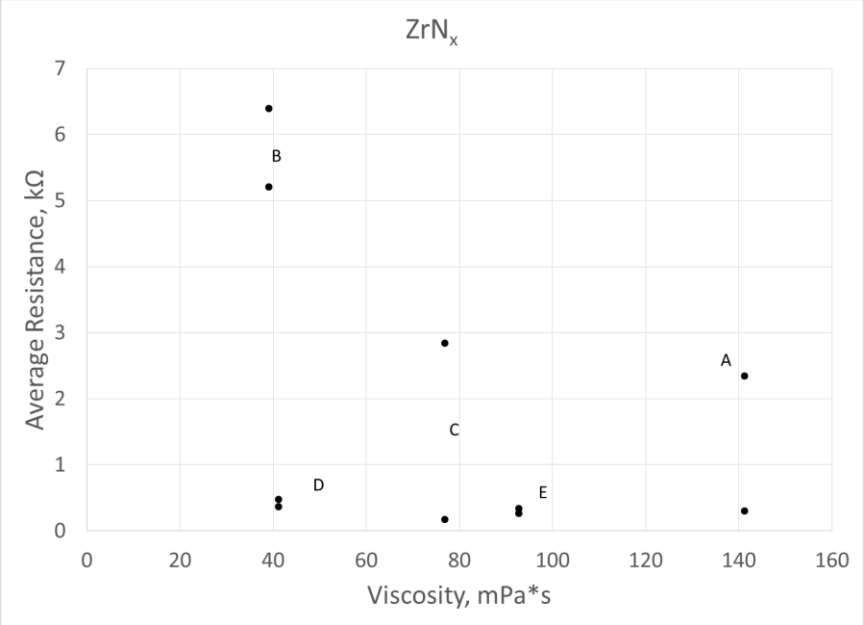

Figure 81: Viscosity effects in ZrN_x coated CNT electrodes. No strong correlation is observed.

4.6.3. Impedance Spectroscopy

For the impedance spectroscopy measurements, a 100mV alternating voltage was applied to a supercapacitor over a frequency from 1 hz to 1 Mhz on a Solartron impedance analyzer. The acquired data was fit to the equivalent circuit model shown in Figure 82 using the fitting software provided with the Solartron. The equivalent circuit model is a modified Randles circuit model, a common circuit model for electrochemical impedance spectroscopy [27], with two resistors and two constant phase elements (CPE). The extra CPE was added to account for an electrochemical reaction on each electrode. This data is used as a confirmation of resistances measured through galvanostatic methods. These tests are not perfectly comparable because the equivalent circuit model breaks the total

resistance, measured by galvanostatic methods, into two resistances, R1 and R2. Since there is no theoretical method to add these resistors and obtain a 'total resistance,' it is assumed that the total resistance is low if both resistors have resistance below 1kΩ. However, the resistance is assumed to be high if one or more resistors have resistance above 1 kΩ. The fitted data is presented in Figure 83 – Figure 87.

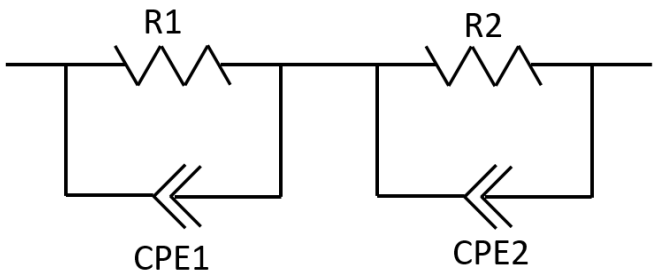

Figure 82: Equivalent circuit model for electrochemical reaction. Modified Randles circuit model with extra constant phase element.

Plain CNT supercapacitors were fabricated and tested as a baseline measurement to compare the pseudocapacitive samples. Fisher et al. tested similar supercapacitor architectures and demonstrated resistances on the order of a few Ω [31]. IL B and IL E exhibited the lowest resistances. IL A and IL D exhibited high resistances in the kΩ range. This suggests that the supercapacitor was not filled entirely.

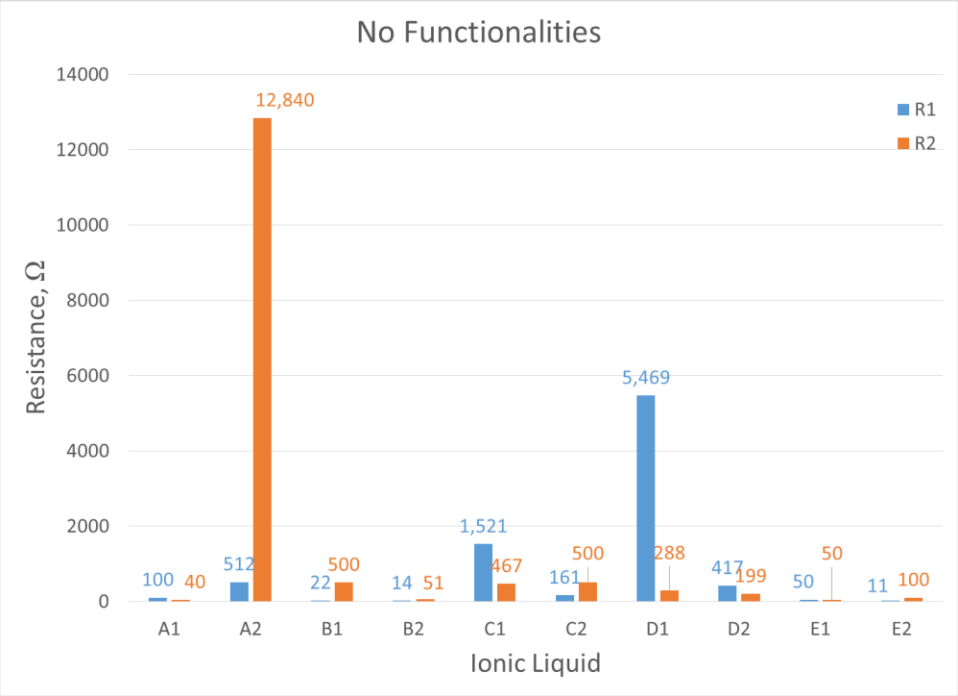

Figure 83: Resistance of plain CNT samples measured by impedance spectroscopy. Most samples exhibited high resistances for supercapacitor applications, however, these results confirm the calculations from galvanostatic methods. IL B and IL demonstrated the lowest resistances.

The resistance of the TiO_x samples are shown in Figure 84. IL A exhibited particularly high resistances with all samples having at least one resistor in the kΩ range. This confirms the results from the galvanostatic methods. The consistently high resistance of IL A in the TiO_x samples was unexpected as Fisher et al. reported resistances on the order of a few Ω [31] for a similar system. There are two differences between the work reported by Fisher and the present work. First, the titania reported by Fisher had been annealed at 600°C in N_2 for 4 hours after deposition resulting in phase changes in the titania. Second, the electrolyte used in Fisher's work was a mixture of IL A and acetonitrile. The addition of acetonitrile would have a dramatic effect on the resistance since the

conductivity of acetonitrile is orders of magnitude smaller than that of any ILs studied in this work. The viscosity and ionic mobility are also significantly improved which reduces the resistance. IL D also had one resistor in the kΩ range. However, the inconsistency between IL D samples suggests that this may have been due to fabrication errors. In comparison, IL B, IL C, and IL E had low resistances with the TiO_x coating, however the resistances are still not low enough for high power supercapacitor applications which requires resistances on the order of a few Ω. Further investigation needs to be completed to produce high power TiO_x supercapacitors utilizing the presented architecture. IL B and IL C produced the lowest resistances.

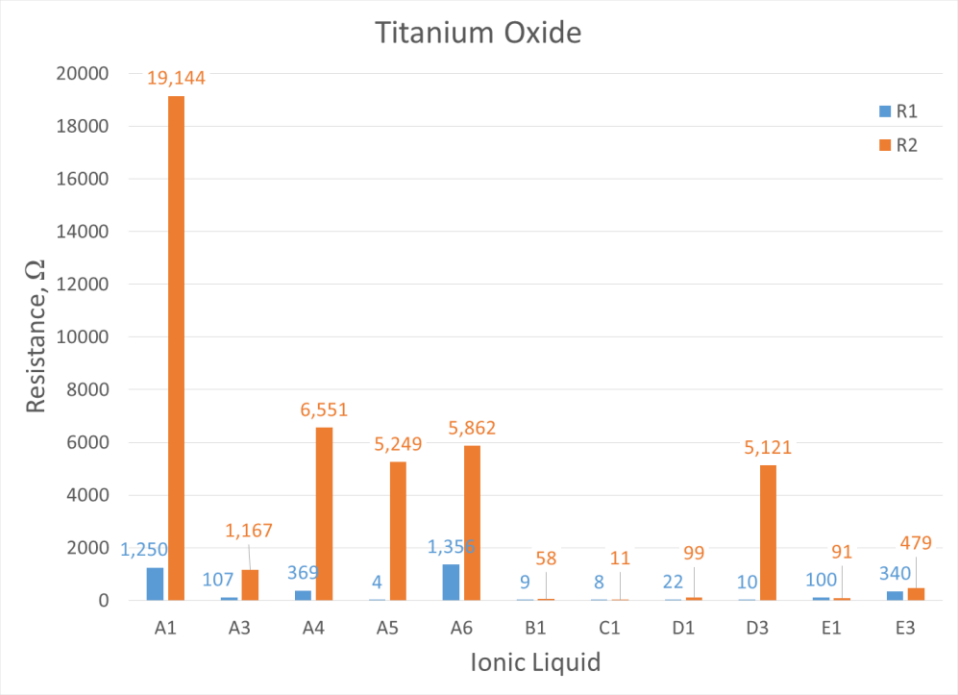

Figure 84: Resistance of TiO_x samples measured by impedance spectroscopy. Each of the IL A samples exhibited extremely high resistances. It is unclear whether this is due to chemical interactions or manufacturing error due to the high viscosity of the IL. IL B and IL C produced the lowest resistances.

The TiN_x samples exhibited similar properties as the TiO_x samples as shown in Figure 85. IL A, IL B, and IL C exhibited resistances in the kΩ range. Charge storage in TiN is accomplished through oxygen vacancies on the TiO_x layer formed from atmosphere [65]. Therefore, high resistances in the TiN_x samples for IL A are supported by the high resistances in the TiO_x samples. Due to processing time, a limited number of TiN_x samples were able to be fabricated and only single samples of IL B, IL C and IL E were fabricated. IL D showed low resistance across two samples which suggests that IL D would be the best pair with TiN_x samples, however IL E exhibited even lower resistance. Each of these results correlates with observations from galvanostatic methods. Further studies need to be conducted to verify the presented results.

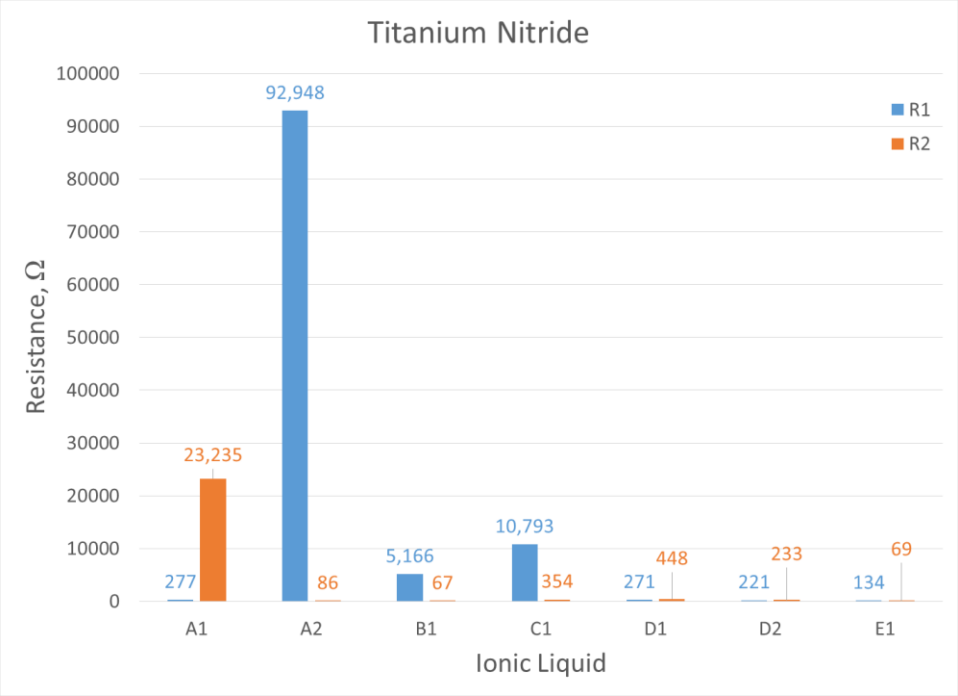

Figure 85: Resistance of TiN_x samples measured by impedance spectroscopy. IL A produced high resistances whereas IL D and E produced the lowest resistances with TiN_x.

ZrO_x produced high resistances with each IL except IL B and one sample of IL C as shown in Figure 86. Again, IL A resulted in tremendously high resistances with both samples tested having at least one resistance over 10 kΩ. These measurements correlate well with the galvanostatic methods which also demonstrated low resistances for IL B only.

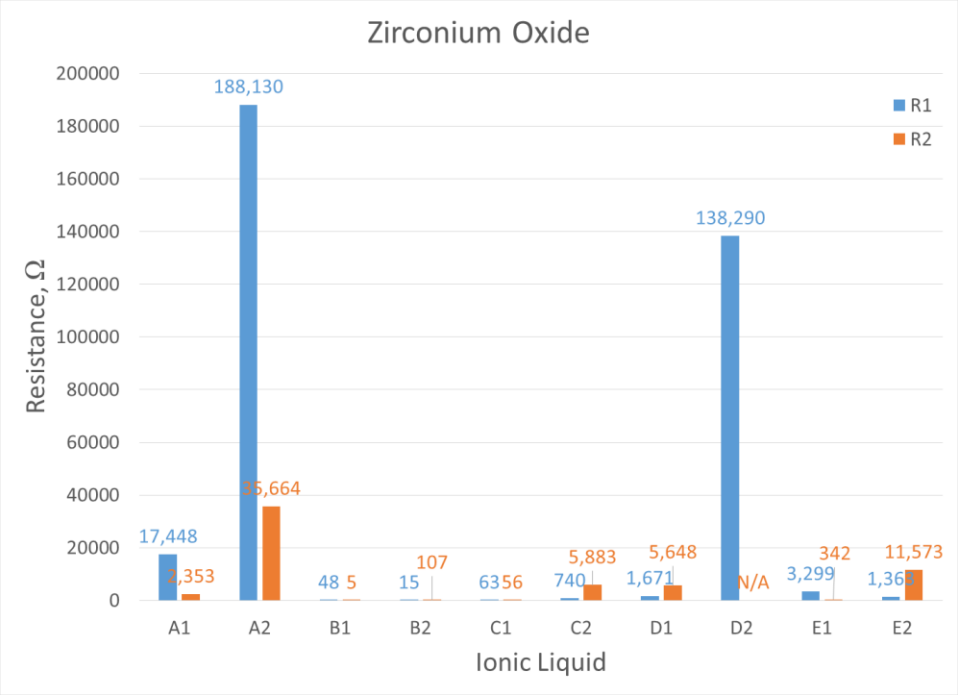

Figure 86: Resistance of ZrO_x samples measured by impedance spectroscopy. IL A and D had high resistances whereas IL B had low resistance. N/A for IL D2 shows that the value had no effect on the fitting of the impedance data.

Zirconium nitride had the most consistently low resistance samples as shown in Figure 87. However, a single sample of each IL A and IL B still exhibited high resistances. Else, each of the ILs had at least one sample exhibit resistances below 200Ω. These results match well with the observed resistances from galvanostatic methods.

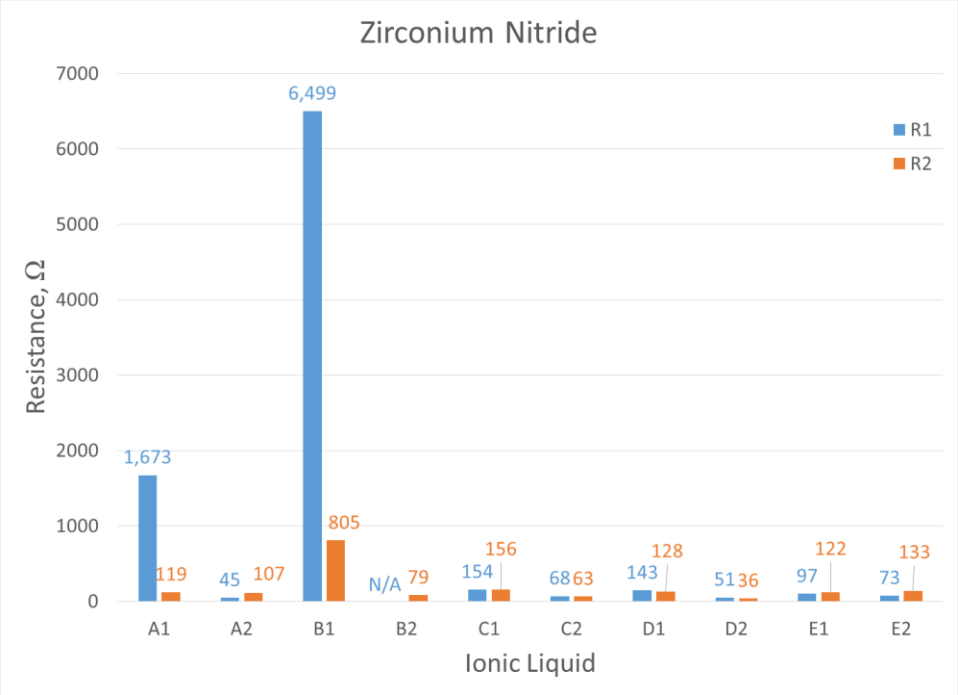

Figure 87: Resistance of ZrN_x samples measured by impedance spectroscopy. N/A signifies the resistance value had no impact for fitting to the measured data. IL A and IL B had the highest resistances with most other samples having resistances comparable to the best samples of other architectures in this work.

4.7. Chapter Summary

In this section, electrochemical measurements were described and discussed. In particular, capacitance and resistance were measured. Through simple calculations, using the measured values, energy and power density were calculated.

Capacitance was evaluated through CV tests at scan rates of 10, 50, 100, 200, and 500mV/s. These scan rates correspond to typical rates that would be seen in actual applications. The highest capacitances were achieved using titanium based electrodes with TiN_x outperforming TiO_x. However, some ZrN_x samples exhibited capacitances as high as

the titanium samples. ZrO_x did not exhibit significant pseudocapacitance and therefore performed most like the non-functionalized CNT electrodes.

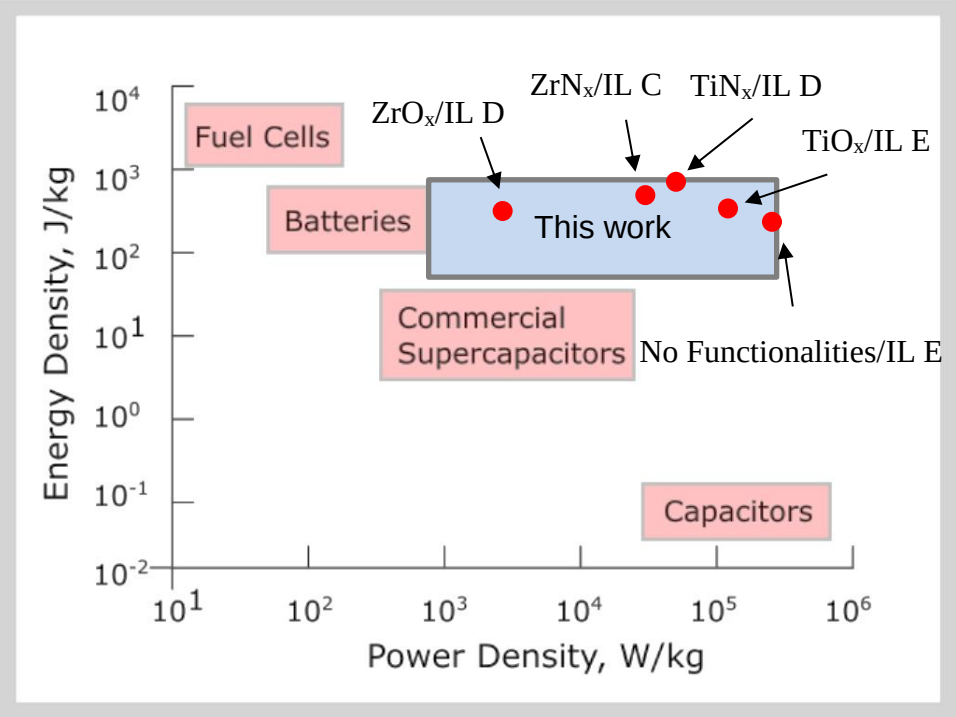

Figure 88: Ragone plot showing the presented supercapacitor performance with respect to other energy storage devices. A data point is shown for the maximum energy density of each pseudocapacitive coating.

Galvanostatic methods were verified through impedance spectroscopy to quantify the resistance of the paired IL and pseudocapacitive coatings. The impedance measurements correlated well with the galvanostatic methods and supported the method to calculate resistance presented in the previous section.

The lowest resistance sample had a resistance of 67.5Ω which is on par with the 54Ω achieved by Chen et al. with graphene oxide and IL based supercapacitors [69]. However, the presented samples had resistances far higher than those observed by Fisher et al. [31]. Fisher et al. reported using a solution of IL A and acetonitrile. The addition of acetonitrile reduces the resistance and increases the viscosity which explains the significant difference in results. The samples reported in this work had resulting power densities of 1 – 400 kW/kg.

Samples fabricated with IL A generally had the highest resistance. However this is most likely attributed to the difficulties in working with such a high viscosity liquid. Other methods of fabrication should be investigated such as using a heated syringe, to reduce viscosity, to inject the IL or expanding the fill port size. Although these difficulties are exacerbated by highly viscous ILs, this would also explain inconsistencies in the measured resistances among sample sets.

CHAPTER 5

CONCLUSION

Supercapacitors are a technology with the potential to revolutionize electronics today. This work utilized industrial silicon based technologies to produce chip scale carbon nanotube supercapacitors. The testing methods used in this work are standard testing procedures in the supercapacitor field. Testing of a variety of pseudocapacitive coatings and IL electrolytes is important since new coatings and electrolytes are continuously being developed. The results of this work showed a maximum energy density and power density of ~800 J/kg and ~400kW/kg, respectively.

The goals of this research were (1) to develop a chip scale, silicon based, CNT supercapacitor electrode, (2) evaluate promising pseudocapacitive oxide coatings and their nitride counterparts, (3) survey IL electrolytes with large electrochemical windows and a variety of viscosities, (4) determine a path to focus next efforts in supercapacitor research through pairing pseudocapacitive coatings and IL electrolytes.

Supercapacitor electrodes were developed utilizing a pathway of silicon based processing. When fabricating these electrodes it is particularly important to achieve a negative profile DRIE pit to prevent catalyst deposition, and the resulting CNT growth, on the sidewalls and top of the electrodes. The roughness also needs to be minimized – no silicon grass should be present – in order to ensure adhesion of the catalyst layer for CNT growth. Metal catalysts should be utilized to ensure a conductive pathway for the as grown CNTs. Side fill ports were added to increase the usable electrode surface area, however a

bumper needs to be used to ensure no CNTs are sheared during filling. During filling it is important to ensure the CNT cavity is filled entirely to prevent high resistance supercapacitors. Due to difficulties filling the cavities, it is suggested to use low viscosity ILs.

Analyzing the pseudocapacitive coatings with XPS revealed that the oxide samples had limited nitride contamination. However, the nitride samples had heavy oxygen contamination which resulted in oxynitride formation. Each sample displayed contamination from excess ligands and amino groups.

TiN_x samples proved to be more effective than TiO_x samples. This is possibly due to the higher conductivity of the TiN_x coatings however might also be associated with a more favorable pseudocapacitive reaction between the ILs and the nitrogen in TiN_x. ZrN_x samples performed worse than ZrO_x samples except for the ZrN_x combined with IL C. This combination far outperformed any comparable Zr based sample and was on par with the best Ti based samples. It is therefore suggested that TiN_x and ZrN_x be studied further and, in particular, in combination with IL D and IL C respectively. These combinations are particularly favorable due to the large electrochemical window (5.5V) of the respective ILs. Due to the contamination of the nitride samples, it is imperative that different thicknesses of oxynitrides be studied as pseudocapacitive coatings since the nitride samples outperformed the oxide samples. Different oxide thicknesses should also be studied since the contaminated nitride samples likely had less oxide than the oxide samples.

Scan rate had a significant effect on the achievable capacitance. In this work, scan rates ranging from 10 – 50mV/s were used which correspond to real world applications. At

low scan rates, the highest capacitance achieved was 20.38mF using TiN_x combined with IL D. At high scan rates, the highest capacitance achieved was 6.44mF using TiO_x and IL B. This suggests that zirconium coatings may not be as effective for supercapacitors as titanium based coatings.

Viscosity did not have a significant effect on the capacitance or resistance of the samples. However, since the supercapacitors were filled through micron sized fill ports, viscosity dramatically impacted their manufacturability. This was observed through high resistance measurements of samples that may not have been filled entirely or may have leaked.

For some samples, particularly nitride based samples that showed pseudocapacitive peaks, capacitance increased over time. This may suggest a conditioning effect for nitride samples, however, further work is needed to distinguish a possible conditioning effect from electrode degradation or overcharging effects.

CHAPTER 6

FUTURE WORK

Supercapacitors are a promising candidate to fill the gap in energy storage devices created by batteries and capacitors. CNT based supercapacitors are readily functionalized through techniques such as PECVD and ALD. However, the amount of carbon modifications and number of cycles of ALD needed to optimize the architecture will greatly depend on the density and height of the CNTs and also on the electrolyte being used. These processes should be studied in order to optimize the architecture of the device.

In this work, capacitance was studied with respect to voltage scan rate. It would also be beneficial to have an understanding of the change in resistance versus charge/discharge rate. These tests could be done with changing currents, using galvanostatic methods, or with CV tests. However, in the latter, a metric would need to be established to measure the slant of the CV curve.

Asymmetric supercapacitor electrodes should also be studied to maximize the capacitance of the supercapacitor architecture. The anode and cathode of the ILs will have different electrical and physical properties. These properties should pair with the respective electrode. For example, anodic ions are traditionally smaller than cathodic ions. Therefore, the anodic electrode would be able to utilize small pore sizes. However, if the same electrode is used for the cathodic electrode, the cathodic ions may not be able to access all of the pores. Therefore, the porosity of each electrode should be tailored for the respective

anodic or cathodic ion. A similar principle can be explored to pair the electrolyte cathode and anode with an appropriate pseudocapacitive coating on the device cathode and anode.

In tandem with creating asymmetric supercapacitor electrodes, it would be useful to conduct in depth studies using transmission electron microscopy (TEM) to study the interactions between various ILs and the CNT electrodes with and without functionalizations.

Hermeticity is highly desirable in the presented supercapacitor architecture in order to prevent degradation of the IL electrolytes. A design that involves metal or ceramic binders between the electrodes should be used. In particular, glass frit bonding is a viable option and should be studied as it can be isolate the silicon current collectors and prevent short circuiting especially after the surfaces have been coated with relatively conducive nitride coatings. In the present work, the separating membrane was used to separate the current collectors as well as the electrodes.

It would be beneficial to utilize supercapacitors at a wide range of temperatures in order to apply them to many applications. Therefore, studies should also be conducted at various temperatures. Ionic mobility in the IL is highly dependent on the operating temperature and therefore the capacitance would be expected to be affected by changes in temperature.

APPENDIX A

FURTHER FIGURES

A.1. Scanning Electron Microscopy

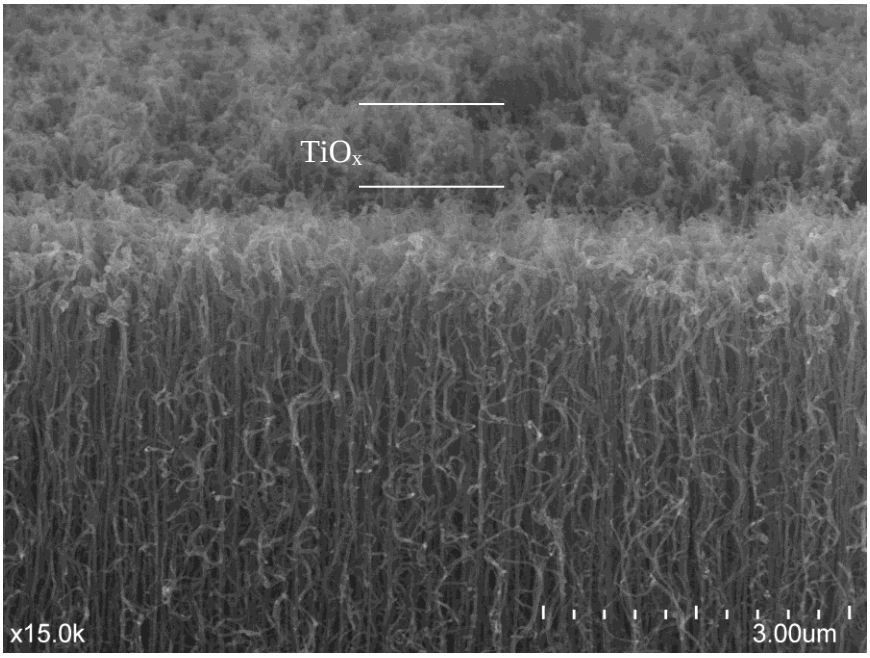

A. 1: TiO_x coated CNTs. Thicker coatings are observed at the top which suggests the coating is not conformal. (Photo courtesy of Stephan Turano)

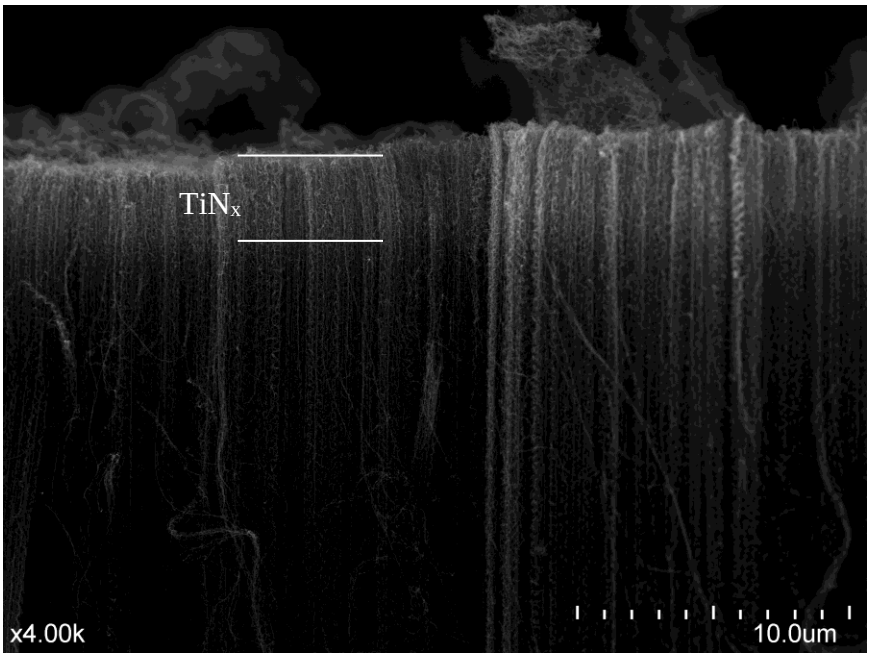

A. 2: TiN_x coated CNTs. Only the first few µm were actually coated by the ALD process. Further Process development is required to ensure conformal coating of the CNTs.

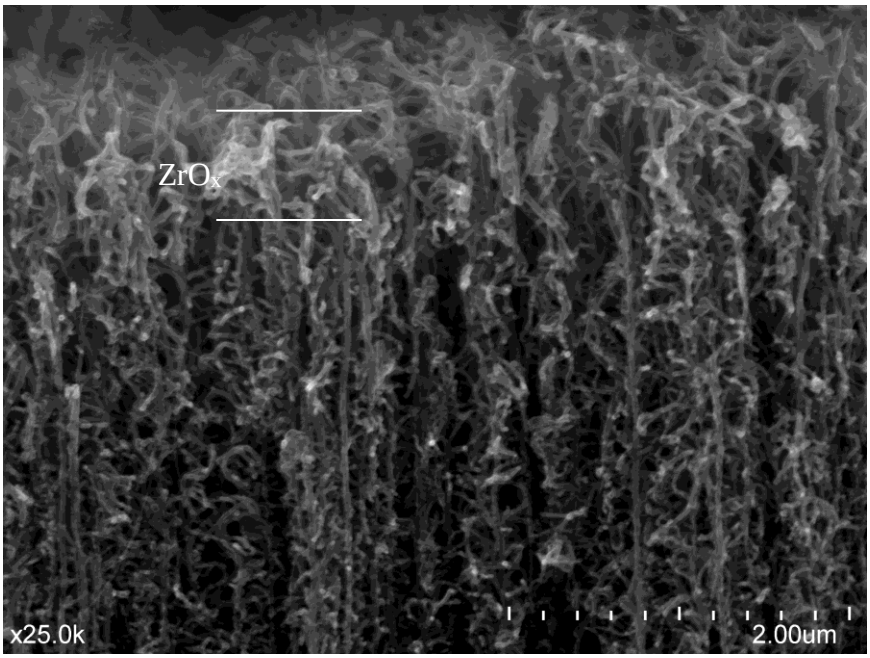

A. 3: Conformal coating of CNTs with ZrO_x but only for the first few µm as seen by the gradient from the top of the figure to the bottom.

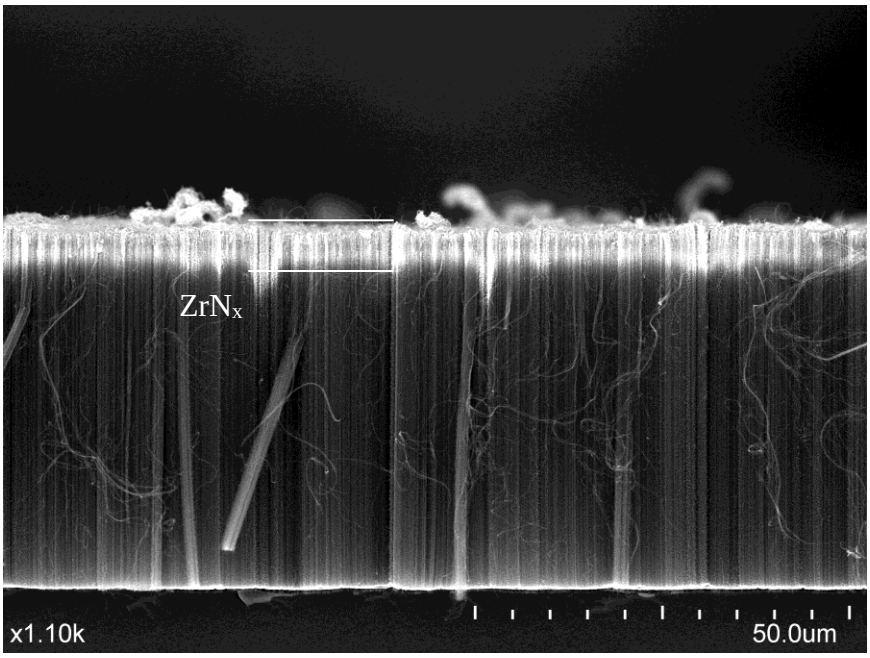

A. 4: Conformal coating of CNTs with ZrN_x but only for the first few µm as seen by the light area at the tip of the CNTs.

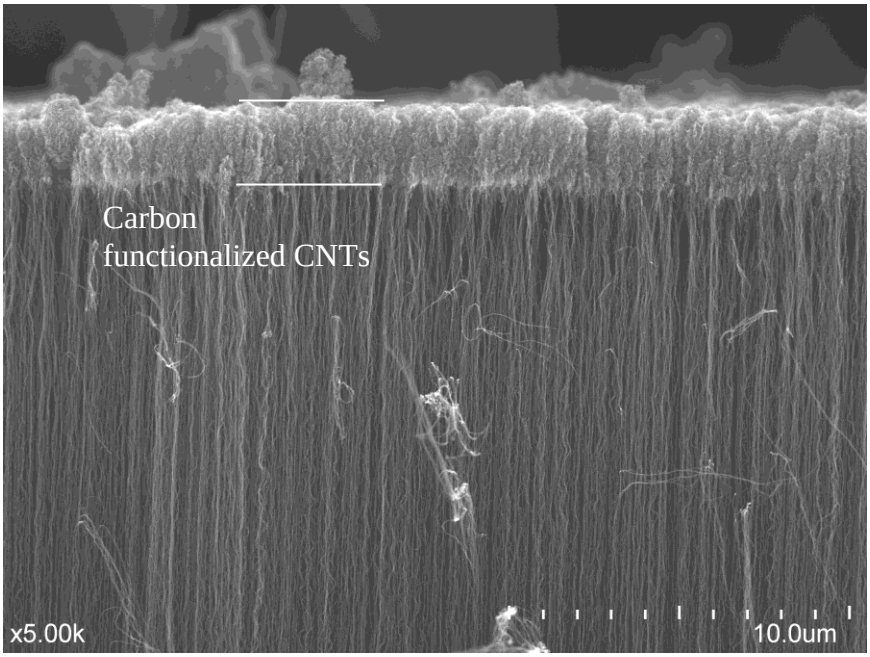

A. 5: Carbon functionalized CNTs. Only the tips of the CNTs were able to grow carbon foliates well unless a large spark hit the CNTs in which case the surrounding CNTs were conformally covered. (photo courtesy of Stephan Turano)

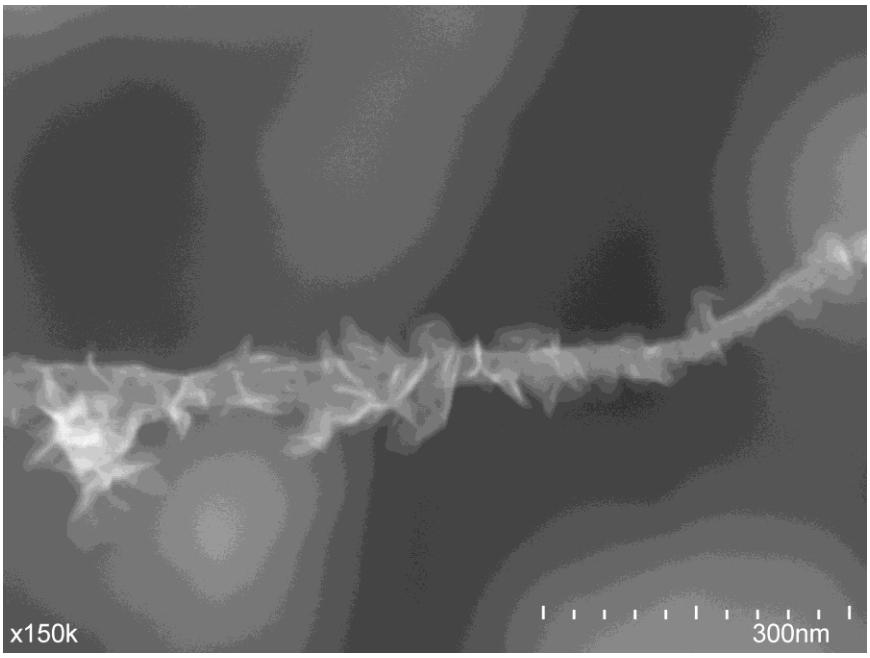

A. 6: Carbon functionalized CNT. (photo courtesy of Stephan Turano)

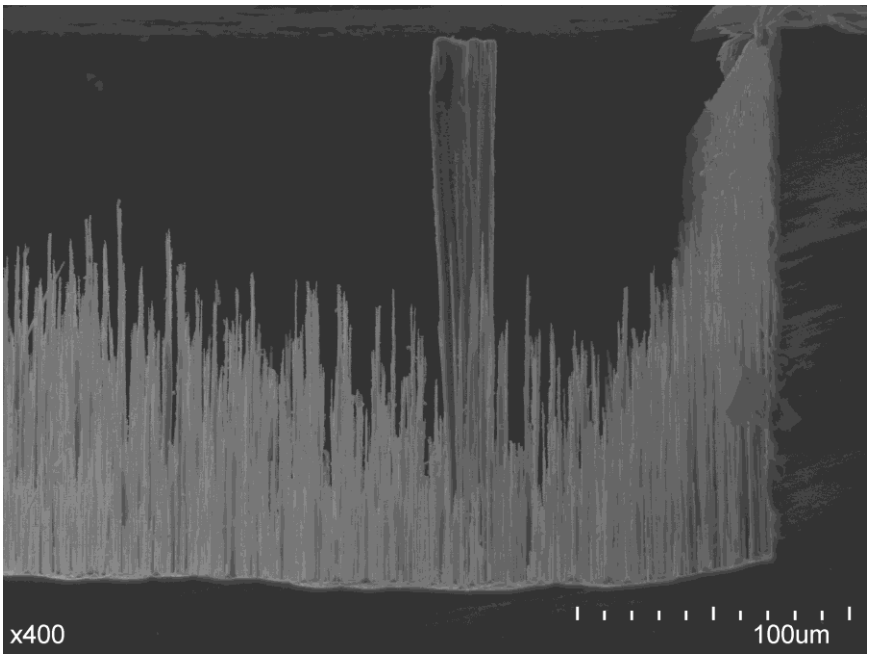

A. 7: Silicon grass formed from DRIE. The formation of the peaks in the pit must be avoided to ensure adhesion of the catalyst layer and to allow sufficient gas flow to grow CNTs.

A.2. Impedance Data and Fitting

In order to verify the galvanostatic methods, impedance spectroscopy was completed for the tested samples. This appendix is used as a repository for each set of impedance data collected. Each test conducted with a 500mV alternative voltage and a frequency scan from 1 hz to 1Mhz. However, the fitted data does not always span the entire range of the frequency scan due to the formation of the Warburg impedance. Warburg impedance presents itself as a 45° angle at the low frequency range of data. Because the simple model that was used does not account for the Warburg impedance, the low frequency data is sometimes not included in the fitting parameters. On few occasions, high frequency data was also ignored in order to accurately fit the region where the resistance is being measured. With a simple equivalent circuit model and limited computing power it is difficult to account for every abnormality in each graph.

A.2.1. No Functionalities

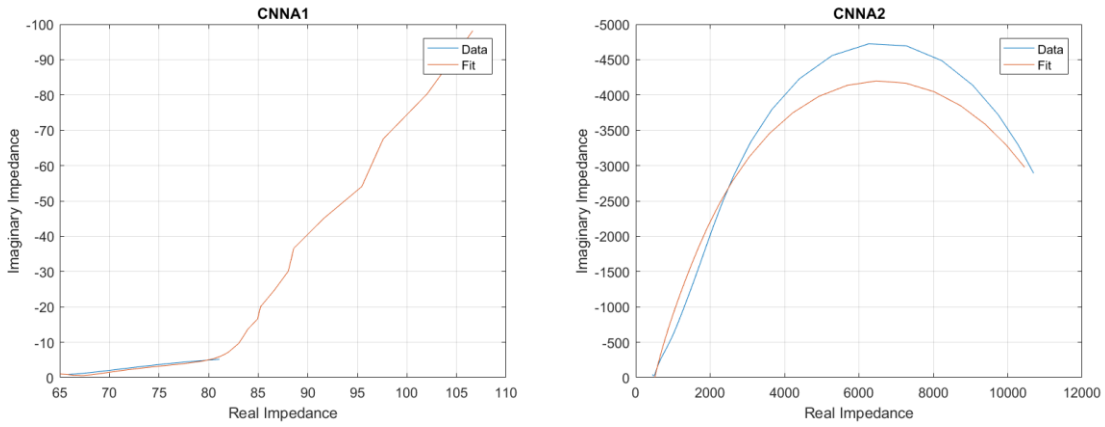

A. 8: Impedance spectroscopy measurements and fitting for electrodes without functionalities paired with IL A.

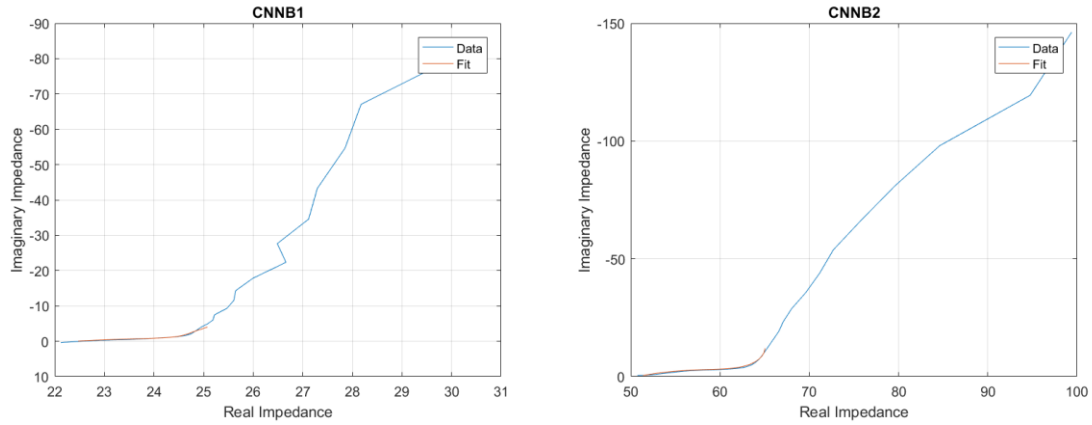

A. 9: Impedance spectroscopy measurements and fitting for electrodes without functionalities paired with IL B.

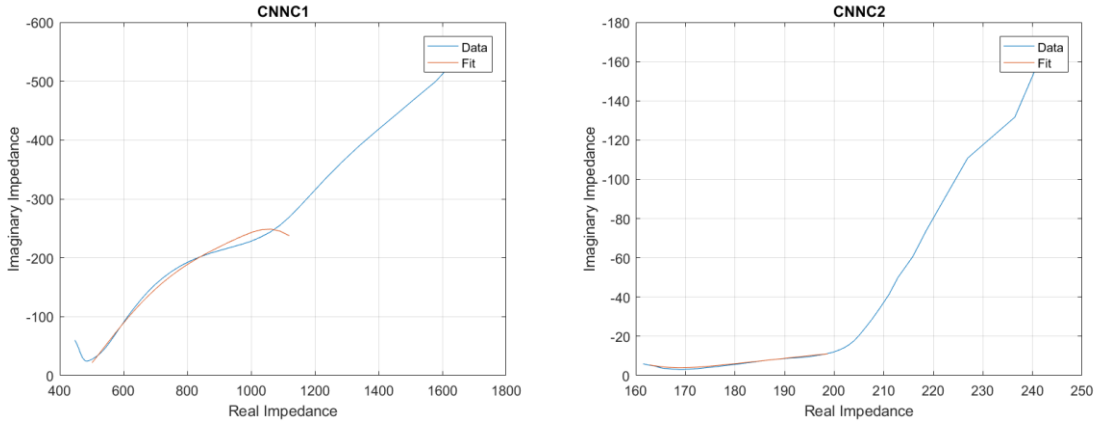

A. 10: Impedance spectroscopy measurements and fitting for electrodes without functionalities paired with IL C.

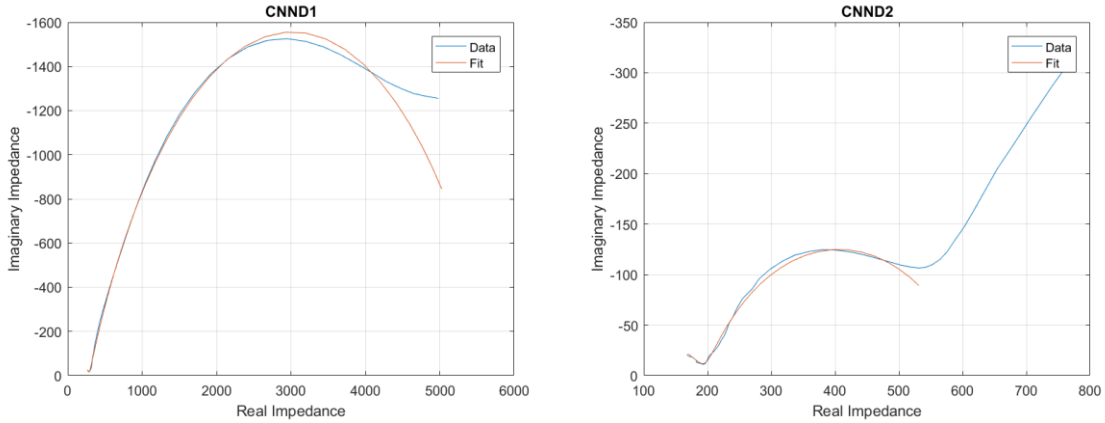

A. 11: Impedance spectroscopy measurements and fitting for electrodes without functionalities paired with IL D.

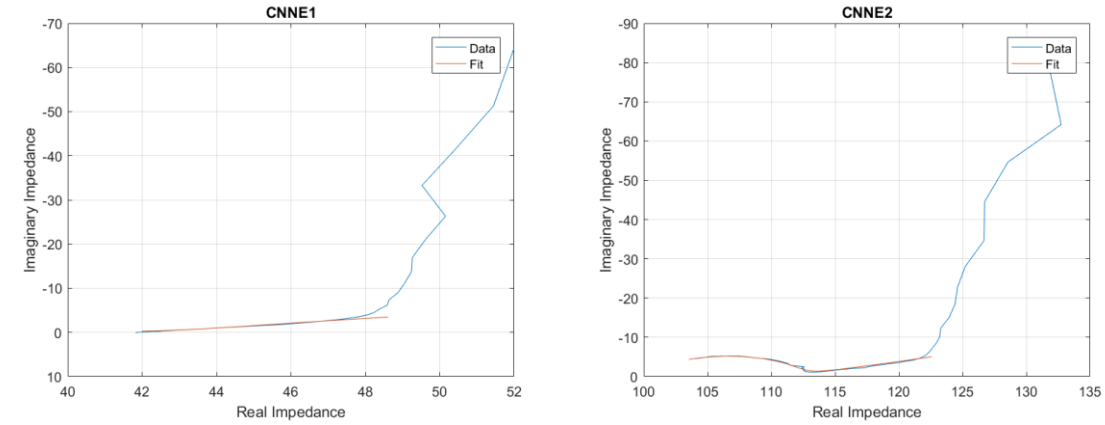

A. 12: Impedance spectroscopy measurements and fitting for electrodes without functionalities paired with IL E.

A.2.2. Titanium Oxide

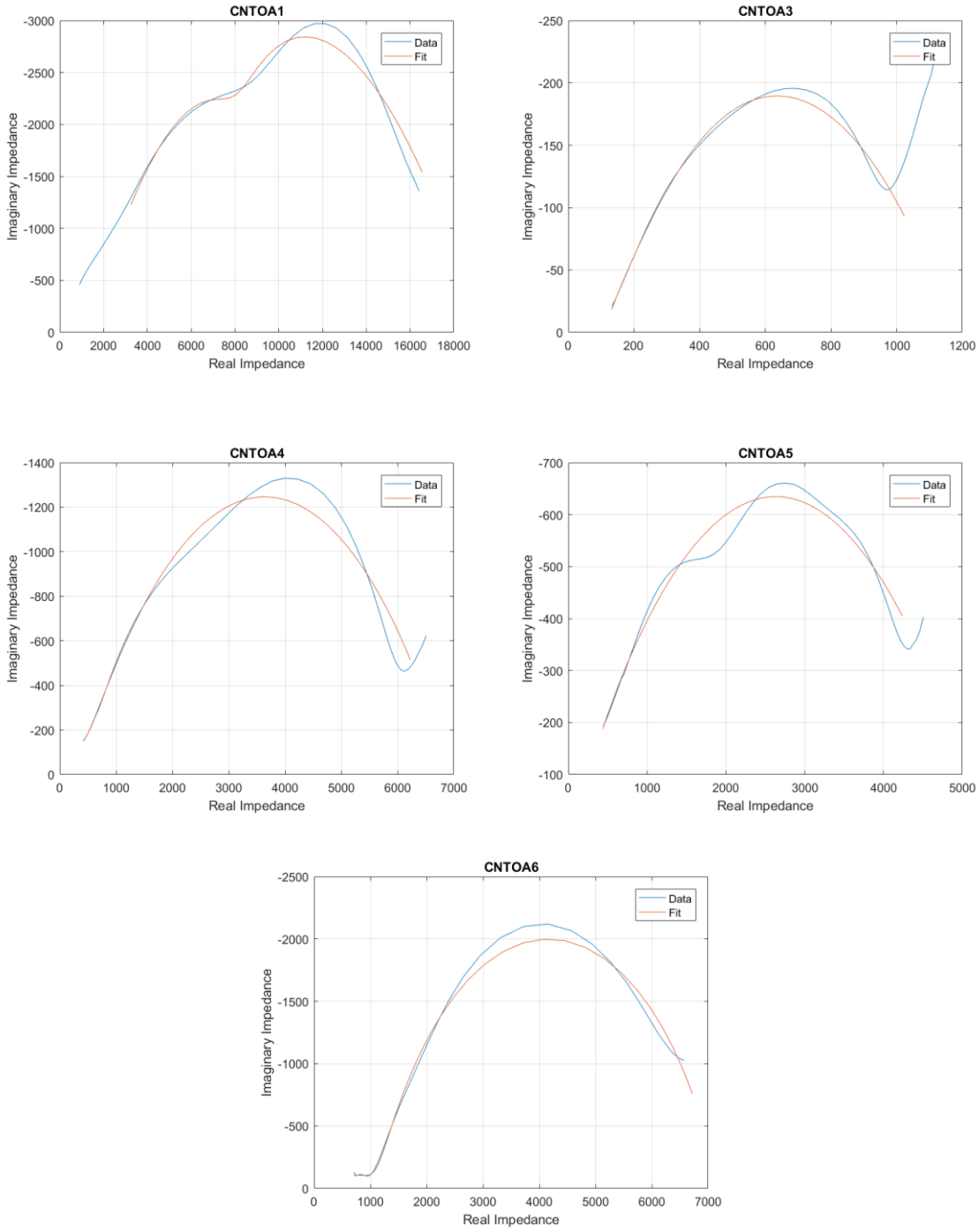

A. 13: Impedance spectroscopy measurements and fitting for electrodes with TiO_x functionalities paired with IL A.

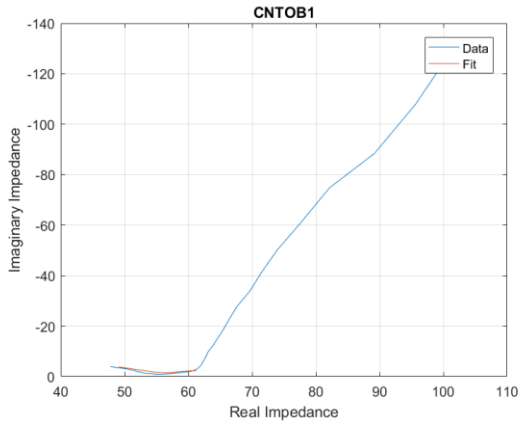

A. 14: Impedance spectroscopy measurements and fitting for electrodes with TiO_x functionalities paired with IL B.

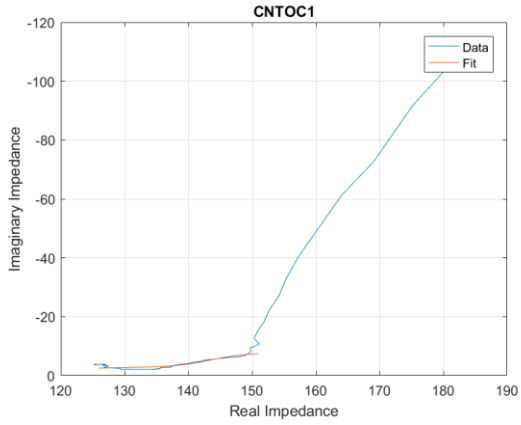

A. 15: Impedance spectroscopy measurements and fitting for electrodes with TiO_x functionalities paired with IL C.

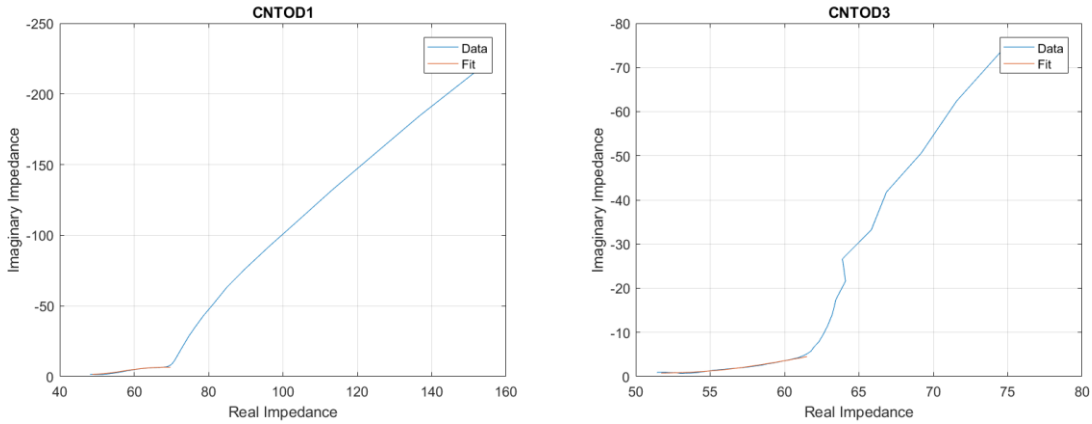

A. 16: Impedance spectroscopy measurements and fitting for electrodes with TiO_x functionalities paired with IL D.

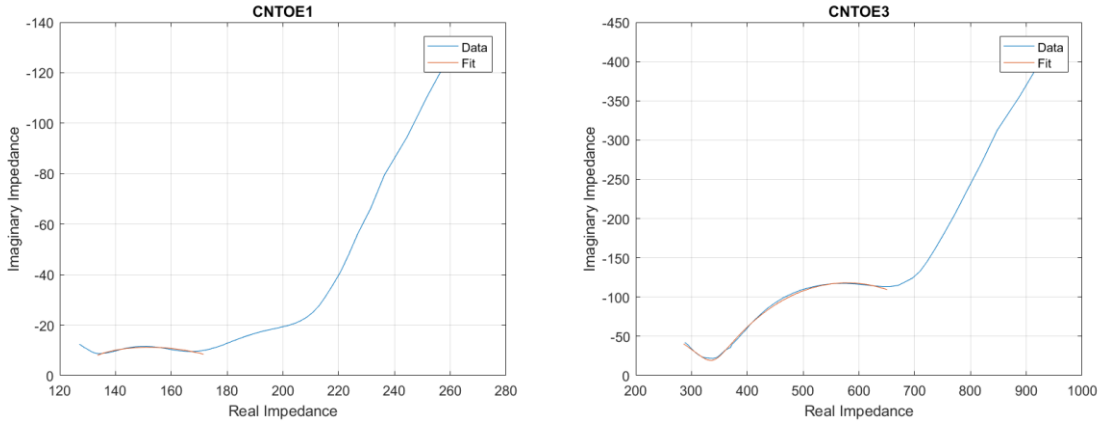

A. 17: Impedance spectroscopy measurements and fitting for electrodes with TiO_x functionalities paired with IL E.

A.2.3. Titanium Nitride

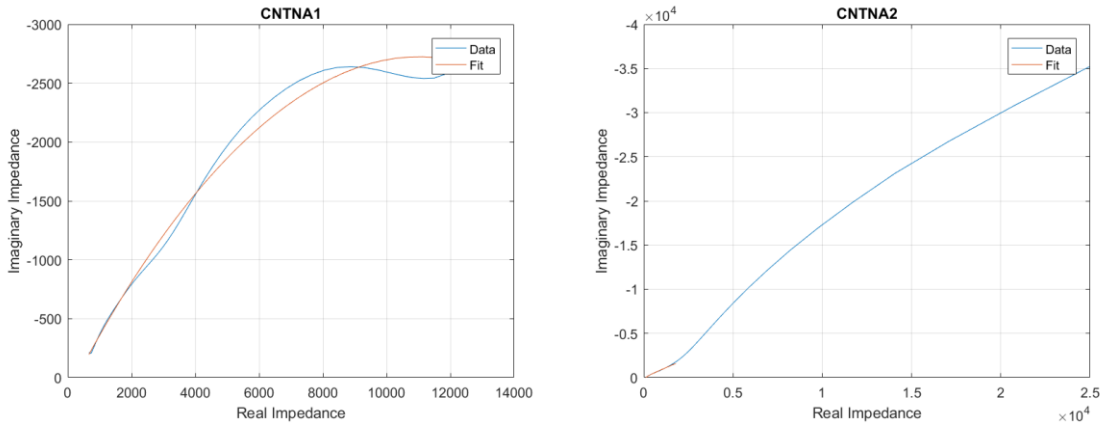

A. 18: Impedance spectroscopy measurements and fitting for electrodes with TiN_x functionalities paired with IL A.

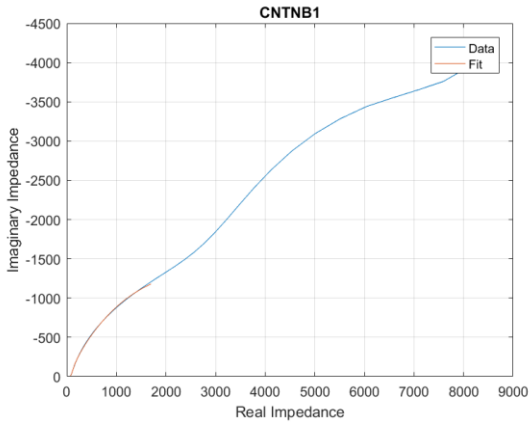

A. 19: Impedance spectroscopy measurements and fitting for electrodes with TiN_x functionalities paired with IL B.

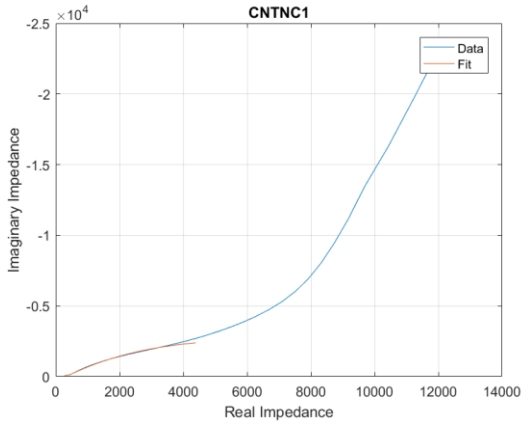

A. 20: Impedance spectroscopy measurements and fitting for electrodes with TiN_x functionalities paired with IL C.

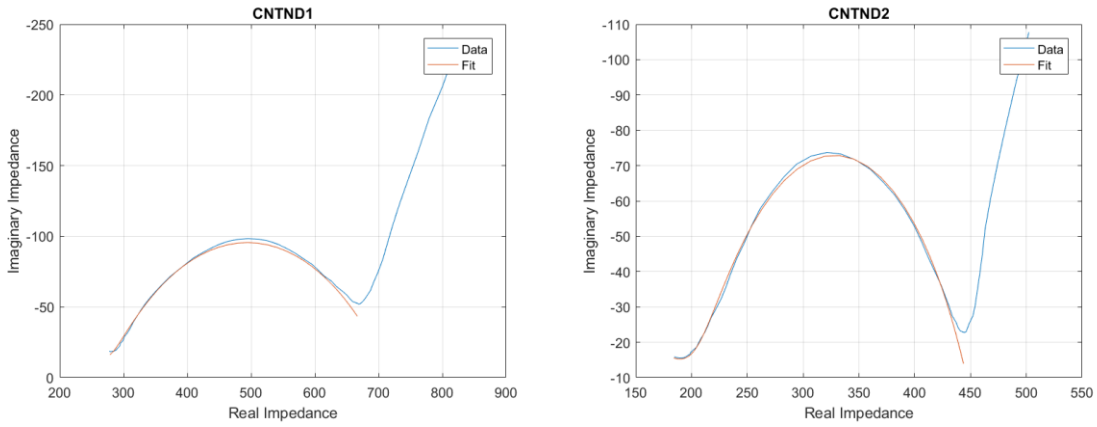

A. 21: Impedance spectroscopy measurements and fitting for electrodes with TiN_x functionalities paired with IL D.

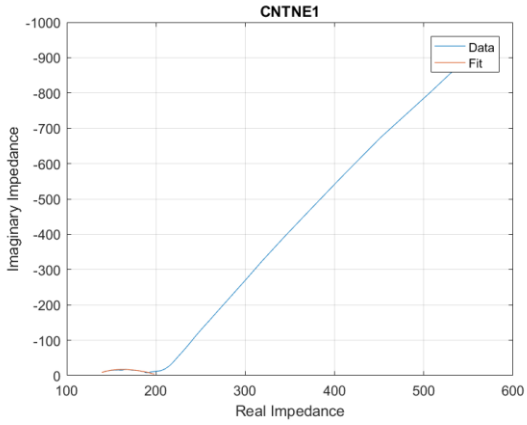

A. 22: Impedance spectroscopy measurements and fitting for electrodes with TiN_x functionalities paired with IL E.

A.2.4. Zirconium Oxide

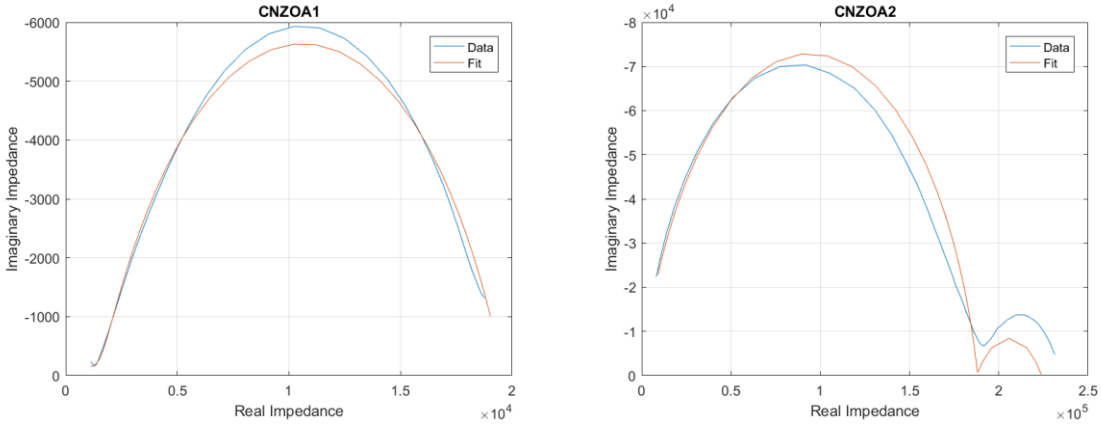

A. 23: Impedance spectroscopy measurements and fitting for electrodes with ZrO_x functionalities paired with IL A.

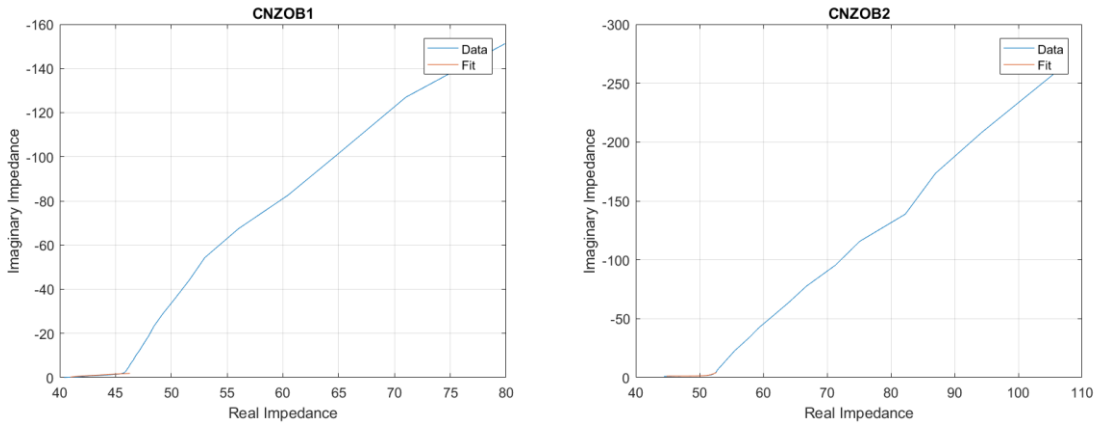

A. 24: Impedance spectroscopy measurements and fitting for electrodes with ZrO_x functionalities paired with IL B.

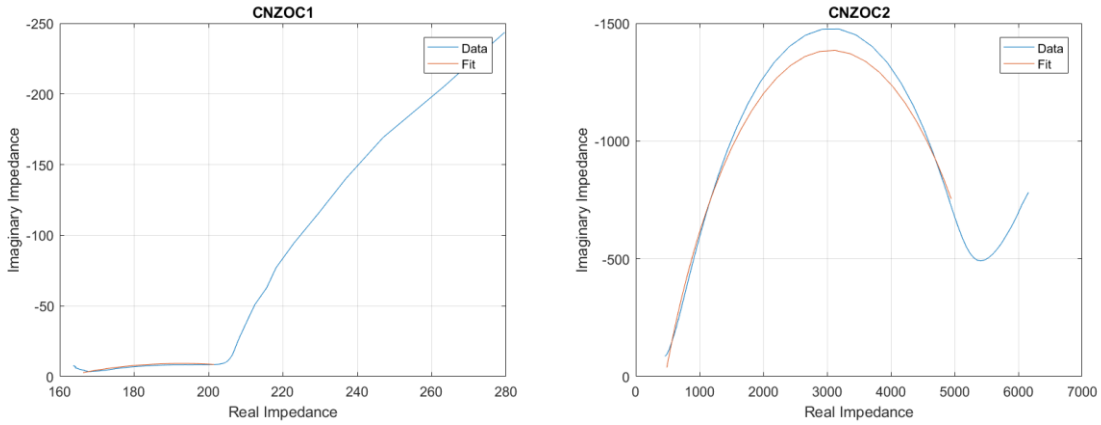

A. 25: Impedance spectroscopy measurements and fitting for electrodes with ZrO_x functionalities paired with IL C.

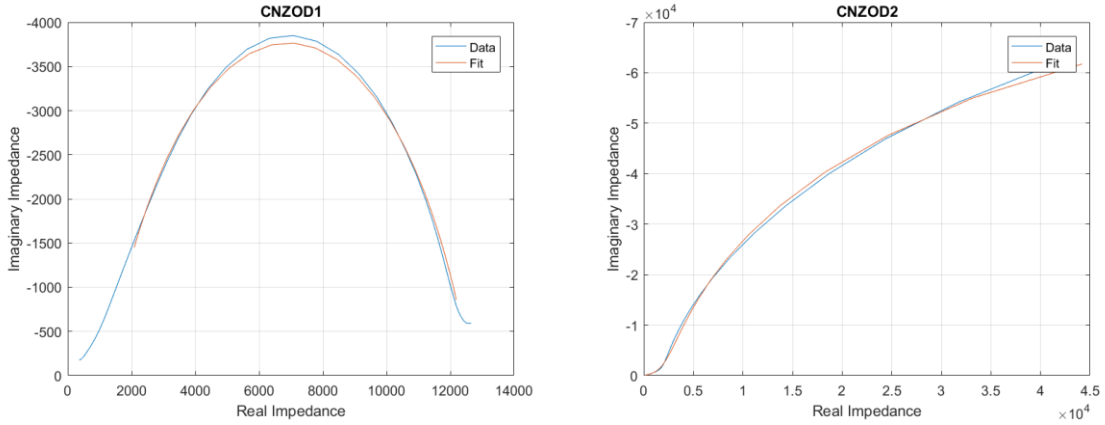

A. 26: Impedance spectroscopy measurements and fitting for electrodes with ZrO_x functionalities paired with IL D.

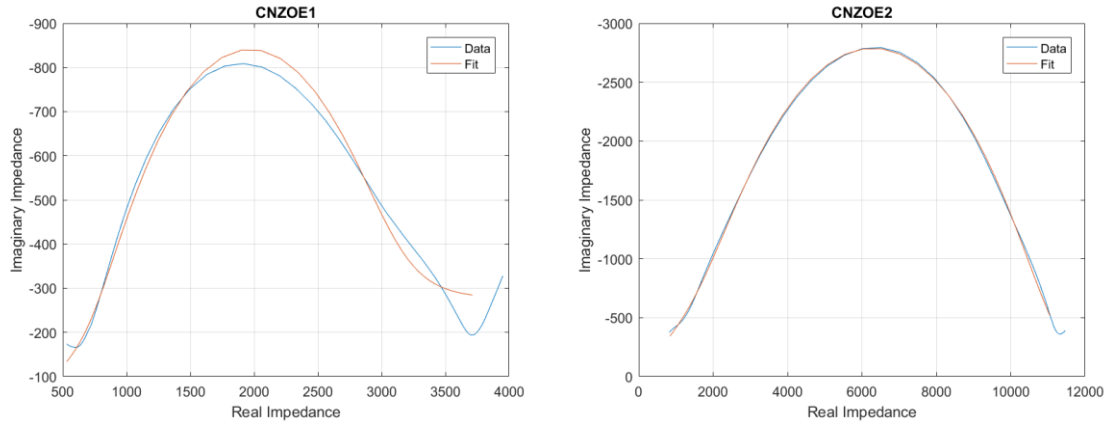

A. 27: Impedance spectroscopy measurements and fitting for electrodes with ZrO_x functionalities paired with IL E.

A.2.5. Zirconium Nitride

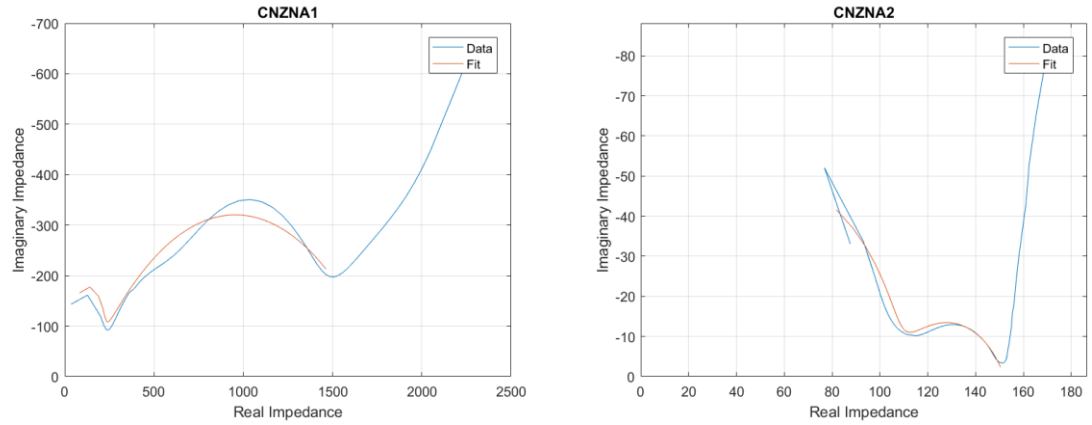

A. 28: Impedance spectroscopy measurements and fitting for electrodes with ZrN_x functionalities paired with IL A.

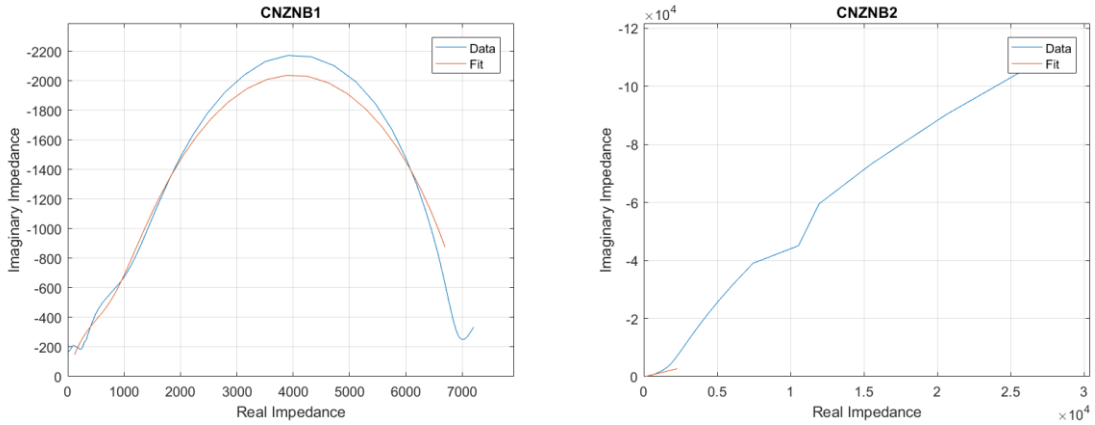

A. 29: Impedance spectroscopy measurements and fitting for electrodes with ZrN_x functionalities paired with IL B.

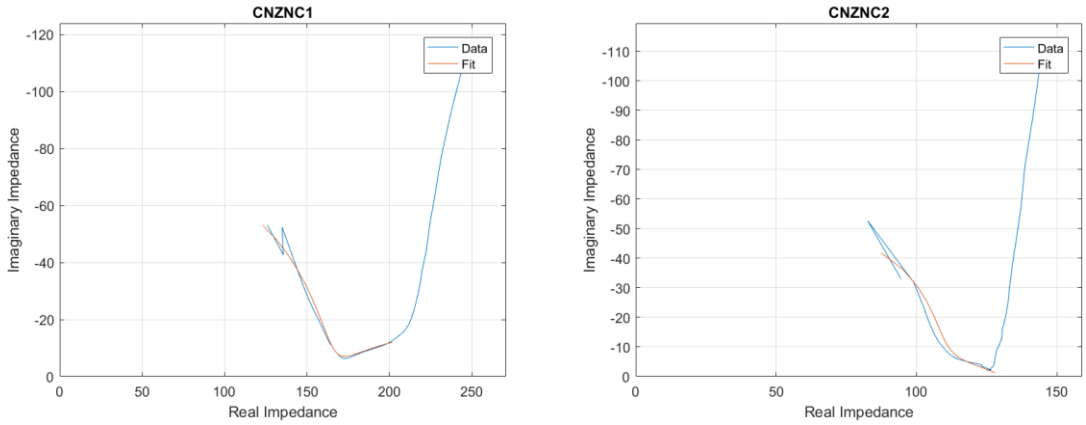

A. 30: Impedance spectroscopy measurements and fitting for electrodes with ZrN_x functionalities paired with IL C.

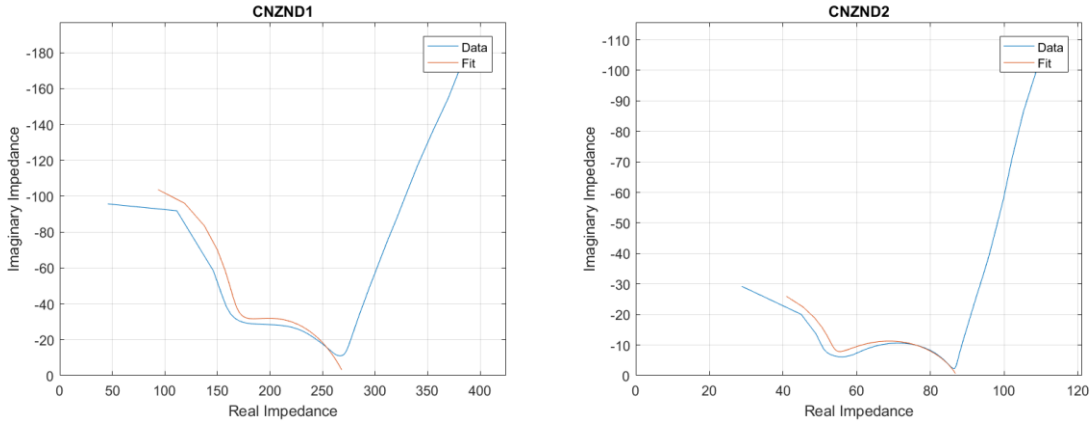

A. 31: Impedance spectroscopy measurements and fitting for electrodes with ZrN_x functionalities paired with IL D.

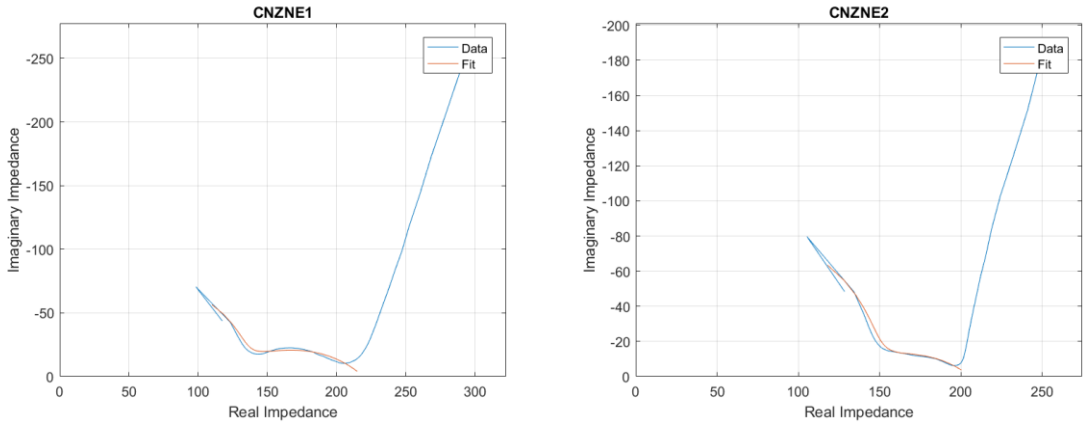

A. 32: Impedance spectroscopy measurements and fitting for electrodes with ZrN_x functionalities paired with IL E.

REFERENCES

1. Conway, B. E., *Electrochemical Supercapacitors Scientific Fundamentals and Technological Applications*. 1999: Plenum Publishers.

2. Pandolfo, A. G.; Hollenkamp, A. F., *Carbon Properties and Their Role in Supercapacitors.* Journal of Power Sources, 2006. **157**(1): p. 11-27.

3. Sharma, P.; Bhatti, T. S., *A Review on Electrochemical Double-Layer Capacitors.* Energy Conversion and Management, 2010. **51**(12): p. 2901-2912.

4. Helmholtz, H. v., Ann. Phys. (Leipzig), 1853. **211**(89).

5. Conway, B. E.; Birss, V.; Wojtowicz, J., *The Role and Utilization of Pseudocapacitance for Energy Storage by Supercapacitors.* Journal of Power Sources, 1997. **66**: p. 1-14.

6. Conway, B. E., *Transition from "Supercapacitor" to "Battery" Behavior in Electrochemical Energy Storage.* Journal of The Electrochemical Society, 1991. **138**(6): p. 1539-1548.

7. Snook, G. A.; Kao, P.; Best, A. S., *Conducting-Polymer-Based Supercapacitor Devices and Electrodes.* Journal of Power Sources, 2011. **196**(1): p. 1-12.

8. Snook, G. A.; Chen, G. Z.; Fray, D. J.; Hughes, M.; Shaffer, M., *Studies of Deposition of and Charge Storage in Polypyrrole–Chloride and Polypyrrole–Carbon Nanotube Composites with an Electrochemical Quartz Crystal Microbalance.* Journal of Electroanalytical Chemistry, 2004. **568**: p. 135-142.

9. Zhi, M.; Xiang, C.; Li, J.; Li, M.; Wu, N., *Nanostructured Carbon-Metal Oxide Composite Electrodes for Supercapacitors: A Review.* Nanoscale, 2013. **5**(1): p. 72-88.

10. Peigney, A.; Laurent, C.; Flahaut, E.; Bacsa, R. R.; Rousset, A., *Specific Surface Area of Carbon Nanotubes and Bundles of Carbon Nanotubes.* Carbon, 2001. **39**(4): p. 507-514.

11. M. Thommes, K. K., A. V. Neimark, J. P. Olivier, F. Rodriguez-Reinoso, J. Rouquerol, K. S. W. Sing, *Physisorption of Gases, with Special Reference to the Evaluation of Surface Area and Pore Size Distribution (Iupac Technical Report).* Pure and Applied Chemistry, 2015. **87**(9-10).

12. Kötz, R.; Carlen, M., *Principles and Applications of Electrochemical Capacitors.* Electrochimica Acta, 2000. **45**: p. 2483-2498.

13. Kim, N. D.; Kim, S. J.; Kim, G.-P.; Nam, I.; Yun, H. J.; Kim, P.; Yi, J., *Nh3-Activated Polyaniline for Use as a High Performance Electrode Material in Supercapacitors.* Electrochimica Acta, 2012. **78**: p. 340-346.

14. Abbas, S. A.; Jung, K.-D., *Preparation of Mesoporous Microspheres of Nio with High Surface Area and Analysis on Their Pseudocapacitive Behavior.* Electrochimica Acta, 2016. **193**: p. 145-153.

15. Endo, M.; Maeda, T.; Takeda, T.; Kim, Y. J.; Koshiba, K.; Hara, H.; Dresselhaus, M. S., *Capacitance and Pore-Size Distribution in Aqueous and Nonaqueous Electrolytes Using Various Activated Carbon Electrodes.* Journal of The Electrochemical Society, 2001. **148**(8): p. A910.

16. Chmiola, J.; Yushin, G.; Gogotsi, Y.; Portet, C.; Simon, P.; Taberna, P. L., *Anomalous Increase in Carbon Capacitance at Pore Sizes Less Than 1 Nanometer.* Science, 2006. **313**(5794): p. 1760-3.

17. Largeot, C.; Portet, C.; Chmiola, J.; Taberna, P. L.; Gogotsi, Y.; Simon, P., *Relation between the Ion Size and Pore Size for and Electric Double-Layer Capacitor.* J. AM. CHEM. SOC., 2008. **130**: p. 2730-2731.

18. Cava, R., *Future Directions in Solid State Chemistry: Report of the Nsf-Sponsored Workshop.* Progress in Solid State Chemistry, 2002. **30**(1-2): p. 1-101.

19. Frackowiak, E.; Beguin, F., *Carbon Materials for the Electrochemical Storage of Energy in Capacitors.* Carbon, 2001. **39**: p. 937-950.

20. Yu, M.; Qiu, W.; Wang, F.; Zhai, T.; Fang, P.; Lu, X.; Tong, Y., *Three Dimensional Architectures: Design, Assembly and Application in Electrochemical Capacitors.* J. Mater. Chem. A, 2015. **3**(31): p. 15792-15823.

21. Ervin, M., *Carbon Nanotube and Graphene-Based Supercapacitors: Rationale, Status, and Prospects*. 2010, Army Research Laboratory. p. 18.

22. Chhowalla, M.; Teo, K. B. K.; Ducati, C.; Rupesinghe, N. L.; Amaratunga, G. A. J.; Ferrari, A. C.; Roy, D.; Robertson, J.; Milne, W. I., *Growth Process Conditions of Vertically Aligned Carbon Nanotubes Using Plasma Enhanced Chemical Vapor Deposition.* Journal of Applied Physics, 2001. **90**(10): p. 5308-5317.

23. Kumar, M.; Ando, Y., *Chemical Vapor Deposition of Carbon Nanotubes: A Review on Growth Mechanism and Mass Production.* Journal of Nanoscience and Nanotechnology, 2010. **10**(6): p. 3739-3758.

24. Reddy, A. L. M.; Ramaprabhu, S., *Nanocrystalline Metal Oxides Dispersed Multiwalled Carbon Nanotubes as Supercapacitor Electrodes.* J. Phys. Chem., 2007. **111**: p. 7727-7734.

25. Parker, C.; Raut, A.; Brown, B.; Stoner, B.; Glass, J., *Three-Dimensional Arrays of Graphenated Carbon Nanotubes.* Journal of Materials Research, 2012. **27**(7): p. 1056-1053.

26. Yu, K.; Lu, G.; Bo, Z.; Mao, S.; Chen, J., *Carbon Nanotube with Chemically Bonded Graphene Leaves for Electronic and Optoelectronic Applications.* The Journal of Physical Chemistry Letters, 2011. **2**(13): p. 1556-1562.

27. Fisher, R. A.; Watt, M. R.; Ready, W. J., *Functionalized Carbon Nanotube Supercapacitor Electrodes: A Review on Pseudocapacitive Materials.* ECS Journal of Solid State Science and Technology, 2013. **2**(10): p. M3170-M3177.

28. Rakhi, R. B.; Cha, D.; Chen, W.; Alshareef, H. N., *Electrochemical Energy Storage Devices Using Electrodes Incorporating Carbon Nanocoils and Metal Oxides Nanoparticles.* The Journal of Physical Chemistry C, 2011. **115**(29): p. 14392-14399.

29. Hu, C.-C.; Chen, W.-C.; Chang, K.-H., *How to Achieve Maximum Utilization of Hydrous Ruthenium Oxide for Supercapacitors.* Journal of The Electrochemical Society, 2004. **151**(2): p. A281.

30. Choi, D.; Blomgren, G. E.; Kumta, P. N., *Fast and Reversible Surface Redox Reaction in Nanocrystalline Vanadium Nitride Supercapacitors.* Advanced Materials, 2006. **18**(9): p. 1178-1182.

31. Fisher, R. A.; Watt, M. R.; Konjeti, R.; Ready, W. J., *Atomic Layer Deposition of Titanium Oxide for Pseudocapacitive Functionalization of Vertically-Aligned Carbon Nanotube Supercapacitor Electrodes.* ECS Journal of Solid State Science and Technology, 2014. **4**(2): p. M1-M5.

32. Salari, M.; Aboutalebi, S. H.; Chidemob, A. T.; Nevirkovets, I. P.; Konstantinov, K.; Liu, H., *Enhancement of the Electrochemical Capacitance of Tio2 Nanotube Arrays through Controlled Phase Transformation of Anatase to Rutile.* Physical Chemistry Chemical Physics, 2012. **14**: p. 4770-4779.

33. Zhang, W.; Tan, Y.; Gao, Y.; Wu, J.; Tang, B., *Ultrafine Nano Zirconia as Electrochemical Pseudocapacitor Material.* Ceramics International, 2015. **41**(2): p. 2626-2630.

34. Mudila, H.; Rana, S.; Zaidi, M. G. H., *Electrochemical Performance of Zirconia/Graphene Oxide Nanocomposites Cathode Designed for High Power Density Supercapacitor.* Journal of Analytical Science and Technology, 2016. **7**(1).

35. Liu, J.; Meng, X.; Hu, Y.; Geng, D.; Banis, M. N.; Cai, M.; Li, R.; Sun, X., *Controlled Synthesis of Zirconium Oxide on Graphene Nanosheets by Atomic Layer Deposition and Its Growth Mechanism.* Carbon, 2013. **52**: p. 74-82.

36. Ghimbeu, C. M.; Raymundo-Piñero, E.; Fioux, P.; Béguin, F.; Vix-Guterl, C., *Vanadium Nitride/Carbon Nanotube Nanocomposites as Electrodes for Supercapacitors.* Journal of Materials Chemistry, 2011. **21**(35): p. 13268.

37. Kao, E.; Yang, C.; Warren, R.; Kozinda, A.; Lin, L., *Ald Titanium Nitride on Vertically Aligned Carbon Nanotube Forests for Electrochemical Supercapacitors.* Sensors and Actuators A: Physical, 2016. **240**: p. 160-166.

38. Marichy, C.; Pinna, N., *Carbon-Nanostructures Coated/Decorated by Atomic Layer Deposition: Growth and Applications.* Coordination Chemistry Reviews, 2013. **257**(23-24): p. 3232-3253.

39. Marichy, C.; Bechelany, M.; Pinna, N., *Atomic Layer Deposition of Nanostructured Materials for Energy and Environmental Applications.* Adv Mater, 2012. **24**(8): p. 1017-32.

40. Zheng, C.; Qian, W.; Yu, Y.; Wei, F., *IL Coated Single-Walled Carbon Nanotube Buckypaper as Supercapacitor Electrode.* Particuology, 2013. **11**(4): p. 409-414.

41. Sillars, F. B.; Fletcher, S. I.; Mirzaeian, M.; Hall, P. J., *Variation of Electrochemical Capacitor Performance with Room Temperature IL Electrolyte Viscosity and Ion Size.* Phys Chem Chem Phys, 2012. **14**(17): p. 6094-100.

42. Huang, M.-M.; Jiang, Y.; Sasisanker, P.; Driver, G. W.; Weingärtner, H., *Static Relative Dielectric Permittivities of ILs at 25 °C.* Journal of Chemical & Engineering Data, 2011. **56**(4): p. 1494-1499.

43. Kim, K. S.; Shin, B. K.; Lee, H., *Physical and Electrochemcial Properties of 1-Butyl-3-Methylimidazolium Bromide, 1-Butyl-3-Methylimidazolium Iodide, and 1-Butyl-3-Methylimidazolium Tetrafluoroborate.* Korean J. Chem. Eng., 2004. **21**(5): p. 1010-1014.

44. Schreiner, C.; Zugmann, S.; Hartl, R.; Gores, H. J., *Fractional Walden Rule for ILs: Examples from Recent Measurements and a Critique of the So-Called Ideal Kcl Line for the Walden Plot.* J. Chem. Eng. Data, 2010. **55**: p. 1784-1788.

45. Sangoro, J.; Iacob, C.; Serghei, A.; Naumov, S.; Galvosas, P.; Karger, J.; Wespe, C.; Bordusa, F.; Stoppa, A.; Hunger, J.; Buchner, R.; Kremer, F., *Electrical Conductivity and Translational Diffusion in the 1-Butyl-3-Methylimidazolium Tetrafluoroborate IL.* J Chem Phys, 2008. **128**(21): p. 214509.

46. Irvin, J. A.; Stenger-Smith, J. D., *ILs for Energy Storage Applications*, in *Material Matters*. Sigma-Aldrich. p. 103-109.

47. Safarov, J.; El-Awady, W. A.; Shahverdiyev, A.; Hassel, E., *Thermodynamic Properties of 1-Ethyl-3-Methylimidazolium Bis(Trifluoromethylsulfonyl)Imide.* J. Chem. Eng. Data, 2011. **56**: p. 106-112.

48. Pereiro, A. B.; Veiga, H. I. M.; Esperança, J. M. S. S.; Rodríguez, A., *Effect of Temperature on the Physical Properties of Two ILs.* The Journal of Chemical Thermodynamics, 2009. **41**(12): p. 1419-1423.

49. Bhattacharjee, A.; Luis, A.; Lopes-da-Silva, J. A.; Freire, M. G.; Carvalho, P. J.; Coutinho, J. A., *Thermophysical Properties of Sulfonium- and Ammonium-Based ILs*. Fluid Phase Equilib, 2014. **381**: p. 36-45.

50. Hayamizu, K.; Tsuzuki, S.; Seki, S., *Transport and Electrochemical Properties of Three Quaternary Ammonium ILs and Lithium Salts Doping Effects Studied by Nmr Spectroscopy.* Journal of Chemical & Engineering Data, 2014. **59**(6): p. 1944-1954.

51. Jun, L.; Xianyou, W.; Qinghua, H.; Sergio, G.; Sebastian, P. J., *Studies on Preparation and Performances of Carbon Aerogel Electrodes for the Application of Supercapacitor.* Journal of Power Sources, 2006. **158**(1): p. 784-788.

52. Omar, N.; Gualous, H.; Salminen, J.; Mulder, G.; Samba, A.; Firouz, Y.; Monem, M. A.; Van den Bossche, P.; Van Mierlo, J., *Electrical Double-Layer Capacitors: Evaluation of Ageing Phenomena During Cycle Life Testing.* Journal of Applied Electrochemistry, 2013. **44**(4): p. 509-522.

53. Qaiser, A. A., *Dual-Transmission Line Modeling of Electrochemical Processes in Polyaniline-Cellulose Ester Composite Porous Membranes.* J Phys Chem B, 2014. **118**(32): p. 9686-94.

54. Sugimoto, W.; Iwata, H.; Yokoshima, K.; Murakami, Y.; Takasu, Y., *Proton and Electron Conductivitiy in Hydrous Ruthenium Oxides Evaluated by Electrochemical Impedance Spectroscopy: The Origin of Large Capacitance.* J. Phys. Chem., 2005. **109**: p. 7330-7338.

55. Qu, D.; Shi, H., *Studies of Activated Carbons Used in Double-Layer Capacitors.* Journal of Power Sources, 1998. **74**: p. 99-107.

56. Volfkovich, Y. M.; Mikhailin, A. A.; Bograchev, D. A.; Sosenkin, V. E.; Bagotsky, V. S., *Studies of Supercapacitor Carbon Electrodes with High Pseudocapacitance*. 2012.

57. Lai, J.; Levy, S.; Rose, M., *High Energy Density Double-Layer Capacitors for Energy Storage Applications*. 1992: IEEE Aerospace Electronic Systems Magazine. p. 14-19.

58. Barker, P. *Ultracapacitors for Use in Power Quality and Distributed Resource Applications*. in *IEEE Power Engineering Society Summer Meeting*. 2002. Knoxville, TN.

59. Kim, M. S.; Gaudiot, J.; Goldman, A., *Survey of Supercapacitors Application for Power Awareness of Embedded Systems in Internet of Things.*

60. *Murata Supercapacitor (Edlc) Technical Note*. 2014: Murata Manufacturing Co., Ltd.

61. *Xps Knowledge Base*, T. Scientific, Editor. 2017: http://xpssimplified.com/periodictable.php.

62. *Be Lookup Table for Signals from Elements and Common Chemical Species.* Handbook of The Elements and Native Oxides, 1999.

63. Badrinarayanan, S.; Sinha, S.; Mandale, A. B., *Xps Studies of Nitrogen Ion Implanted Zirconium and Titanium.* Journal of Electron Spectroscopy and Related Phenomena, 1989. **49**: p. 303-309.

64. Milosev, I.; Strehblow, H.-H.; Gaberscek, M.; Navinsek, B., *Electrochemical Oxidation of Zrn Hard (Pvd) Coatings Studied by Xps.* Surface and Interface Analysis, 1996. **24**: p. 448-458.

65. Achour, A.; Ducros, J. B.; Porto, R. L.; Boujtita, M.; Gautron, E.; Le Brizoual, L.; Djouadi, M. A.; Brousse, T., *Hierarchical Nanocomposite Electrodes Based on Titanium Nitride and Carbon Nanotubes for Micro-Supercapacitors.* Nano Energy, 2014. **7**: p. 104-113.

66. Chen, J.; Xia, N.; Zhou, T.; Tan, S.; Jiang, F.; Yuan, D., *Mesoporous Carbon Spheres: Syntehsis, Characterization and Supercapacitance.* International Journal of Electrochemical Science, 2009. **4**: p. 1063-1073.

67. Hu, Z.; Margulis, C., *Room-Temperature ILs: Slow Dynamics, Viscosity, and the Red Edge Effect.* Accounts of Chemical Research, 2007. **40**: p. 1097-1105.

68. Ruiz, V.; Huynh, T.; Sivakkumar, S. R.; Pandolfo, A. G., *IL–Solvent Mixtures as Supercapacitor Electrolytes for Extreme Temperature Operation.* RSC Advances, 2012. **2**(13): p. 5591.

69. Chen, Y.; Zhang, X.; Zhang, D.; Yu, P.; Ma, Y., *High Performance Supercapacitors Based on Reduced Graphene Oxide in Aqueous and IL Electrolytes.* Carbon, 2011. **49**(2): p. 573-580.